DEVELOPMENT OF AN ELECTRONICALLY TUNABLE ULTRA-WIDEBAND RADAR IMAGING SENSOR AND ITS COMPONENTS

A Dissertation

by

JEONGWOO HAN

Submitted to the Office of Graduate Studies of
Texas A&M University
in partial fulfillment of the requirements for the degree of

DOCTOR OF PHILOSOPHY

May 2005

Major Subject: Electrical Engineering

DEVELOPMENT OF AN ELECTRONICALLY TUNABLE ULTRA-WIDEBAND RADAR IMAGING SENSOR AND ITS COMPONENTS

A Dissertation

by

JEONGWOO HAN

Submitted to Texas A&M University
in partial fulfillment of the requirements
for the degree of

DOCTOR OF PHILOSOPHY

Approved as to style and content by:

Cam Nguyen (Chair of Committee)	Kai Chang (Member)
Don R. Halverson (Member)	Norris Stubbs (Member)
Chanan Singh (Head of Department)	

May 2005

Major Subject: Electrical Engineering

ABSTRACT

Development of an Electronically Tunable Ultra-Wideband Radar Imaging Sensor and Its Components. (May 2005)

Jeongwoo Han, B.S.; M.E., Kyungpook National University

Chair of Advisory Committee: Dr. Cam Nguyen

Novel microwave transmitter and receiver circuits have been developed for implementing UWB (Ultra-Wideband) impulse radar imaging sensor operating in frequency band 0.2 to 4 GHz. with tunable operating frequency band. The fundamental system design parameters such as the required transmitting pulse power and the pulse duration were estimated for a presumed specific application, the pavement assessment. The designed transmitter is the tunable monocycle pulse generator with tuning capability for the output pulse duration from 450- to 1200- ps, and has relatively high transmitting pulse power from 200 to 400 mW. Tuning of the pulse duration was implemented by novel PIN diode switch configuration and decoupling circuit, and boosting of transmitting pulse power was made possible by using a high power pulse driving circuit and SRD coupling circuit.

The synchronous sampling receiver system was designed by using the integrated sampling mixer and two reference clock oscillators placed in the transmitter and receiver respectively for timing control. A novel integrated CSH (Coupled-Slotline Hybrid) sampling mixer has been developed along with the design of the strobe pulse generator appropriate for the impulse radar system. The integrated sampling mixer has unprecedented conversion loss of 2.5 dB for the pulse signal, bandwidth 5.5 GHz, and dynamic range 50 dB. The introduced UWB LNA (Low Noise Amplifier) design operating up to 4 GHz should be useful for weak signal detection applications.

The design of the UWB microstrip quasi-horn antenna was optimized for short pulse transmission with respect to the input return loss and the pulse stretching effect. For signal detection in the signal processing stage, the background subtraction technique and B-scan data format were used. A novel signal monitoring technique was introduced in the signal processing to compensate the frequency modulation effect of the reference clock. The test results for the complete system with respect to some sample multi-layer structures shows good receiving pulse waveform with low distortion, enough pulse penetration depth for 13” pavement sample structure, and minimum 1-in of range resolution.

DEDICATION

To my parents, my wife, son and daughter.

ACKNOWLEDGMENTS

I would like to express my sincere gratitude to my advisor, Dr. Cam Nguyen, for his guidance, encouragement, and support throughout this research work. I would also like to thank my committee members, Dr. Kai Chang, Dr. Don R. Halverson and Dr. Norris Stubbs for their valuable time and advice.

I wish to thank Mr. Tom Scullion, Mr. Lee Gustavus, and Mr. Tony Barbosa of the Texas Transportation Institute for their help, as well as Dr. Joongsuk Park and Dr. Seoktae Kim of our Sensing, Imaging and Communication Systems Laboratory for their valuable discussion and advice as colleagues and fellow researchers. Finally, I would like to express my love and gratitude to my wife, Youngsoon Yun, son, Dongwook Han, daughter, Youra Han, and my parents for their endless support and encouragement.

This work was supported in part by the National Science Foundation, in part by the Texas Advanced Research Program and in part by Dell Computer.

TABLE OF CONTENTS

CHAPTER Page

LIST OF TABLES

TABLE Page

LIST OF FIGURES

FIGURE Page

FIGURE Page

FIGURE Page

CHAPTER I

INTRODUCTION

The UWB impulse radar is so named because it uses impulse type signal as transmitting and receiving signal to detect targets. Many types of signals such as step pulse, Gaussian impulse, single-cycle or multi-cycle signal with short pulse duration in the range of 200-ps to 5-ns can be used; but the single-cycle (monocycle) signal is commonly used in most impulse radars now developed because of its better spectral shape for wireless transmission than the step or Gaussian impulse, and wider bandwidth characteristic than the multi-cycle signal [1]-[13].

The impulse radar is distinguished from conventional radars because its impulse type signals have very wide instantaneous bandwidth (as much as several octaves or even a decade), which are much larger than conventional CW (Continuous-Wave) radars; hence it is classified as an ultra-wideband (UWB) radar [1]-[6]. There are other types of UWB radars such as the step-frequency radar according to their transmitting signal modulation type [2]-[6]. The impulse radar can be classified as a PAM (Pulse Amplitude Modulation) radar in terms of the modulation type. Compared to frequency modulation type UWB radars, the impulse radar has some general advantages, as follows. First, it

---

The journal model is *IEEE Transactions on Microwave Theory and Techniques*.

can be implemented with a more compact circuit and system structure. Second, it is likely to get higher transmitting power with a simpler circuit structure. Third, its signal processing cost required for detection of the signal is cheaper because it does not require any data conversion processing from frequency domain to time domain, as in the frequency modulation radars. These attractive aspects of the impulse radar in terms of system structure and cost have made it dominant in various UWB radar applications, and it is still more popular than the frequency modulation radar, which is evolving gradually.

The UWB radar uses extraordinary wideband signal; hence it can be used for high resolution radar applications such as target identification and fine resolution ranging or imaging. In a variety of UWB radar applications, subsurface penetrating radar (SPR) applications may be the most promising and widespread applications of the UWB radar. SPR has been used to probe and identify the subsurface or ground structure in geophysical survey. It can also be used to detect buried objects and to identify the internal structure of a non-conductive material. There are too many applications of SPR to mention here; but most typical ones are geophysical prospecting, assessment of pavement, bridge, tunnels or even buildings, land-mine detection, UXO (un-exploded ordinance) detection, etc [1]-[15].

The main reason of the exclusive use of UWB radar such as the impulse radar in SPR applications is due to the extremely wideband characteristic of the impulse type signal. Such a wideband signal includes both low frequency and high frequency components.

Meanwhile, desirable performance characteristics of SPR are long detection range and high range resolution. The UWB signal is adequate to achieve such desirable characteristics of SPR because many low frequency components of UWB signal enable long range detection and sufficient high frequency components enable high range resolution.

Typical signal waveforms used in the impulse radar are the monopolar (or Gaussian) impulse and the monocycle signal, which are depicted in Fig. 1.1 along with their frequency spectral shapes.

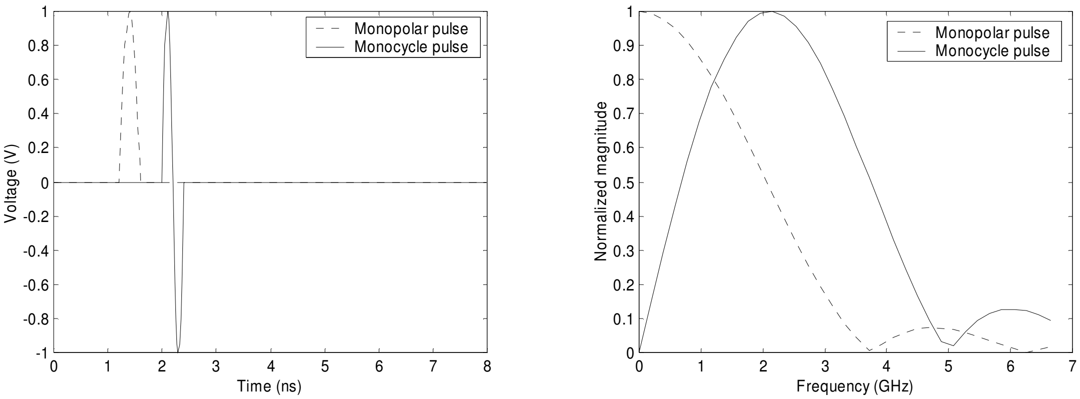

(a) (b)

Fig. 1.1. Waveforms (a) and spectral shapes (b) of the monopolar and monocycle pulse with 400-ps pulse duration.

The monopolar impulse is simplified here for comparison as a half cycle of a sinusoidal signal, and the monocycle pulse is defined as a single cycle of a sinusoidal signal. For comparison of spectral shapes of both signals, the same pulse duration of 400-ps is considered. As indicated in Fig. 1.1(b), the monopolar signal has about 4-GHz bandwidth, defining the bandwidth as a first null point on the spectrum, and its spectral components include a considerable quantity of DC and very low frequency components. The monocycle signal has about 5-GHz bandwidth, but in contrast to the monopolar pulse, no DC components, and much lower quantities of low frequency components are included in it. This difference in spectral shape of both signals, especially in terms of DC components, greatly affects the performance of the signal transmission efficiency of the wireless system using antennas. Since not all antennas can transmit the DC components or are efficient with very low frequency components, the signal transmission efficiency becomes much higher when no DC components are involved; thus the monocycle pulse shape is a better choice in the wireless transmission system. However, as the monocycle pulse has wider bandwidth, a system using it requires wider bandwidth as well, and the design of the monocycle pulse generator is more intricate and difficult.

The overall structure of the impulse radar and its operational concept are shown in Fig. 1.2. It is assumed that the radar system is applied to an arbitrary stratified dielectric substrate including an object. The impulse radar is used to detect reflected signals from each interface between layers. The first upper interface in Fig. 1.2 is formed between air and the first dielectric layer, and the second interface is formed between the first dielectric layer and the upper surface of the object, and so on. In general, the impulse radar consists of a transmitter, a receiver, antennas, and a DSP (Digital Signal

Processing) unit such as another radar system. Here I assumed a bistatic radar configuration formed by separated transmitting and receiving antennas, which is a commonly used antenna configuration in the impulse radar or SPR (Subsurface Penetrating Radar).

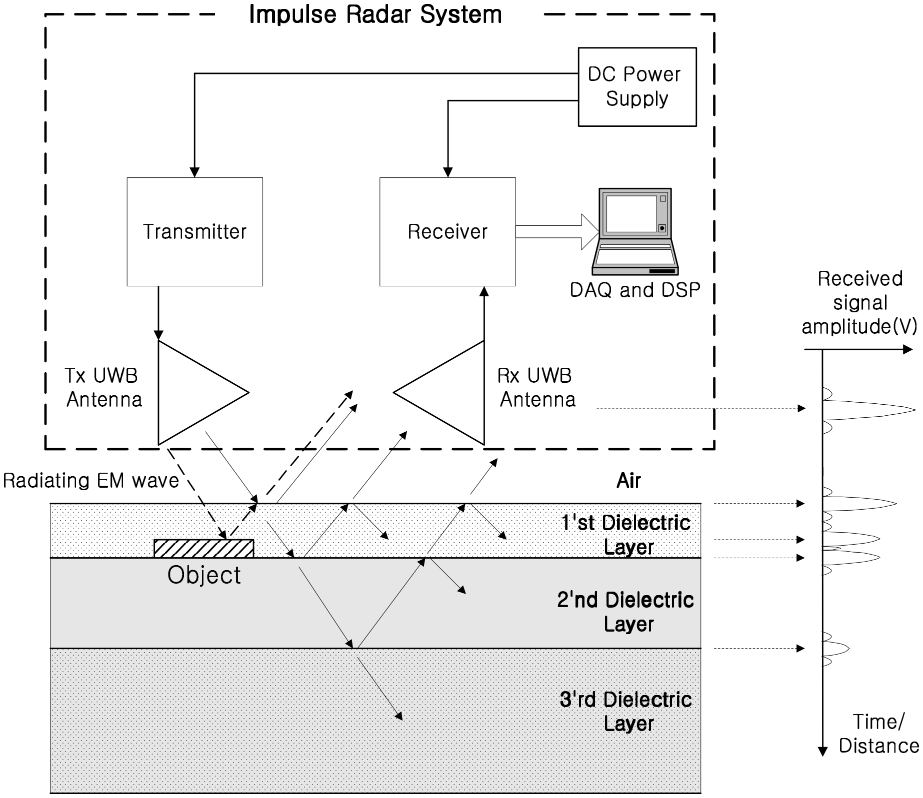

Fig. 1.2. Overall structure of the impulse radar used to identify the internal structure of a stratified substrate.

In Fig. 1.2, an electromagnetic (EM) pulse wave radiated from the transmitting antenna impinges on the surface of the substrate material. Part of the incident power to the surface will be reflected back and captured by the receiving antenna. Others will be transmitted into first dielectric layer. This kind of reflection and transmission will occur on every layer interfaces as described in Fig. 1.2, and some of the reflected power from each interface will be captured by the receiving antenna. The received signal from the receiving antenna can be represented in time domain as shown on the right-hand side of Fig. 1.2. Using this kind of received signals, we may identify the relative location of each interface and, eventually, the internal structure of the target substrate. Further signal processing such as image processing can give more obvious detection information for the object embedded in the substrate layers.

The goal of this research is to develop a prototype of a more advanced impulse radar system mainly for applications of short-range subsurface probing such as assessment of pavement and concrete structures, detection of buried mine and UXO, etc. Some of the pioneering work on the development of impulse radar for subsurface profiling was done by Daniels [4]. Recently, Azevedo and McEwan have developed a compact-size impulse radar sensor with low power consumption, the so-called micro-power impulse radar [10]. Duzdar and Kompa have also introduced an impulse radar sensor with 6-GHz of frequency bandwidth, which can be implemented at low cost and applied to high resolution ranging application [11]. Yarovoy et al. have developed a 3-GHz ground penetrating impulse radar and demonstrated its capability for the detection of small and shallow-buried objects [12], [13]. Lee had also developed an impulse radar system for subsurface penetrating radar applications and showed the potential for its application to pavement assessment [14], [15].

The development of an advanced impulse radar system may be divided into two different disciplines: microwave circuit and system design and digital signal processing. This research is mainly focused on the design of microwave circuits for transmitter, receiver, and antennas, and their integration into a microwave module. The signal processing technique required to implement the complete impulse radar system was investigated and a novel processing technique needed for the designed system will be introduced.

The transmitter and the receiver of the impulse radar were designed and implemented as microwave integrated circuits (MIC). Even though various microwave circuits for the impulse radar have been developed and are commercially available, new transmitter and receiver circuits were designed according to the following new motivations and requirements.

1) All circuits needs to be implemented as the planar circuit structure and to be as compact in size as possible to take into account its integration with an antenna.
2) The circuits should be fabricated with ease and low cost in hybrid MIC structure.
3) The transmitter must have tuning capability upon the output pulse duration, especially for the monocycle pulse signal, such that it may generate variable pulse durations with compact circuit structure.
4) The transmitter needs to generate the monocycle pulse signal with relatively high peak power and required short pulse duration.

5) The receiver circuit should have sufficiently low noise performance or low conversion loss, and wide operating frequency bandwidth to cover the transmitted signal frequency band.

The most outstanding feature of the designed system is that tuning (or selection) of the operating frequency band of the system was implemented by a novel electronically tunable transmitter with compact circuit structure. Variation in frequency band is obtained by variation in the pulse duration of the output monocycle signal. The tuning range of the designed transmitter is 450 to 1170 ps for pulse duration, which corresponds to a minimum of 0.15 to 1 GHz of frequency band and maximum 0.4 to 4 GHz of frequency band. The efficient tuning capability of the frequency band provides more flexibility in use of the sensor to detect layer interfaces or objects. A high frequency band can be used to obtain the higher resolution required for the detection of closely located interfaces. On the other hand, a low frequency band can be used to obtain the longer detection range. Using all of available frequency bands for a certain target, the multi-band operation of the sensor can give integrated effects from multiple frequency bands and render more information on the target structure. To implement the multi-band operation, proper signal processing and display format is necessary. The example of the multi-band operation will be shown in chapter VI. The designed transmitter can also generate 200 to 400 mW of output pulse peak power in monocycle form, which is relatively high output power and comparable with expensive commercial products.

The receiver of the impulse radar uses the synchronous sampling (or equivalent time sampling) technique to down-convert a high frequency signal with GHz bandwidth into a low frequency signal with KHz bandwidth [2], [3]. In view of the time domain, this is the same effect as reproducing the received fast-transient signal into a much slower signal, i.e. from sub-nanosecond duration to sub-millisecond duration.

The most critical component of the synchronous sampling receiver is the sampling mixer. The sampling mixer down-converts the RF signal into the IF (or baseband) signal according to the principle of sampling down-conversion, which is a well–known and efficient form of wideband down-conversion. The sampling mixer is the sample-and-hold circuit in which the voltage level of the RF input signal is sampled using supplied sampling strobe pulse, and the sampled voltage level is maintained in the holding capacitor. Unlike general microwave mixers, the sampling mixer is working with the strobe pulse LO (Local Oscillator) signal rather than CW (Continuous Wave) LO signal. The design of the short pulse generator for strobe pulse generation is therefore one of the main issues in the development of a fully integrated sampling mixer.

The sampling mixer should have the required bandwidth and low conversion loss in RF to IF conversion. The bandwidth of the sampling mixer should accommodate the bandwidth of the RF input signal for lower distortion. The major factor in determining the bandwidth of the sampling mixer is the strobe pulse duration. Therefore, the strobe pulse generator needs to generate a 100-ps order of pulse duration to obtain several GHz bandwidth of the sampling mixer. The large dynamic range of the sampling mixer is also important especially for impulse radar since the dynamic range of the RF input power incident to the receiver is as large as 30 to 40 dB.

A novel sampling circuit, called CSH (Coupled-Slotline-Hybrid) sampling mixer, was developed as a hybrid MIC for UWB applications. The circuit was fully integrated with the LO strobe pulse generator and the baseband circuit. The circuit structure of the CSH sampling mixer lends itself to easier fabrication than other designs; it is solid and more reproducible, and the performance is superior for impulse radar applications. The operating bandwidth of the CSH sampler is 5.5 GHz, the conversion loss is 4.5 to 7.5 dB (without amplifier), the conversion gain 6.5 to 9.5 dB (with amplifier) over the operating bandwidth, and the dynamic range is more than 50 dB.

The antenna is another critical component in the impulse radar system, affecting the detection performance of the system. The approach taken in this research is optimization of the known antenna structure to improve its performance and to accommodate required frequency band. There are many types of UWB antennas that can be used for an impulse radar, such as resistive loaded dipole antenna, spiral antenna, bow-tie antenna, and TEM (Transversal Electromagnetic) horn antenna. Since the TEM horn type antenna has better performance for pulse signal transmission, such as higher radiation efficiency, good gain, and most importantly linear phase characteristic and less dispersion, it has been used in common with impulse radars.

Recently, a novel TEM horn type antenna named microstrip quasi-horn (or quasi-horn) antenna has been reported, with a smaller physical size than a conventional TEM horn and simpler RF input feeding structure (in case of transmitting antenna) capable of being connected directly to the microstrip line or coaxial line. It also provides a handy structure for integrating with other components, such as the transmitter and the receiver by being attached to the ground plate that is a part of the microstrip quasi-horn antenna without any additional structure. Another important advantage of using quasi-horn antenna for an impulse radar stems from reducing the cross-coupling between transmitting and receiving antennas. This advantage is a main motivation for developing this kind of antenna rather than using a conventional TEM horn antenna. In a bistatic configuration of antennas located close to each other, the cross-coupled signal distorts reflected signals from layer interfaces or objects. The cross-coupled signal is therefore supposed to be removed in signal processing stage using the well-known technique of background signal subtraction, but it is not possible to remove it completely. The processing (or subtraction) error may increase the spurious signal level and false-alarm rate. An easy way of reducing such errors is to reduce the cross-coupled signal by means of modified antenna structure such as a microstrip quasi-horn antenna. The physical size of the antenna is a critical issue in system design, especially as low frequency antennas are so large that they dominate the overall size of the sensor system. The designed quasi-horn antenna has approximately half the size of a comparable TEM horn antenna.

The developed antenna can transmit and receive the full band of pulse signals (400-ps to 1200-ps pulse durations) generated by the designed transmitter. There is only inherent signal distortion, which is the first-derivation effect caused by the TEM-horn type transmitting antenna; however, this kind of distortion does not affect the detection performance of the system. There is no severe waveform distortion in the transmission of pulse signals through designed antennas, such as ringing of the pulse signal caused by the limited bandwidth of the antenna. The maximum achievable antenna gain of the designed antenna is about 15 dB for a single frequency, and the input VSWR is better than 2:1 from 0.5 to more than 6 GHz. Especially, the input reflected pulse signal from the designed antenna was measured for the input 450-ps monocycle pulse, and the result shows acceptable input return loss performance.

The signal received through the receiving antenna is down-converted by the sampling mixer, and the down-converted baseband signal is converted to a digital format by A/D converter. The digitized pulse signal normally contains both the cross-coupling signal and target reflected signals. Simple processing of background subtraction is used to remove the background cross-coupling signal. This technique is simple but very sensitive to jittering or the frequency modulation (FM) effect in the baseband detected signal. The main reason for FM in the baseband signal is due to the FM effect of the reference clock oscillators in the transmitter and the receiver, respectively. Very stable clock oscillators are therefore required to reduce the FM effect in the baseband signal. A different approach will be introduced to overcome the FM problem without incurring the extra cost of expensive stable oscillators, which is a simple but novel signal monitoring technique devised to improve the performance of signal processing using a background subtraction technique.

Subsequent chapters describe details of the circuit and the system design developed in this research. Chapter II focuses on system analysis to figure out the returned signal power, the required power budget, and the range resolution for the application of the pavement assessment, which is a primary application of the designed system. Chapter III describes the transmitter design, focusing on how to design the high power pulse generator and the electronically tunable monocycle pulse generator. Chapter IV introduces a novel sampling mixer design for UWB applications and the design of a synchronous sampling receiver system along with a subsidiary UWB LNA design. Chapter V focuses on optimized UWB antenna design pertaining to the microstrip quasi-horn antenna. Chapter VI is concerned with system integration using the developed components, with emphasis on the integrated microwave module and the signal processing unit. Test and evaluation results demonstrate the performance of the designed system for some sample target structures. Finally concluding remarks are given along with some recommended future work for improvement to the system.

CHAPTER II

SYSTEM ANALYSIS

Fundamental questions for the design of a radar system are how much transmitting power is needed and how good a resolution is required to distinguish different targets. For SPR (Subsurface Penetrating Radar) applications to investigate multiple stratified medium, another important question likely to be raised is how the radiated EM (Electromagnetic) wave propagates and is reflected in the stratified medium, and what its effect on the received signal is.

A system analysis was done to find answers for these problems related to the design of an impulse radar system. The analysis assumed a specific medium structure to be investigated, which is the pavement structure, since the primary application of the designed system is assumed to be the pavement assessment. The analysis result will be a reference specification for all components of the impulse radar to be designed, which are the transmitter, the receiver, and the antenna. The result may also be useful and applied to implementing the system using commercially available components.

The purpose of this analysis is to make a rough estimation of the required power budget and range resolution of the system so that we do not have to delve deeply into the analysis and design of the impulse radar system because it requires a wide and accurate range of information for the target media and more sophisticated modeling of transmission and reflection of EM wave in the medium. More generic and in-depth analysis and design of the subsurface penetrating radar can be found in the literature.

The main purpose of the power budget analysis is to estimate the required transmitting power. There are two different approaches available. One approach developed by Daniels is the method of factorization of total loss [3]. The other, developed by Annan and Davis, is the range analysis of the SPR [16], [17]. Since Daniels' approach is simpler and more appropriate to our purpose, the power budget analysis in this research was based on Daniels'. In the description of the power budget analysis, the multiple reflection phenomenon of the radiated EM wave is considered and its effect appearing on the received signal is described.

The resolution of the impulse radar system is determined predominantly by the radiating pulse duration. An estimation of the required minimum pulse duration is derived through the range resolution analysis based on the minimum thickness of the pavement structure.

A. Power Budget Analysis

The power budget analysis involves estimating minimum required transmitter output power to detect the reflected signal from an interest object, in our case, an interface between two adjacent layers in a stratified medium. Fig. 2.1 illustrates the situation where a radar sensor illuminates a pavement structure and receives reflected power from the second interface.

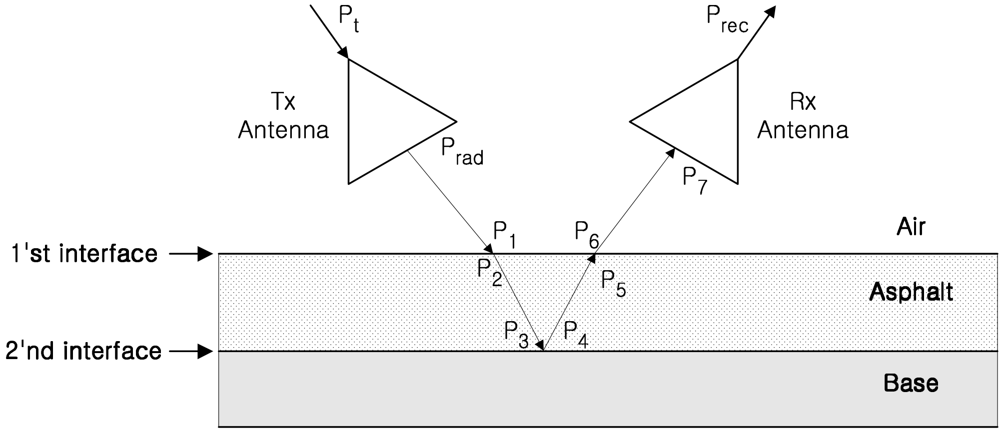

Fig. 2.1. Simplified power flow diagram of the impulse radar system for a pavement structure.

In Fig. 2.1, the total power flow from the transmitter to the receiver is represented by a power flow diagram that consists of subdivided power factors. Each power component is defined as follows; P_t: transmitter output power, P_{rad}: radiated power from the transmitting antenna, P_1: incident power from air to asphalt, P_2: transmitted power from air to asphalt, P_3: incident power from asphalt to base, P_4: reflected power on the 2'nd interface, P_5: incident power from asphalt to air, P_6: transmitted power from asphalt to air, P_7: incident power into the receiving antenna, P_{rec}: received power from the receiving antenna.

The received power can be expressed as (2.1) in dBm, where the total loss L_t is defined as (2.2). The receiver sensitivity, S_i, in dB form thus can be represented as (2.3) using the minimum required transmitter power, $P_{t,min}$ instead of a transmitter power, P_t in (2.2).

$$P_{rec}\left(dBm\right)=P_t+L_t \tag{2.1}$$

$$L_t\equiv\frac{P_{rec}}{P_t} \tag{2.2}$$

$$S_i\left(dB\right)=P_{t,min}+L_t \tag{2.3}$$

From (2.3), we recognize that the minimum required transmitter power, $P_{t,min}$ can be obtained by knowing the total loss, L_t, and the receiver sensitivity, S_i, which is determined by the receiver performance. The main problem to obtain $P_{t,min}$ is the calculation of the total loss, L_t. The total loss can be factorized as (2.4) using the power factors defined in Fig. 2.1.

$$L_t=\frac{P_{rec}}{P_7}\frac{P_7}{P_6}\frac{P_6}{P_5}\frac{P_5}{P_4}\frac{P_4}{P_3}\frac{P_3}{P_2}\frac{P_2}{P_1}\frac{P_1}{P_{rad}}\frac{P_{rad}}{P_t} \tag{2.4}$$

Each term of (2.4) can be grouped into several loss factors according to the cause of the loss. According to Daniels' terminology, the loss factors contained in (2.4) are to be the antenna loss (L_{ant}), the spreading loss (L_s), the material attenuation loss (L_a), the transmission coupling loss (L_{t1}), the retransmission coupling loss (L_{t2}), and the target scattering loss (L_{sc}). These loss factors are related to each term of (2.4) as shown in (2.5a) to (2.5e).

$$L_{ant} = \frac{P_{rec}}{P_7}\frac{P_{rad}}{P_t} \tag{2.5a}$$

$$L_s L_a = \frac{P_1}{P_{rad}}\frac{P_3}{P_2}\frac{P_5}{P_4}\frac{P_7}{P_6} \tag{2.5b}$$

$$L_{t1} = \frac{P_2}{P_1} \tag{2.5c}$$

$$L_{t2} = \frac{P_6}{P_5} \tag{2.5d}$$

$$L_{sc} = \frac{P_4}{P_3} \tag{2.5e}$$

Notice that the antenna loss (L_{ant}) represents the total loss incurred by both of transmitting and receiving antenna. The loss of each antenna can be divided further into the antenna efficiency (L_e) and the antenna mismatch loss (L_m). For instance, the antenna loss occurred by transmitting antenna can be represented as (2.6),

$$\frac{P_{rad}}{P_t} = \left(\frac{P_{rad}}{P_a}\right)\left(\frac{P_a}{P_t}\right) = L_e L_m \tag{2.6}$$

where P_a is the accepted power from the transmitter. Using these definitions for loss factors, the total loss, L_t, can be represented as (2.7) in terms of loss factors.

$$L_t(dB) = 2L_e + 2L_m + L_s + L_a + L_{t1} + L_{t2} + L_{sc} \tag{2.7}$$

Now we need to derive a detail model of each loss factors in order to calculate the total loss. The antenna efficiency (L_e) and mismatch loss (L_m) can be assumed simply as -1 dB, respectively, since a well designed antenna can achieve such a low loss. The other loss factors will be elaborated in sequence.

1) Spreading loss (L_s)

The spreading loss always occurs for any radiating EM wave because the power density of the radiating wave is reduced with the propagation distance. The well-known radar equation written in (2.8) represents the spreading loss in generic form for a bistatic radar configuration [18],

$$\frac{P_{ra}}{P_{ta}} = \frac{A_{et}A_{er}\sigma}{4\pi R^4 \lambda^2} \tag{2.8}$$

where P_{ra} is the received power on the antenna, P_{ta} is the radiated power from the antenna, A_{et} and A_{er} represent the effective aperture of the transmitting and receiving antenna, respectively, σ is the RCS (Radar Cross Section) of the target, R is the range from the radar to the target, and λ is the wave length. The RCS value σ is not considered in the spreading loss here, and it will be dealt with as the target scattering loss term later. After factoring out the RCS term, equation (2.8) can be simplified as,

$$L_s = \frac{G_t A_{er}}{\left(4\pi R^2\right)^2} \tag{2.9}$$

where G_t is the transmitting antenna gain. Equation (2.9) indicates that the spreading loss is a function of the inverse 4th power of the range. This relationship with the range is reasonable only for a point reflector type target. However, in the case of a planar reflector type such as ground interface, the spreading loss expression needs to be modified and can be approximated as,

$$L_s = \left.\frac{P_7}{P_{rad}}\right|_{L_a=0dB} \cong \frac{G_t A_{er}}{(4\pi)^{3/2} R^2} = \frac{G^2 \lambda^2}{(4\pi)^{5/2} R^2} \tag{2.10}$$

where L_s is also expressed in terms of power factors, P_7 and P_{rad}, defined in Fig. 2.1, and indicating that no material attenuation effect is involved. Additionally, G is the antenna gain when the same transmitting and receiving antenna are used. Notice that the wave length λ is not a single value for the situation of wave propagating in a homogeneous medium such as depicted in Fig. 2.1. In the actual calculation of the spreading loss, however, λ is assumed as a single value pertaining to the homogeneous medium of free space so as to simplify the analysis.

2) Material attenuation loss (L_a)

The EM wave propagating in a lossy medium experiences the loss or attenuation of its power. The attenuation factor of a lossy material can be found in the expression for the complex propagation constant γ of the lossy material [19],

$$\gamma = \alpha + j\beta = j\omega\sqrt{\mu\varepsilon'\left(1 - j\frac{\varepsilon''}{\varepsilon'}\right)} \tag{2.11}$$

where α and β are attenuation and phase constant, respectively, ε' and ε'' are real and imaginary parts of the complex dielectric constant for lossy material, μ is the permitivity of the material, and ω is the radian frequency. The attenuation constant α of a material can be obtained by expansion of (2.11),

$$\alpha = \omega\sqrt{\frac{\mu\varepsilon'}{2}\left(\sqrt{1 + tan^2\delta} - 1\right)} \tag{2.12}$$

where $\tan\delta$ is the loss tangent of the material. The quantity of loss is measured in common by exponential function of α such as,

$$Loss = e^{-\alpha R} \tag{2.13}$$

where R is the distance of EM wave propagating. Representing the loss quantity in units of Np, Loss = $-\alpha R$ and in dB, Loss = $-\alpha R(8.686)$. Therefore the material attenuation loss, L_a, in dB for propagation distance R can be expressed as (2.14) using (2.12).

$$L_a\left(dB\right) = -8.686\varpi R\sqrt{\frac{\mu\varepsilon'}{2}\left(\sqrt{1+tan^2\delta}-1\right)} \tag{2.14}$$

3) Transmission coupling loss (L_{t1}), retransmission coupling loss (L_{t2}) and target scattering loss (L_{sc})

Transmission coupling loss (L_{t1}), retransmission coupling loss (L_{t2}), and target scattering loss (L_{sc}) are related to the reflection and transmission phenomena of the EM wave on the interface of two different adjacent media. In the application of the SPR, the medium to be investigated such as the pavement structure consists of multiple layers of material as shown in Fig. 2.1; thus, complicated multiple reflections and transmissions may occur on the multiple interfaces. This situation is illustrated in Fig. 2.2 in the form of a reflection-transmission diagram [6].

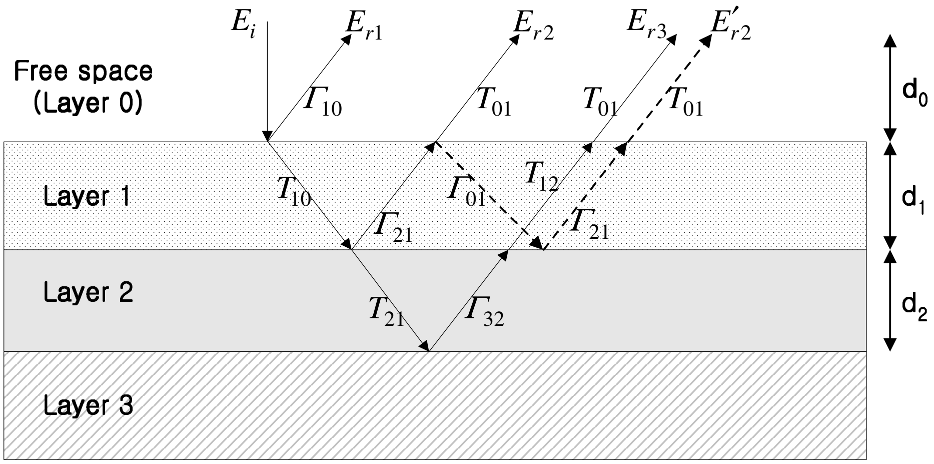

Fig. 2.2. Simplified reflection-transmission diagram for an electric field impinged to a pavement structure.

In Fig. 2.2, it is assumed that a radiated electric field from the antenna impinges on the surface of the stratified medium in normal direction. To simplify the problem, we do not consider the oblique incidence of an EM wave with parallel or perpendicular polarization. In Fig. 2.2, E_i represents the incident electric field intensity into the surface. E_{rk}, where k is an integer, represents the returned electric field intensity by reflection occurring at the kth interface. E_{rk}' also represents the returned intensity from kth interface, but it is coming out from double reflections at the kth interface, unlike a single reflection included in E_{rk}. T_{mn} represents the transmission coefficient for the transmitted signal from nth layer to mth layer. Similarly, Γ_{mn} represents the reflection coefficient for the incident signal from nth layer to mth layer. The diagram depicted in Fig. 2.2 is simplified and does not include all possible reflection and transmission pairs, but only includes critical pairs that significantly contribute to producing a detectable returned signal.

Using the diagram from Fig. 2.2, we can obtain expressions for the returned electric field intensities with respect to the incident field intensity, E_i, as shown in (2.15a) to (2.15d).

$$\frac{E_{r1}}{E_i} = \Gamma_{10} \tag{2.15a}$$

$$\frac{E_{r2}}{E_i} = T_{10}\Gamma_{21}T_{01} \tag{2.15b}$$

$$\frac{E_{r3}}{E_i} = T_{10}T_{21}\Gamma_{32}T_{12}T_{01} \tag{2.15c}$$

$$\frac{E'_{r2}}{E_i} = T_{10}\Gamma_{21}\Gamma_{01}\Gamma_{21}T_{01} = T_{10}\Gamma_{21}^2\Gamma_{01}T_{01} \tag{2.15d}$$

Notice that the returned field intensity including double reflections at the 2'nd interface, E_{r2}', expressed in (2.15d), is much smaller than others because, in the case of most SPR applications, the magnitude of the reflection coefficient is much smaller than that of the transmission coefficient, and Equation (2.15d) includes reflection coefficients three times as high than in others, which means that the resulting magnitude value of (2.15d) is much smaller than others, and can be ignored. A general form of the equations involving a single reflection can be written as (2.16).

$$\frac{E_{rn}}{E_i} = \Gamma_{n(n-1)}\left[\prod_{m=1}^{n-1}\left(T_{m(m-1)}T_{(m-1)m}\right)\right] \tag{2.16}$$

To calculate the returned field intensity using (2.16), we need to know each reflection and transmission coefficient term. The reflection and the transmission coefficients are represented as (2.17a) and (2.17b), respectively, for normal incident EM wave [19],

$$\Gamma_{n(n-1)} = \frac{\eta_n - \eta_{n-1}}{\eta_n + \eta_{n-1}} \tag{2.17a}$$

$$T_{n(n-1)} = \frac{2\eta_n}{\eta_n + \eta_{n-1}} \tag{2.17b}$$

where η_n is the intrinsic impedance of the material of nth layer. The intrinsic impedance of the lossy material is a complex value in general; therefore, the reflection and transmission coefficients for the lossy material are also complex values in general according to (2.17a) and (17b). To simplify the analysis, however, the intrinsic impedances are assumed as real values because common pavement materials of interest in subsurface radars can be considered as low-loss and non-magnetic materials [6], and the magnitude of the imaginary factor of the actual intrinsic impedance ($\varepsilon_r'' / 2\varepsilon_r'$) [19] is much less than 1, so that it may be ignored.

The loss factors related to the reflection and transmission of the signal are divided into 2 groups; one is related to the reflection, which is L_{sc}, and the other is to the transmission, which are L_{t1} and L_{t2}. Since the reflected power from the target is related to the RCS of the target as well as the reflection coefficient, the target scattering loss L_{sc} is defined as [3],

$$L_{sc} = \frac{P_{ref}}{P_{inc}} = \sigma \left| \Gamma \right|^2 \tag{2.18a}$$

$$L_{sc}\left(dB\right) = 20 log \left| \Gamma \right| + 10 log\, \sigma \tag{2.18b}$$

where P_{ref} is a reflected power , P_{inc} is an incident power, and σ is the RCS of the target. Since the RCS value of a dielectric half-space such as the ground interface is known as 1 [3], it can be ignored in our case. The target scattering loss is therefore only the multiplication of reflection coefficients on the signal propagation path. The transmission and retransmission coupling loss, L_{t1} and L_{t2}, are in general the multiplication of the transmission coefficient values on 2 different propagation paths respectively; one is in a downward direction and the other in an upward direction. As a result, equation (2.16) turns out to be the total loss including all loss factors related to the signal reflection and transmission effect on a single returned signal, E_{rn}. This new total loss factor is defined as the transmission loss L_u,

$$L_u\left(dB\right) = L_{sc} + L_{t1} + L_{t2} = 20\,log\left(\left|\frac{E_{rn}}{E_i}\right|\right) \tag{2.19}$$

4) Required minimum transmitting pulse power

All equations for loss factors consisting of the total loss are derived; but to calculate loss factors, we need to know parameter values characterizing the objective medium. Our primary objective medium, the pavement structure, has normal physical dimensions as summarized in Table 2.1. The pavement structure consists of an asphalt base and sub-base in downward direction.

Table 2.1. Normal thickness values of each layer of the pavement structure.

Type of the layer	**Thickness (in)**	**Thickness of a typical structure (in)**
Asphalt	2 to 10	6
Base	4 to 14	10
Sub-base	N/A	8

In Table 2.2, the electromagnetic properties of each layer of the pavement structure are summarized. The definition of $\varepsilon_r^{'}$ and $\varepsilon_r^{''}$ in Table 2.2 comes from the definition of the complex dielectric constant,

$$\varepsilon_c \equiv \varepsilon' - j\varepsilon'' = \varepsilon - j\varepsilon'' = \varepsilon_0\varepsilon_r' - j\varepsilon_0\varepsilon_r'' = \varepsilon_0(\varepsilon_r' - j\varepsilon_r'') \tag{2.20}$$

where $\varepsilon=\varepsilon_0\varepsilon_r$, ε_0 is the permitivity of the free space, ε_r is the relative dielectric constant, and $\varepsilon_r=\varepsilon_r'$. The attenuation constant α in the table can be computed by using (2.12) and $\tan\delta=\varepsilon_r''/\varepsilon_r'$ by definition. The intrinsic impedance of each layer is an approximated real value as a low-loss dielectric material.

Table 2.2. Normal electromagnetic properties of each layer of the pavement structure.

Type of the layer	ε_r'	ε_r''	**α (Np/m) for 2GHz**	$\eta=\sqrt{\frac{\mu_0}{\varepsilon_0\varepsilon_r}}\ (\Omega)$
Asphalt	5 to 7	0.03 to 0.05	0.22 to 0.47	142 to 168
Base	8 to 12	0.3 to 0.8	1.8 to 5.9	108 to 133
Sub-base	20	N/A	N/A	84

Now we are ready to obtain the value of the required minimum transmitter power. The transmitter power should be sufficient to detect the most distant object which is, in our case, the 3’rd interface between base and sub-base layer of the pavement structure. Therefore the calculation of the required transmitter power should be based on the returned signal from the 3rd interface of the pavement structure.

Let us assume that the interesting frequency is 2-GHz as the center frequency of the transmitting pulse signal with 400-ps duration. The thickness of asphalt and base layers, which are depicted as d_1 and d_2 in Fig. 2.2, is assumed as 6-in and 10-in as maximum possible values, respectively. There is the additional thickness of the free space between the end of the antenna aperture and the top of the asphalt, which is depicted as d_0 in Fig. 2.2 and assumed as 10-in.

First, the spreading loss L_s can be calculated using (2.10). TEM horn type antenna is assumed to be used for obtaining higher antenna gain than for other types. The same antennas for transmitting and receiving are to be used, and the antenna gain G is assumed to be 10 dB. The range R is 50-in, which is the sum of d_0 d_1 and d_2. The calculation result is L_s= -22.6 dB.

Second, the material attenuation loss L_a can be calculated using (2.14), but here a slightly different approach is applied. The loss factor L_a can be defined in units of dB/m, not just in dB, such as L_a (dB/m) = -8.686α, where α is the attenuation constant of the material. Notice that two different materials, asphalt and base, are involved in our case. Two material attenuation loss factors in units of dB/m for two different materials are defined as L_{a1} and L_{a2}. Calculation results using maximum α values are provided in Table 2.2 are L_{a1}=-4.08 dB/m and L_{a2}=-51.2 dB/m. The wave traveling distance in each medium is twice of d_1 and d_2, which is $2d_1$=0.5 m, $2d_2$=0.7 m. Therefore, the total material attenuation loss in dB, $L_a = 2L_{a1}d_1 + 2L_{a2}d_2 = -37.9$ dB.

Third, we need to calculate the transmission loss L_u defined as (2.19). In our case we are interested in the detection of the 3rd interface, hence need to calculate $L_u=20\log(|E_{r3}/E_i|)$ using (2.15c). The reflection and the transmission coefficients included in (2.15c) can be calculated using (2.17a) and (2.17b). In this calculation, the intrinsic impedance value for each layer is assumed as $\eta_0=377$, $\eta_1=150$, $\eta_2=120$, $\eta_3=84$, based on the material property data in Table 2.2. The calculation result, $L_u=-17$ dB.

Finally, using the calculated loss factor values, the total loss can be obtained as, $L_t = 2(L_e+L_m)+L_s+L_a+L_u = -82$ dB, where the antenna efficiency L_e and the antenna mismatch loss L_m are assumed as -1 dB, respectively.

To obtain the minimum required transmitter power according to (2.3), we need to know the receiver sensitivity S_i as well as the total loss. The receiver sensitivity is selected as 8-dB tangential sensitivity, which is generally used for measurement systems [20]. The sensitivity is therefore [21],

$$S_i(dB) = kTBF + SNR_o = kTBF + 8 \tag{2.21}$$

where k is the Boltzmann constant, T is the absolute temperature in K, so that kT= -174 dBm/Hz at room temperature, B is the mixer bandwidth, F is the noise figure of the mixer, which may be assumed as the same value with the conversion loss of the mixer

[21], and SNR_o is the required output SNR (Signal-to-Noise Ratio), which is 8 dB for 8-dB tangential sensitivity. The calculation result for the sensitivity, S_i=-66 dB using B=5 GHz and F=3 dB.

Using (2.3) and the calculation result for the total loss and the sensitivity, the required minimum transmitter power is obtained as $P_{t,min}$=16 dBm. Note that this is the average power for the CW signal. For the pulse signal such as the monocycle pulse, we are interested in the pulse peak power or peak-to-peak voltage value (V_{pp}). The conversion result from average power to peak-to-peak voltage value is 4 V_{pp} for 50 Ω load, which is the required minimum voltage of the transmitter output pulse, and is equivalent to 80 mW of the peak power.

B. Range Resolution Analysis

The minimum range resolution is required only for the asphalt layer detection in the pavement assessment application because the asphalt layer has minimum thickness throughout the entire pavement structure. Let us assume that the minimum thickness of the asphalt we need to discern from the base layer is 1 in. The objective of this analysis turns out to be finding the minimum required pulse duration to achieve the required range resolution of 1-in. We can find the minimum required pulse duration T_p from the simple equation, $T_p=d_m/v_p$, where d_m is the minimum thickness of the asphalt layer and v_p is the phase velocity of the propagating EM wave at a certain frequency. In general

$v_p=\omega/\beta$ for a plane EM wave, where the phase constant β may be approximated for low-loss material as [19],

$$\beta \cong \omega\sqrt{\mu\varepsilon'}\left(1+\frac{1}{8}tan^2\,\delta\right) \cong \omega\sqrt{\mu\varepsilon'} \tag{2.22}$$

Therefore the phase velocity v_p can be approximated for low-loss non-magnetic material as,

$$v_p \cong \frac{1}{\sqrt{\mu\varepsilon'}} = \frac{1}{\sqrt{\mu_o\varepsilon_o\varepsilon_r'}} = \frac{c}{\sqrt{\varepsilon_r'}} \tag{2.23}$$

Using (2.23), we can show that the phase velocity in the asphalt layer is from 4.46×10^9 to 5.28×10^9 in/sec for the dielectric constant values of the asphalt specified in Table 2.2. Finally we can calculate the minimum required pulse duration $T_p \cong 200$ ps. However, this short pulse duration value does not take into account the actual waveform shape in the detection stage. Considering the actual received waveform from the receiving antenna, the minimum required pulse duration to achieve required range resolution is not the same as the transmitting pulse duration.

Assuming that TEM horn type antennas are used for the transmitting and the receiving antennas of the impulse radar system, the radiating electric field intensity is in the form of the first derivative of the driving current [2], [22]; therefore, for the driving current with monocycle pulse shape, the received waveform through the receiving antenna becomes similar to the approximated Sinc-function, as shown in Fig. 2.3.

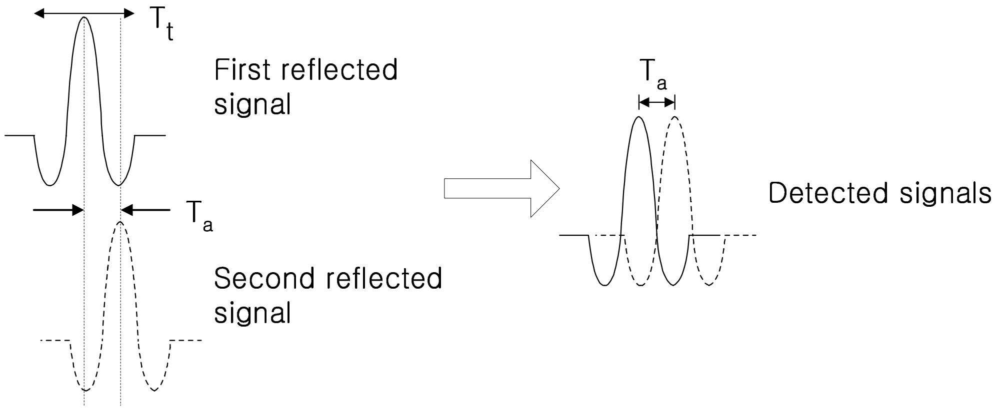

Fig. 2.3. Two detected signals with minimum discernable time interval in actual receiving situation through a TEM horn type antenna.

In Fig. 2.3, we are considering the situation in which two reflected signals from two different layer interfaces separated by the distance of minimum range resolution are detected in series. The first reflected signal in Fig. 2.3 is the reflected signal from the first interface, and the second reflected signal is from the second interface. The pulse duration T_t can be considered as the same as that of the transmitting pulse, ignoring any small pulse stretching effect of a well-designed antenna. As shown in the waveform of the detected signals in Fig. 2.3, the minimum time interval T_a is required to discern two detected signals without overlap in the pulse main-lobes. Therefore T_a is equivalent to the minimum required pulse duration, T_p, after taking account of the real waveform. T_a

is about half of the transmitting pulse duration $T_{t,}$ as shown in the Fig 2.5; hence the transmitting pulse duration T_t to achieve 1 in of the range resolution is twice the time of T_a (or T_p), which is about 400-ps.

CHAPTER III

TRANSMITTER DESIGN

The transmitter of the impulse radar is a pulse generator which generates an impulse type signal, in our particular case the monocycle pulse. The pulse generator should have proper performance to satisfy required specifications for impulse radar applications. The critical performance factors of the pulse generator as a transmitter are the duration of the output pulse and its peak power. The duration of the output pulse should be small enough to satisfy the required resolution for adjacent target detection. The peak power of the output pulse is necessary to be high enough to detect long distance target in a medium. According to the system analysis of Chapter II, the required pulse duration is about 400-ps and the peak power should be greater than 80 mW which is corresponding to 4 $V_{p\text{-}p}$ in voltage amplitude of the pulse.

The output pulse of the generator should also have good intended shape (monocycle) with small distortion in the main pulse and small ringing in the tail (or side-lobe) of the main pulse. An additional desirable function of the pulse generator is its tuning capability to generate different pulse durations with constant peak power and pulse shape. Tunable pulse generator can give great flexibility in the operation of the impulse radar. The pulse with wider duration contains large low-frequency components, enabling the pulse signal to propagate deeply into a medium because of the relatively low propagation loss of its low-frequency components. The pulse with shorter duration, on the other hand, has wider frequency bandwidth making feasible higher range resolution. A pulse that can change its duration, especially by an electronic means, would therefore have both advantages of increased penetration (or range) and fine range resolution and is attractive for UWB systems. Electronically tunable pulse generators are also desired for measurement equipment. The polarimetric video impulse radar described in [12] and [13] is a good example showing the usefulness of tuning capability of the pulse generator.

Many kinds of pulse generators have been developed and applied for impulse radar applications. The pulse generators of the impulse radar are distinguished here by its output pulse peak power, pulse duration, and pulse shape. According to the peak power of the output pulse, the pulse generator can be divided into high power and low power pulse generator. A reference value of the peak power that can differentiate the high and low power pulse generator may be 500 mW which corresponds to 10 $V_{p\text{-}p}$ in peak voltage amplitude of the pulse. According to the pulse duration, the pulse generator can be divided into nanosecond and sub-nanosecond pulse generator. The output pulse duration of the nanosecond pulse generator is greater than 1 ns, which corresponds to the bandwidth of smaller than 1 GHz approximately. According to the pulse shape, the pulse generator can be divided into step function, impulse and monocycle pulse generator.

In most case of high power applications for long range detection, high-power pulse generators with impulse shape of nanosecond duration are commonly used. Even though the impulse shape is not efficient for antenna transmission, it is widely used because of easier and simpler implementation of the impulse generator than monocycle pulse generator. In our case, referring to the required specifications of the output pulse peak power and its duration, the desired pulse generator is categorized into the low-power sub-nanosecond monocycle pulse generator.

For high power impulse radar applications, such as deep-penetration ground penetrating radar (GPR), pulse generators have been commonly implemented by using avalanche transistors with or without a series stack of step-recovery diodes (SRD) [23]-[27]. Optoelectronic design using GaAs photoconductive semiconductor switch and electronic design using drift step-recovery diode (DSRD) and silicon avalanche shaper are also well known method for high-power pulse applications [28], [29]. These high-power pulse generators, however, have bulky, complicated structures and in some cases requires high DC bias voltage as much as 100 V. Devices such as DSRD are also difficult to find in commercial market. Currently available commercial products of high-power pulse generator have limited performance, whose achievable minimum pulse width is only about 1ns and the maximum output pulse repetition frequency (PRF) is usually about 1 MHz.

Research in efficient pulse generator design for low-power, short-range UWB impulse radar and communication systems has not attracted much attention, partly because of the availability of commercial products with good performance [30]-[32]. However, with the increasing demand of low-power and compact UWB systems, it is naturally desirable to have compact low-cost pulse generators. Especially, it is hard to find the tunable monocycle pulse generator, being able to be integrated with antenna and to be implemented with low-cost, in commercial products. The pulse generators proposed in [33], [34] provide relatively high output pulse power and handy tuning capability, but the output waveform is an impulse or a step function. The tunable pulse generators reported in [35] also produce impulses only. The monocycle pulse generators shown in [36]-[39] provide relatively low output power (20 mW of peak power) without tuning capability.

Through out the research, we have developed a novel sub-nanosecond tunable monocycle pulse generator for low-power short-range UWB applications. The developed monocycle pulse generator produces monocycle pulses with 10 MHz of PRF, tuning range of 0.4-1.2 ns for the pulse duration, corresponding approximately to 0.15 to 3.7 GHz operating frequency range. The output pulse amplitude is in the range of 6 to 9 $V_{p\text{-}p}$ equivalent to 200 to 400 mW of peak power, which is comparable to the output power of other commercial products.

The developed tunable monocycle pulse generator uses a single SRD (Step Recovery Diode) to form a fast transient rise-time, which is a commonly used approach for sub-nanosecond pulse generator design. Relatively high output pulse power is obtained by using high driving power for the SRD, provided by a driving circuit consisting of high-speed amplifier and buffer IC's. This design approach greatly simplifies the circuit design as compared to that using discrete components proposed in [40] and avoid using expensive high-power wideband MMIC at the output stage of the pulse generator as proposed in [38], [39]. In addition to using high driving power, high output power can be obtained by increasing the output power efficiency of the SRD pulse generator using proper DC biasing scheme for the SRD as described in [33], [40], [41]. In our generator, a novel coupling circuit for the SRD is designed to increase the output power efficiency. This circuit has the form of a first-order high-pass RC filter and does not require any external DC bias for normal operation. A decoupling circuit is also employed to reduce the ringing level of the output pulse.

The basic idea for realizing the monocycle pulse tuning ability relies on using PIN-diode switches proposed for tunable impulses [35]. The same tuning principle is extended to make a tunable monocycle rather than an impulse. In comparison with the tuning method using DC bias control for the SRD [33], the PIN diode switching method is simpler, facilitates the design of tunable monocycle pulse waveforms and provides convenient tuning operation. In the developed monocycle pulse generator, an impulse is generated first and a pulse shaping circuit is used to convert the impulse to a monocycle.

The first section discusses the design technique for the SRD impulse generator to obtain fast transient and improved output pulse power. Section B covers details of the design for the tunable monocycle pulse generator, including tuning technique for the pulse duration and the design of the decoupling circuit required for the monocycle pulse shaping. Section C describes the fabrication and performance of the tunable monocycle pulse generator.

A. Design of Delay-Line SRD Impulse Generator

The basic element in the developed tunable monocycle pulse generator is the delay-line impulse generator. Formation of an impulse using delay line is a classical technique used in the digital or pulse circuit area. Some SRD impulse or monocycle-pulse generators have been designed using the same delay-line principle and implemented on microstrip or CPW structures [36]-[39], [42]. Another type of SRD impulse generator, extensively used for sub-nanosecond pulse generation and microwave multiplier, is the shunt-mode SRD impulse generator [43]-[47].

Before beginning the circuit design, important SRD characteristics affecting circuit performance of the impulse generator need to be identified. One of the important characteristics is the transition time of SRD that determines the minimum achievable pulse's transition time. The other is the minority carrier lifetime (MCLT) of the SRD, which affects the storage time under reverse bias condition. If a clock signal is applied to the SRD pulse-shaping circuit, the rise time of the clock should be less than the MCLT of the SRD in order to obtain maximum achievable pulse amplitude [28]. In our design, the SRD is selected for 70-ps transition time and 10-ns MCLT, assuming that the output pulse duration to be generated is 200 ps and the rise time of the clock is 10 ns.

Fig. 3.1 shows the overall circuit diagram of the designed impulse generator. It can be subdivided into the clock driving, the SRD coupling and the pulse shaping circuit according to their functions. The clock driving circuit consists of a clock oscillator, a non-inverted opamp voltage amplifier and two current boosting buffers. The clock oscillator generates a TTL compatible clock signal with 5 ns of rise time and about 10 MHz of PRF. This fast rise-time clock signal is required according to the MCLT of the selected SRD.

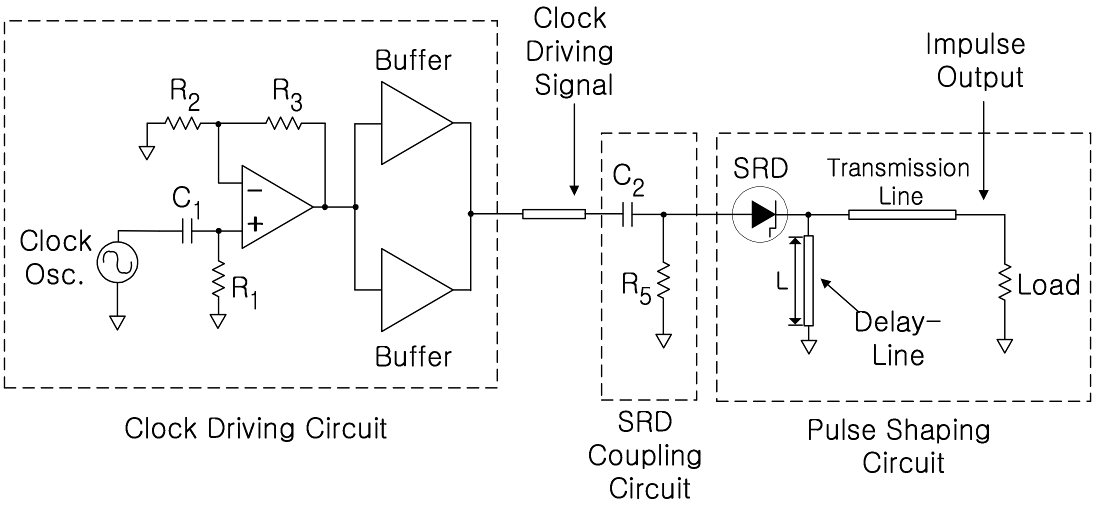

Fig. 3.1. Circuit diagram for the designed SRD delay-line impulse generator.

High voltage of the clock driving signal for the SRD, indicated in Fig. 3.1, produces large amplitude for the output impulse. To increase the driving signal voltage level, the input clock signal is amplified by amplifier and buffers. The desired voltage level of the driving signal is set as 20 $V_{p\text{-}p}$, taking into account the selected SRD having 15 V of breakdown voltage. The amplifier is designed to have voltage gain of 4 in order to obtain 20 $V_{p\text{-}p}$ from a 5 $V_{p\text{-}p}$ TTL input signal and bandwidth of 100 MHz using a wideband opamp with 400-MHz unity-gain bandwidth in order to prevent the input rise time from slowing down. The buffer is used to supply the SRD, representing a low-impedance load, with enough current to obtain a high output voltage swing of 20 $V_{p\text{-}p}$ and to reduce large loading effect on the amplifier. Two buffers are used to enhance the reduction of loading effect and to have some margin for its supplied current capacity. The loading circuit analysis, which will be shown below, determines the required current capacity for the buffers.

To produce an impulse having high amplitude and a transition as fast as possible, a proper DC bias can be applied to the SRD. The DC bias controls the quantity of the stored charge in the SRD through the forward-bias current, which determines the storage time and thus affecting the turn-off transition time when the SRD is reverse biased. The stored charge should be large enough to have a sufficient storage time so that a fast transition may occur at the maximum voltage level of the input clock signal. On the other hand, it should also be minimized to obtain as fast transition time as possible. In our design, we employ a SRD coupling circuit, as shown in Fig. 3.1, to avoid the use of an external bias network. The coupling circuit works effectively to control the quantity of the stored charge in the SRD. Detailed analysis of this circuit included in the following will explain this controlling effect and determine its optimal component values (R_5 and C_2 in Fig. 3.1)

An equivalent circuit for the delay-line impulse generator is shown in Fig. 3.2(a), in which the driving circuit in Fig. 3.1 is replaced by a voltage source with a source resistance. R_f represents the forward-biased resistance of the SRD. Fig. 3.2(b) displays the voltages and currents in Fig. 3.2(a).

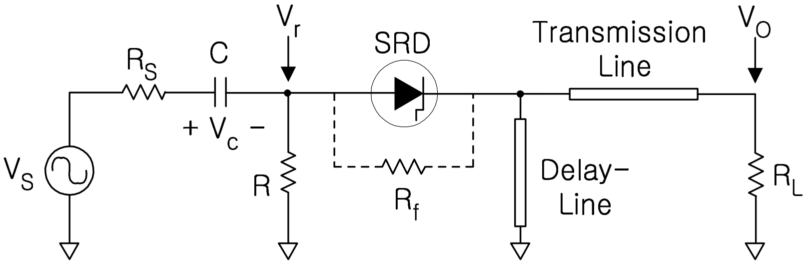

(a)

Fig. 3.2. Equivalent circuit of the SRD delay-line impulse generator (a) and the voltage and current waveforms occurred in the circuit (b).

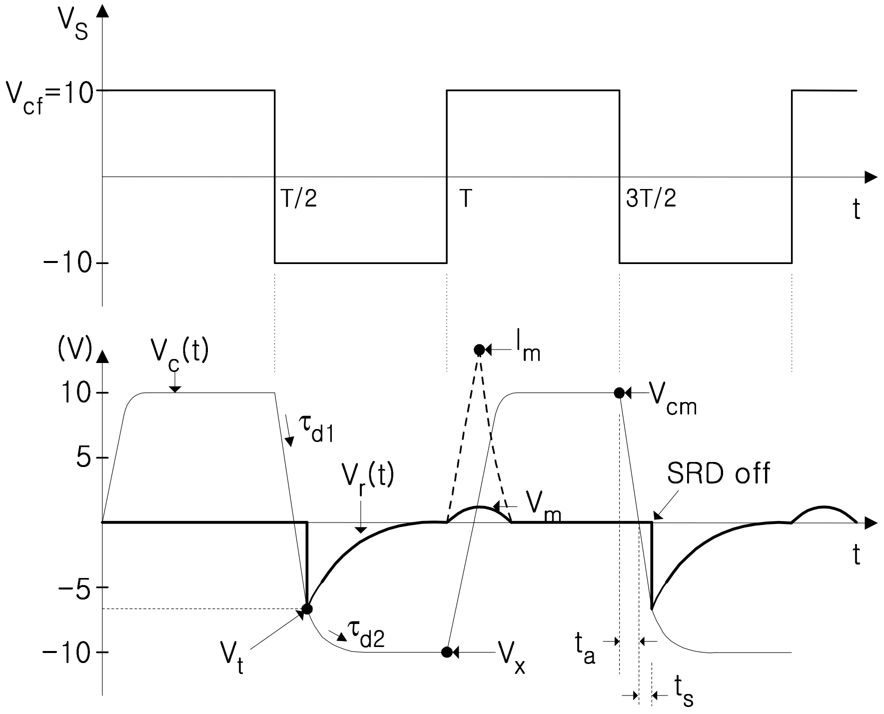

(b)

Fig. 3.2. Continued.

The source signal V_s is assumed as an ideal clock with instant transitions to simplify the analysis. The waveforms for V_c and V_r, defined in Fig. 3.2(a), are drawn by means of a basic transient analysis. In the waveform of $V_r(t)$ (input to the pulse shaping circuit), a fast transition occurred due to the turn-off of the SRD is illustrated. This transient is transformed to an impulse at the output by combining with the reflected one from the short-circuited transmission line representing the delay-line. The waveform of the forward-biased current flowing through the SRD, which determines the stored charge quantity, is also shown with a peak value of I_m.

Our design goal is to determine optimum values for the resistors (R's) and capacitors (C's) in the equivalent circuit to produce a maximum transient amplitude of V_t for $V_r(t)$, described in Fig. 3.2(b). The values for R's are determined qualitatively first as follows. To obtain sufficient storage time, the peak amplitude of the forward current, I_m, should be as large as possible. Since the forward current is proportional to the diode voltage,

$$I_m \propto V_m \propto -V_c\left(T^-\right)+V_s\left(T^+\right)=-V_x+V_{cf} \tag{3.1}$$

where V_{cf} is the peak voltage of the clock source that is 10 V in our case. From the relationship given in (3.1), in order to increase I_m, $|V_x|$ should be equal to V_{cf}. To increase $|V_x|$ and V_t, $\tau_{d2}=(R+R_s)C$ and $\tau_{d1}=(R_f+R_s)C$ should be decreased. Therefore, R, R_s and R_f should be as small as possible. However, R needs to be much greater than R_f to achieve a smooth transition after the fast diode turn-off transition in V_r. As a result, assuming R_f is equal to the series resistance of the SRD, which is 0.22 ohm in our case, R=10 Ω can then be selected as a reasonable value.

An optimal value for C can be found by deriving equations for the waveforms shown in Fig. 3.2(b) and solving them using an iterative optimization method. First, a small negative value for V_x is assumed as an initial value. From the rising and falling edges of the waveform $V_c(t)$, the following equations can be derived:

$$V_{cm} = V_{cf} + \left(V_x - V_{cf}\right)e^{-T/2R_f C} \tag{3.2}$$

$$V_t = -V_{cf} + \left(V_{cm} + V_{cf}\right)e^{-t_t/R_f C} \tag{3.3}$$

where $t_t=t_s+t_a$, with t_s and t_a being defined in Fig. 3.2(b), and T represents the clock period. The storage time t_s can be calculated from the fact that the stored charge in the SRD resulted from the forward current flowing is the same as the removed charge caused by the reverse current. Assuming the forward current is proportional to applied diode voltage, it's straightforward to derive the following equation for the stored charge Q_f:

$$Q_f \cong \frac{V_a\left(t_k\right)}{R_f}\left[\frac{t_k}{2} + R_f C\left[e^{-t_k/R_f C} - e^{-t_L/R_f C}\right]\right] \tag{3.4}$$

where $V_a(t)$ is the response of a ramp signal with a slew rate of m,

$$V_a\left(t\right) = mR_f C\left(1 - e^{-t/R_f C}\right) \tag{3.5}$$

where $m=|V_x|/t_k$. t_k is a half of the rise time t_r of the clock source and t_L is the MCLT of the SRD. Similarly, the removed charge quantity Q_r can be derived for two distinct cases. For $t_s \leq t_r$,

$$Q_r \cong \frac{V_a(t_s)}{2R_f} t_s \tag{3.6}$$

where m=|V$_{cm}$|/t$_k$. For $t_s > t_r$,

$$Q_r \cong \frac{V_a(t_k)}{R_f}\left[\frac{t_k}{2} + R_f C\left[e^{-t_k / R_f C} - e^{-t_s / R_f C}\right]\right] \tag{3.7}$$

The estimate of t_s can now be obtained by an iterative optimization method using the following criterion:

$$\hat{t}_s = arg\left(\min_{t_o \le t \le t_L} \left|Q_f - Q_r\right|\right) \tag{3.8}$$

where t_o is a small time step used in the iteration process. From (3.3), with the condition of V_t=0,

$$\hat{t}_a = -R_f C\left[ln\left(\frac{V_{cf}}{V_{cm} + V_{cf}}\right)\right] \tag{3.9}$$

Using a negative part of the waveform $V_c(t)$ corresponding to the portion after the SRD turn-off transition, the updated estimate value of V_x can be calculated as

$$\widehat{V}_x = -V_{cf} + \left(V_t + V_{cf}\right)e^{-\left(\frac{T}{2}-t_t\right)/RC} \tag{3.10}$$

Finally, the estimate of V_t can be obtained using the following criterion:

$$\widehat{V}_t = arg\left(\min_{n\to\infty}\left|\widehat{V}_x(n) - \widehat{V}_x(n-1)\right|\right) \tag{3.11}$$

where n represents the number of iterations in the optimization procedure. Results from the simulation and measurement are given in Fig. 3.3. Fig. 3.3(a) shows calculated values for the negative charging voltage V_x and the transient step voltage V_t along with the measured impulse amplitude as a function of the capacitance values of the RC coupling circuit. The simulation result for the step amplitude V_t shows a consistent trend with the measured impulse amplitude, thus validating the simulation. From this result, an optimal value for C can be chosen within the range of 0.2 ~ 1 nF. The simulation results for the stored and removed charge quantities, shown in Fig. 3.3(b), confirms the fact that $Q_F \approx Q_R$, and hence verifies the convergence of the simulation. C=200 pF is chosen as an optimal value based on the result in Fig. 3.3(b) considering the fact that smaller stored charge makes faster transition.

The required current capacity for the current boosting buffer can be calculated approximately based on the previous analysis. The loading circuit for the buffer is the same as that shown in Fig. 3.2(a) and the voltage waveform applied to the load is the same as $V_r(t)$ in Fig. 3.2(b). Assuming R=12 Ω, C=1 nF, and $R_s+R_f=1$ Ω, the peak voltage amplitude with respect to the forward current is calculated as 2.77 V using (3.5). The required positive average current can then be calculated as 173 mA. Similarly, the negative average current required is determined as 210 mA. This result shows that the two parallel-connected current buffers, each with ±250 mA of output current capacity, can satisfy the driving current requirements with some design margin.

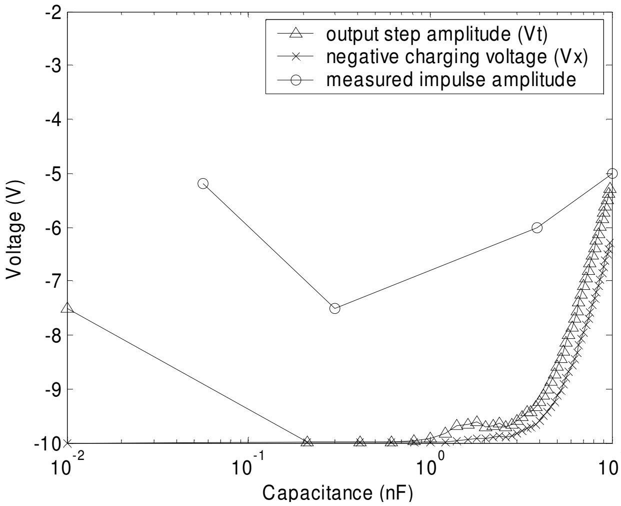

(a)

Fig. 3.3. (a) Calculated and measured voltages for the designed delay-line impulse generator. (b) Calculated results for the stored and removed charge quantities in the SRD.

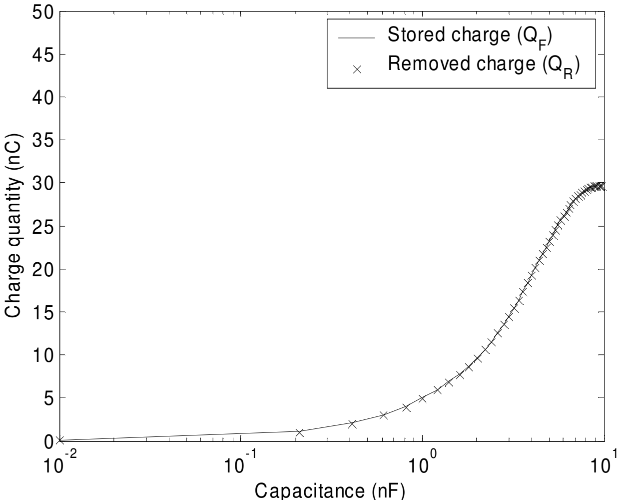

(b)

Fig. 3.3. Continued.

B. Design of Tunable Monocycle Pulse Generator

The tuning method used in our design is based upon the PIN diode switching method described in [35] for impulse generation. Here it is extended to generate various monocycle pulse durations. The underlying principle of the tuning method using PIN diode switching is relatively simple. Fig. 3.4(a) shows an instance of the distributed delay-line for tuning of the impulse duration. The original delay-line, seen in Figs. 3.1 and 3.2(a), is subdivided into several transmission-line sections, separated by DC blocking capacitors, to form a distributed delay-line with each section containing an anti-parallel PIN-diode pair and a biasing circuitry. A synthetic short-circuit can be created at each diode-pair connection point by turning on the PIN diodes through a DIP switch. By changing the DIP switch connections alternately, various delay-lines of different lengths can be effectively made, hence generating different impulse durations corresponding to different round-trip times of the step signal propagating on the delay-line. Use of a pair of anti-parallel PIN diodes, instead of a single diode, at each junction along the delay-line is explained in Fig. 3.4(b). Let's assume a positive step pulse arrives at junction A on a delay-line section and both the PIN diodes are turned on. Assuming further that the step pulse is a large signal, then only two anti-parallel connected PIN-diodes can support opposite current directions required by the incident and reflected step pulses. An anti-parallel PIN diode-pair configuration, therefore, creates a synthetic short-circuit closer to the ideal one than a single-diode configuration for large signal input. The other advantage of using a pair of PIN diodes is that one of the diodes can be placed on the side of the bias circuit to reduce the coupling of the incident pulse to the bias circuitry, resulting in better isolation than using a large resistance for biasing and isolation purposes. Moreover, using two diodes supports the balance of the circuit configuration.

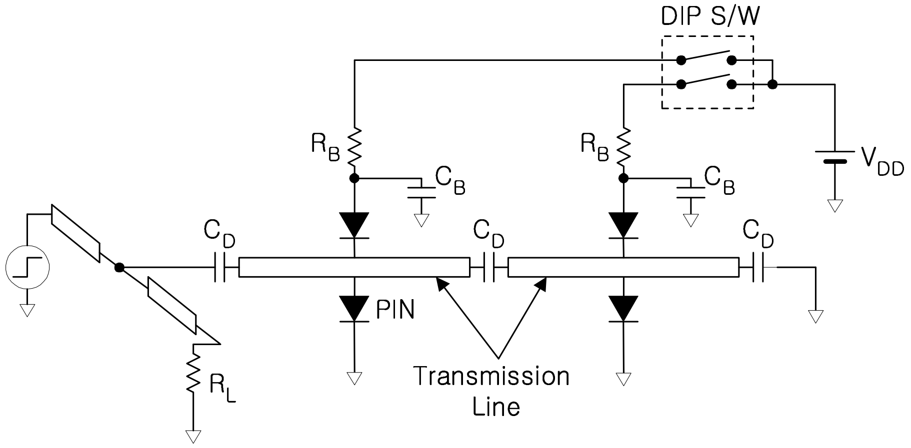

(a)

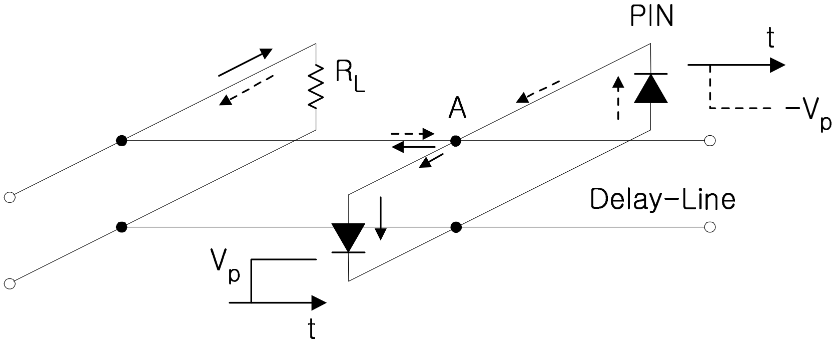

(b)

Fig. 3.4. (a) Circuit diagram for a distributed delay-line using anti-parallel PIN diode pairs. (b) Illustration showing the principle of using a PIN-diode pair to obtain a synthetic short-circuit. The solid- and dashed-line arrows represent current flows corresponding to the positive and negative step voltage transients, respectively.

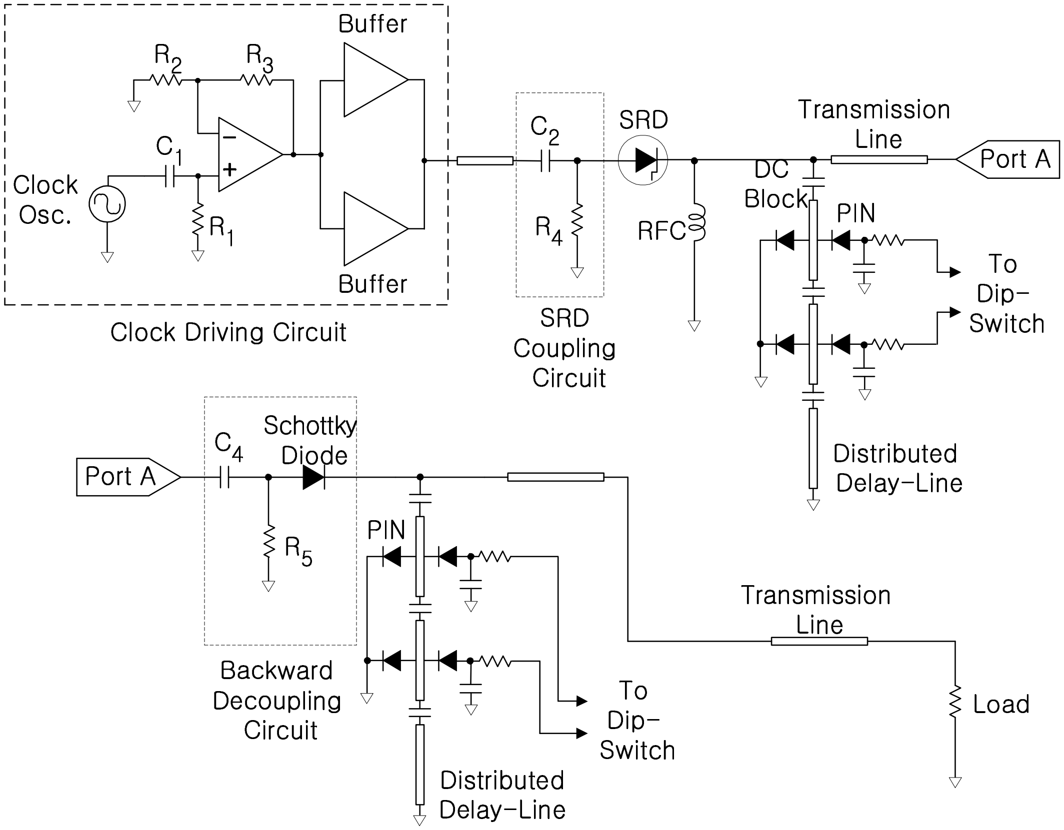

Fig. 3.5. Circuit diagram for the designed tunable monocycle pulse generator.

Fig. 3.5 shows a simplified overall circuit diagram for the designed tunable monocycle pulse generator. The clock-driving and the SRD coupling circuits have the same configurations as those for the impulse generator described in Section II. A broadband RF choke (RFC) is used to provide a return for the low-frequency clock driving signal to the ground, which is necessary in order to create a similar loading circuit as in the impulse generator design, so that the previous design result for the driving and coupling circuits of the impulse generator may be applied directly to the monocycle pulse generator. The RFC used in our design is ADCH-80A manufactured by Mini-Circuits Co.

Two distributed delay-lines with identical configuration are used for tuning of the monocycle pulse duration. The first one is used for formation of various impulse durations. The other is used for controlling the round-trip time of the generated impulse, which results in monocycle pulses with different durations at the output load.

Direct coupling of the two distributed delay-lines may cause problem of backward transmission of the reflected impulse from the second delay-line to the first delay-line, which makes large multiple reflections and eventually causes large ringing on the output signal. A backward decoupling circuit is therefore needed between the two delay-lines to reduce the backward coupling effect. This decoupling circuit included in Fig. 3.5, consisting of a capacitor, resistor and Schottky diode, facilitates direct coupling of the incident pulse from the first delay-line into the second one. It also functions as a pulse-clamping circuit. Fig. 3.6(a) shows a simplified circuit diagram used for the design of the decoupling circuit, which includes the decoupling circuit, a source for the incident pulse, a delay-line, an output transmission line and a load. The incident impulse is clamped to a certain DC level as shown in Fig. 3.6(b) and then combined with the reflected impulse from the delay-line to make a composite signal of monocycle waveform. Part of the reflected signal, represented by region A in Fig. 3.6(b), propagates to the input port of the decoupling circuit in the backward direction. In order to reduce the ringing on the composite monocycle pulse, region A should be reduced. However, excessive reduction of this region may sacrifice pulse-amplitude enhancement. Compromise between the ringing level and pulse amplitude is therefore needed in the design.

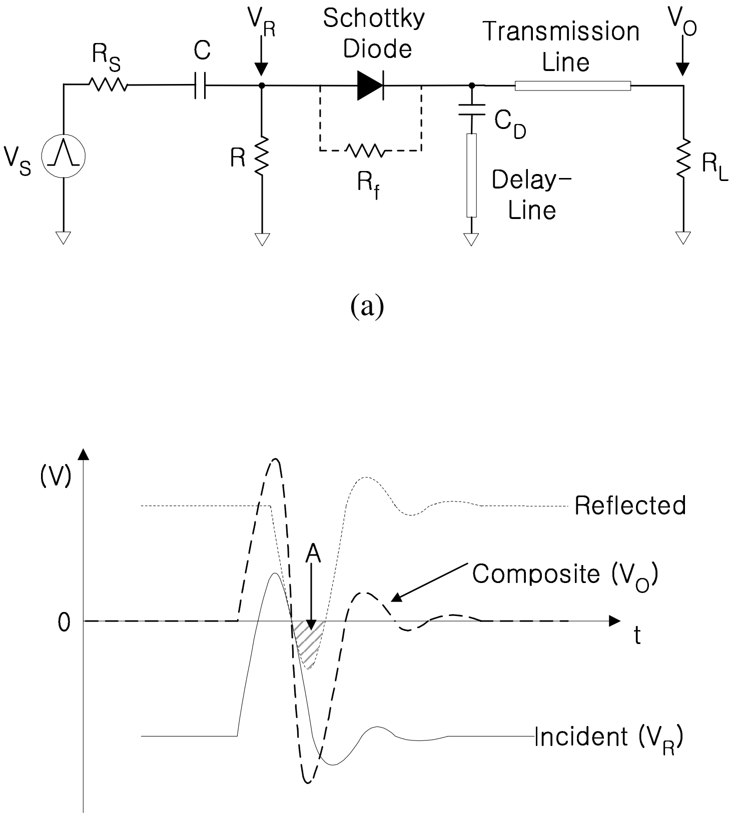

(a)

(b)

Fig. 3.6. (a) Circuit diagram used for the decoupling-circuit design. (b) Portions of the voltage waveforms involved in the composition of the monocycle.

Design of the backward decoupling circuit can be performed based on the well-known pulse-clamping circuit theory [24]. Assuming the input pulse is rectangular with 200-ps pulse duration and 12.5-MHz PRF, it's straightforward to draw the clamped output pulse as shown in Fig. 3.7. In Fig. 3.7, A_f and A_r represent the areas under the positive and negative voltages, respectively, and are related by the following relationship:

$$\frac{A_f}{A_r} = \frac{R_f}{R} \tag{3.12}$$

where R_f is the forward-diode resistance, which can be approximated by the series resistance of the Schottky diode, and R is the clamping resistance shown in Fig. 3.6(a). In our design, the pulse duration is relatively small compared to the period, resulting in a low duty cycle for the pulse generator. As implied in (3.12), for a low duty-cycle pulse signal, it is not practical to clamp the peak of the pulse to a small positive level close to zero. Therefore, assuming that R_f=10 Ω and the clamping level V_m is just a quarter of the pulse amplitude V_p as shown in the ideal pulse waveform in Fig. 3.7, the required R=10 KΩ can be calculated using (3.12). The actual steady-state output pulse waveform of the clamping circuit has some distortion as shown in Fig. 3.7. The distortion parameter Δf has the following relationship with Δr [24]:

$$\Delta f = \frac{R_f}{R_f + R_s} \frac{R + R_s}{R} \Delta r \tag{3.13}$$

where R_s is the source resistance. In our case, R_s=0, resulting in Δf=Δr. Therefore, as shown in Fig. 3.7, in order to increase Δf, τ_2=RC, and hence C, should be decreased. Larger Δf produces larger amplitude for the monocycle pulse but also generates more ringing signal because of the increased portion of the backward coupling. As a compromise to achieving this contradictory objective, it is deemed reasonable to choose

T_2, defined in Fig. 3.7, as RC or RC/2, from which C=8~16 pF can be obtained as design values. To achieve small ringing signal, C=15 pF is finally used in our design.

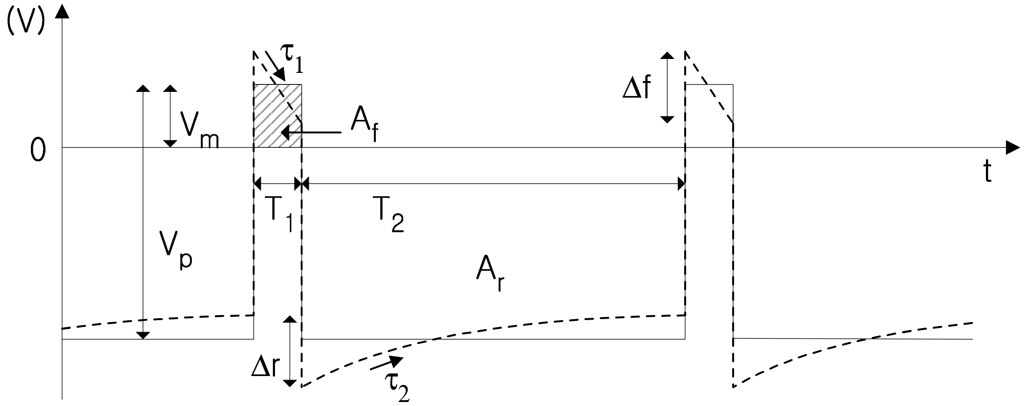

Fig. 3.7. Clamped impulse signal by the decoupling circuit with the circuit design parameters. The solid- and dashed-line waveforms represent ideal rectangular and actual distorted pulses, respectively.

C. Fabrication and Measurement

The delay-line SRD impulse generator was designed and fabricated first, based on the circuit diagram of Fig. 3.1, in order to verify the design concept. This designed impulse generator can be used for other applications such as TDR (Time-Domain Reflectometry) applications as well. The circuit was implemented as an MIC using the microstrip structure on an RT/duriod 6010 substrate having a relative dielectric constant of 10.2 and a thickness of 0.127 cm. For the convenience of measurement, the clock driving circuit was fabricated on a separate circuit board. The clock oscillator used is the low-cost voltage controlled crystal oscillator, CSX-750VC manufactured by Citizen, which has

12 MHz PRF, 5 V CMOS logic output, and 5 ns rise and fall time. The opamp used in the clock driving circuit is THS3001 manufactured by Texas Instruments Inc., which has 420-MHz unity-gain bandwidth and 100-mA output driving capacity. The buffer is BUF634 manufactured by Burr-Brown Co., which has 180-MHz bandwidth and ±250-mA output current capacity. In the SRD coupling circuit, R=12 Ω, which is the same as the design value, and C=300 pF, which is chosen as an optimal value through some experiments rather than using 200-pF design value. For the impulse shaping circuit, the SRD is SMMD-840, manufactured by Metelics Co., which has 70-ps transition time, 10-ns MCLT and 15 V of breakdown voltage. The delay-line is designed to have 100-ps round-trip time. The output pulse from the fabricated circuit is measured by an HP54750A digitizing oscilloscope with 12.4 GHz bandwidth, and the waveform is shown in Fig. 3.8. The measured impulse has 8-V peak amplitude, 160-ps FWHM (Full Width Half Maximum), and 300-ps pulse width (defined at 10 % of the peak amplitude). The bias voltages used for the designed impulse and tunable monocycle pulse generators are summarized in Table 3.1.

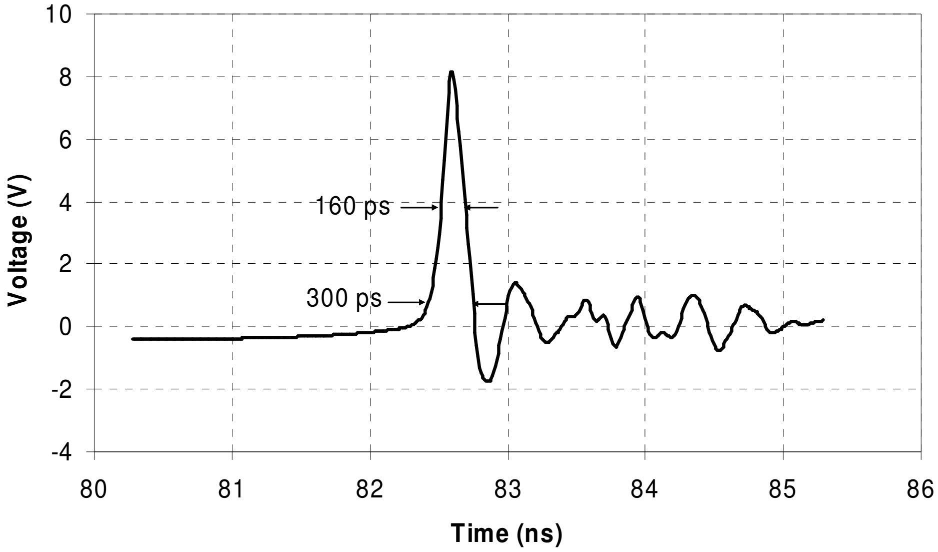

Fig. 3.8. Measured pulse signal output of the fabricated impulse generator.

Table 3.1. DC bias voltages (in V) for the designed impulse and tunable monocycle pulse generators.

	Clock Osc. V_{DD}	**Opamp**		**Buffer**		**PIN Diode**
		V_{cc}^{+}	**V_{cc}^{-}**	**V_{cc}^{+}**	**V_{cc}^{-}**	
Impulse Generator	5	16	-5	18	-18	N/A
Monocycle Generator	4.5 to 4.6	20	-5	18	-18	5

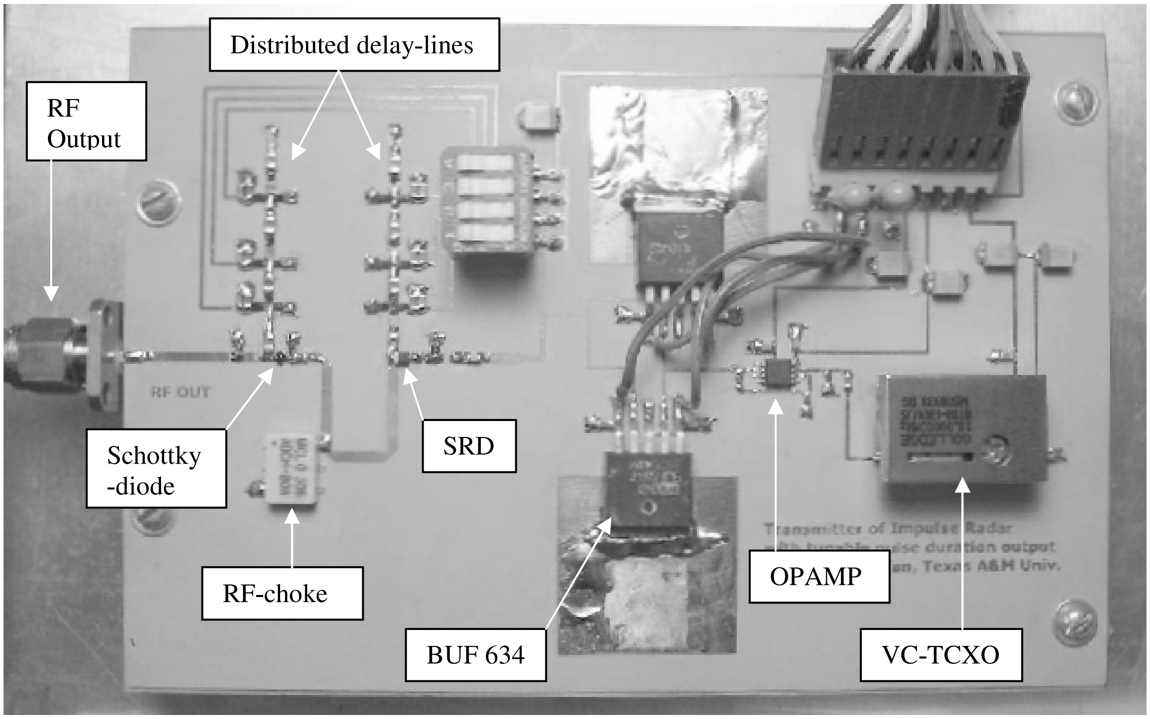

Fig. 3.9. Photograph of the fabricated transmitter of the impulse radar.

The tunable monocycle pulse generator as the transmitter of the impulse radar is fabricated in the form of a single MIC using microstrip structure on the same substrate as that used for the impulse generator. Its photograph is shown in Fig. 3.9.

The clock oscillator used in this circuit is the low-cost VC-TCXO (Voltage Controlled – Temperature Controlled Crystal Oscillator) GTXO-536V manufactured by Golledge Electronics, which has 10 MHz PRF, 5V HCMOS logic output, frequency (or PRF) adjustment through the voltage control, and additionally a mechanical trimmer. The reason why the VC-TCXO was used, which is related to the synchronous sampling receiver system of the impulse radar, will be explained in detail as part of the receiver design in Chapter IV.

For the SRD coupling circuit, C=1 nF is chosen as an optimal value through some experiments rather than 300 pF, as used in the impulse generator. This change may be considered as a result of a slight difference in the circuit structure in the pulse shaping circuitry as compared with the impulse generator. The same SRD for impulse generator is also used here. The switching PIN diodes used for this design are SMP1320-079 manufactured by Alpha Ind. The DC block capacitors for the decoupling of the PIN diode bias are C08 series 20-GHz DC block manufactured by Dielectric Laboratories Inc. The Schottky diode used for the backward decoupling circuit is MSS50048-E25 manufactured by Metelics. The required DC bias voltage settings for the designed transmitter is shown in Table 3.1.

The designed tunable monocycle pulse generator employs two identical distributed delay-lines, each divided into four sections to generate four different monocycle pulse durations. By turning on a branch of DIP switches, the corresponding two PIN-diode pairs located on the two distributed delay-lines are turned on simultaneously, generating an output monocycle pulse with a particular duration. The pulse duration, corresponding to the delay-line length, can be varied according to the selected turn-on position of the PIN-diode pairs. Table 3.2 shows the design parameters and results obtained for the tunable monocycle pulse generator. In the DIP switch setting, “1” represents connection of the corresponding branch of the switch and "0" represents disconnection. The designed pulse width, T_p, in Table 3.2 represents the desired pulse width of the output monocycle, which can be calculated approximately as $T_p=2T_{rt}+t_r$, where T_{rt} is the designed round-trip time and t_r is the rise-time of the leading edge of the monocycle pulse, which can be estimated as 170-ps through the impulse output of Fig. 3.8.

Table 3.2. Summary of the design parameters for the distributed delay-lines and the measured performance of the tunable monocycle pulse generator.

DIP S/W Setting	**Delay-Line Length (mil)**	**Designed Round-Trip Time (ps)**	**Designed Pulse Width (ps)**	**Measured Pulse Width@10% (ps)**	**Operating Frequency Band (GHz)**	**Pulse Amplitude (Vpp)**
001	220	120	410	450	0.40 to 3.70	5.8
010	400	200	570	600	0.30 to 2.60	8.8
100	700	350	870	880	0.20 to 1.80	9.8
000	1000	500	1170	1170	0.15 to 1.30	9.4

Fig. 3.10 shows the measured output monocycle pulses with four different pulse durations. The characteristics of each generated pulse are summarized in Table 3.2 along with the designed values for comparison. The measured pulse width at 10% in Table II is the pulse width measured at about 10 % level of the peak amplitude. Spectrum analysis has also been done for the generated monocycle pulse signals to determine their frequency bandwidths.

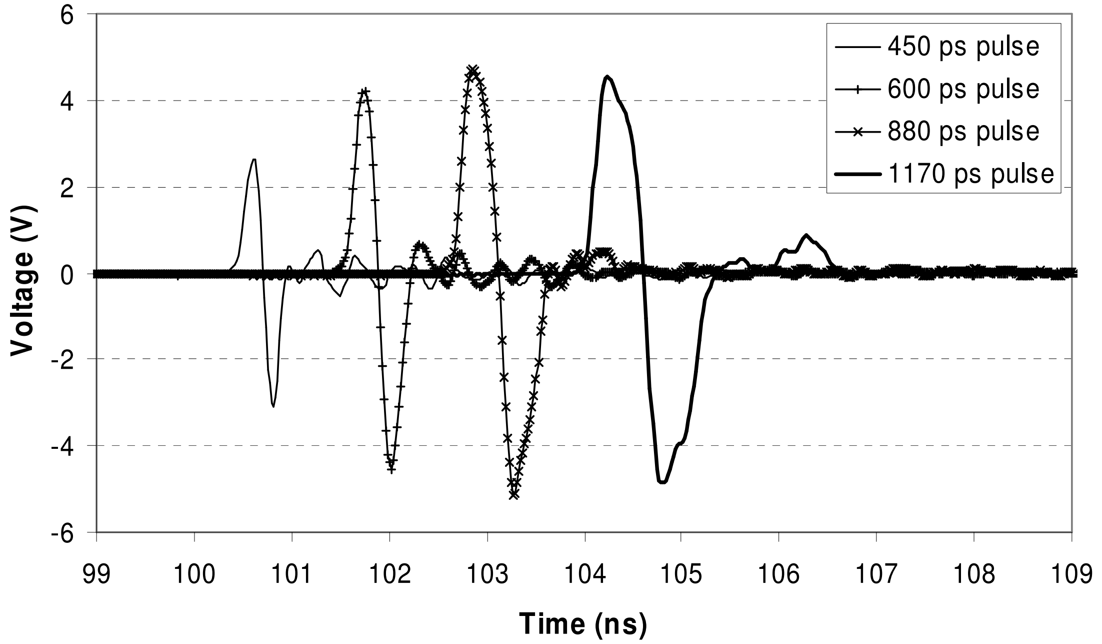

Fig. 3.10. Measured output monocycle pulses with four different pulse durations controlled by PIN diode switching.

Fig. 3.11 shows the frequency-spectrum data for the ideal 450-ps-duration monocycle pulse and the measured 450-ps-duration monocycle for comparison. The ideal monocycle is represented as a perfect single cycle of sinusoid. In the figure, we can see that the side-lobes and even the main-lobe of the ideal monocycle pulse is higher than those of the measured actual pulse. The reason is that the ideal pulse has abrupt transitions at the beginning and ending part of the single cycle duration. The available bandwidth (BW) is defined in Fig. 3.11 as the instantaneous bandwidth at 10-dB level, which is known to be a useful measurement to characterize the range resolution of impulse radars [12], [13].

For instance, the 400-ps-duration monocycle pulse has about 4 GHz of available BW, which corresponds to the range resolution of 1 in for pavement medium structure. The impulse radar having more than 3 GHz available BW for the transmitting pulse signal is usually known as a high resolution SPR, which can be used for high resolution applications such as land-mine or UXO detection. Available BW data is also useful from a system design aspect. The transmitting and receiving antennas should be designed to cover the available BW of the transmitting signal in terms of antenna input return loss and antenna gain. The receiver operating BW should also be large enough to cover the available BW of the pulse to minimize conversion loss and distortion of the down-converted signal.

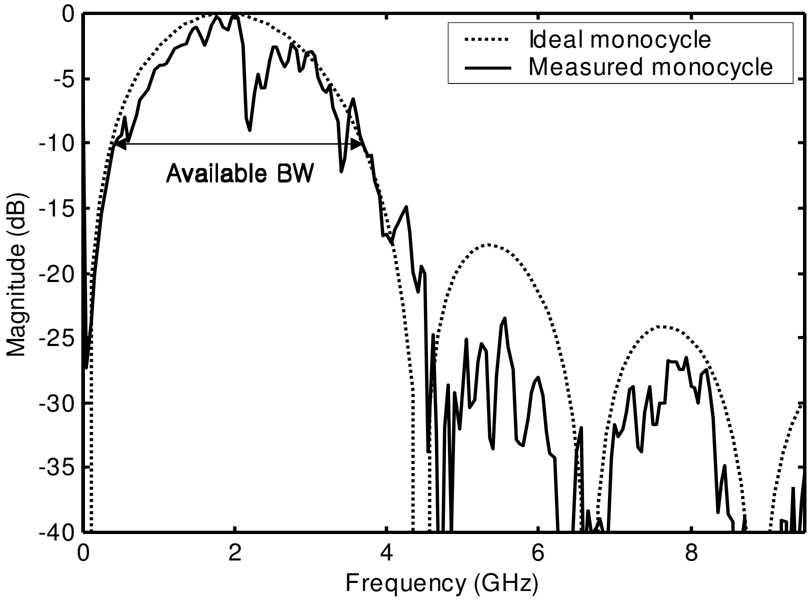

Fig. 3.11. Spectrums of the ideal and the measured monocycle pulse with 450-ps duration.

Spectrum analysis results for all the four generated monocycle pulses are shown in Fig. 3.12 and the measured operating frequency bands at 10-dB level are specified in Table 3.2. The operating frequency bands of these generated pulses are in the range of 0.15 to 3.7 GHz. Measured pulse amplitudes are in the range of 6 ~ 9 Vpp as seen in Fig. 3.10, which corresponds to 200 ~ 400 mW of pulse peak-power. The smaller amplitude obtained for the 450-ps pulse is due to the fact that the designed round-trip time of 120 ps along the delay-line is smaller than the actual transition time of 170 ps; therefore the incident step pulse could not reach the peak value before the arrival of the reflected one, resulting in reduction in impulse amplitude. The only way to improve the amplitude for the 450-ps pulse is to use a new SRD with faster transition time, acceptable MCLT, and breakdown voltage. Such a device, however, is not commercially available at present.

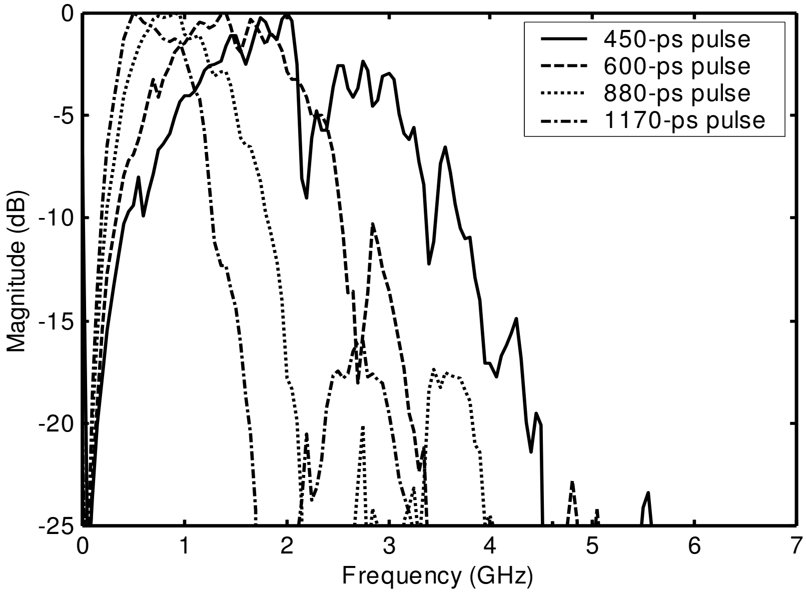

Fig. 3.12. Spectrums of all monocycle pulses generated from the designed tunable pulse generator.

D. Summary

A novel tunable monocycle pulse generator has been developed for low-power, short-range UWB applications. It is made up of a clock driving circuit, a SRD coupling circuit, a backward decoupling circuit and two distributed delay-lines. The clock driving and SRD coupling circuits improve the output power and transition speed. Using opamp and buffer IC's for the clock driving circuit has greatly simplified the circuit design. In the SRD coupling circuit, a simple RC filter structure is used to achieve near optimal bias condition for the SRD without external, complicated bias control circuit. A novel backward decoupling circuit is designed to reduce ringing in the output monocycle pulse. Tuning of the output monocycle pulse duration is achieved by alternately switching on and off the PIN-diode pairs spatially located along the delay lines. The employed tuning method is easy to implement and results in a compact circuit structure. The developed tunable monocycle pulse generator achieves varying pulse duration from 0.4-1.2 ns, corresponding approximately to the operating frequency range of 0.15-3.7 GHz, and 200-400 mW of peak power. These results show that the designed monocycle generator with advanced tuning capability can be used for most short-range UWB applications, even for high-resolution radar applications such as UXO and land-mine detection. The impulse generator, developed along with the tunable monocycle pulse generator, exhibits a performance of 160-ps FWHM and 8-V peak amplitude and can also be used for UWB systems.

CHAPTER IV

RECEIVER DESIGN

The receiver of the impulse radar is a system component that takes a UWB pulse signal as an input from the receiving antenna and down-converts the input to the baseband signal. The challenging problems in the design of the impulse radar receiver are down-converting such a wideband input signal and retaining the down-converted signal waveform in the same form as the RF input signal. It is common to use a synchronous sampling (or equivalent-time sampling) receiver structure in the impulse radar system, unlike other CW radars or communication systems [2], [3], [48]-[51]. The other receiver structure for impulse radars such as channelized ADC (Analog-to-Digital Conversion) receiver has been reported recently [5]; but the synchronous sampling method is much simpler and provides more compact system structure. Instead of designing the receiver component, the wideband sampling oscilloscope commercially available can also be used as a receiver, but it is bulky, expensive and not suitable for mobile and low-cost systems.

The synchronous sampling method has been widely used in electro-optic sampling techniques to down-convert RF signal or to reproduce fast transient signal on a large time scale [49], [50]. Fig. 4.1 illustrates the basic principle of the synchronous sampling method. Synchronous sampling in time domain is basically the same as the harmonic mixing of two different frequencies in frequency domain. In Fig. 2.1, V_R is the waveform of the input RF signal and V_O is the LO strobe pulse signal that triggers the sampling. V_D is the output down-converted signal through the ideal sample-and-hold operation of the receiver circuit.

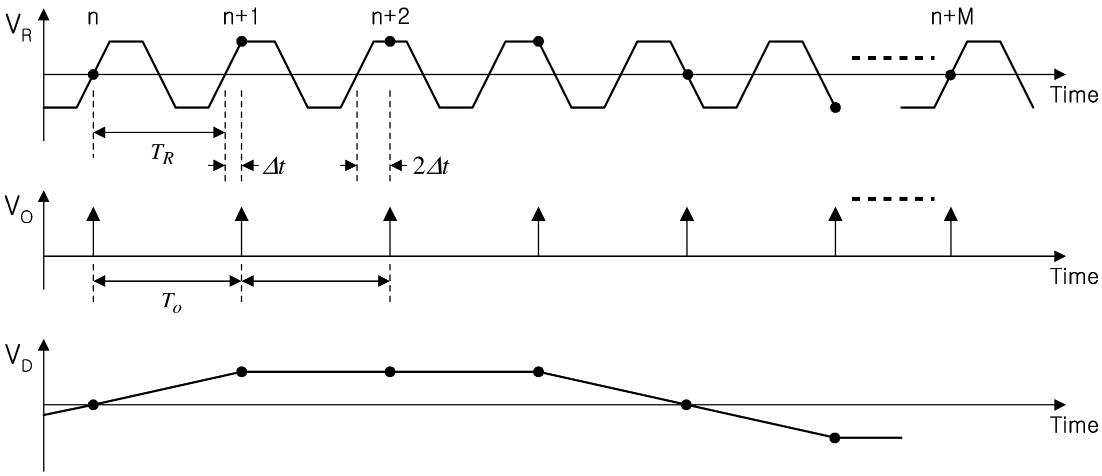

Fig. 4.1. Illustration for the principle of synchronous sampling down-conversion.

Note that to achieve down-conversion of the RF input V_R, the frequency of V_R and PRF of V_O should have a small difference between them. In the case of the impulse radar system, the RF input V_R is actually a pulse signal having a PRF, f_R, and an extremely large duty cycle. For down-converting or stretching the RF pulse, PRF of the LO strobe pulse, f_o, should have a small deviation from f_R; therefore, the synchronous sampling receiver of the impulse radar should have two stable reference oscillators with a small frequency deviation between them. One oscillator is used in the transmitter and determines the PRF of the transmitting pulse, which turns out to be the PRF of the RF input pulse of the receiver. The other oscillator is used for the LO strobe pulse generator of the receiver to determine the PRF of the strobe pulse.

There is another method for building the synchronous sampling receiver other than using two reference oscillators with different frequencies. Two identical oscillators with the same frequencies can be used if proper timing of the sampling can be provided by a timing control circuit. In Fig. 4.1, the dots on the V_R waveform represent the sampled points numbered from n to n+M. Notice that each pair of two successive sample points have the same time delay of Δt from the RF input signal period T_s. Therefore, even in the situation that the PRF of the strobe pulse is the same as that of the RF input pulse, if a constant time delay Δt occurs for the next period of the signal, correct timing of the sampling can be achieved. The successive time delay generation can be implemented by using the digital delay generator, which is a digital IC commonly used in the timing control of digital circuits.

The synchronous sampling using the delay generator can be implemented at low cost, whereas the receiver circuit structure is more complicated than that consisting of using two frequency deviated oscillators. Other disadvantages of using a delay generator are that minimum delay time realizable is limited to 10 ps with currently available commercial products and the number of sample points of a down-converted signal during a time interval of a single clock period is also limited by the internal code length (usually 8-bit) of the delay generator.

To implement the receiver with more compact circuit structure and avoid the limitations of the delay generator, I have finally chosen the synchronous sampling method of using two frequency deviated oscillators for our receiver design. Fig. 4.2 shows the designed receiver system architecture for our impulse radar system. In Fig. 4.2, the synchronous sampling is implemented by using two reference clock oscillators; one is in the transmitter, and the other in the receiver, with a frequency deviation of Δf between them. As indicated in Fig. 4.2, the receiver is composed of an LNA (Low Noise Amplifier) and an integrated sampling mixer circuit in general.

The LNA is only required if the received signal from the receiving antenna is too weak to be detectable or triggered in the baseband circuit. In some applications, the designed transmitter does not need to supply maximum peak power, so much smaller peak power can be used in a low power mode in the transmitter to save DC power consumption in the system. Using the designed transmitter in low power mode or another commercially available low-power transmitter, the LNA may be a useful device to amplify a weak received signal. However, using the designed transmitter in full power mode, the received signal is so large that there is no need to use the LNA to trigger or detect the received signal in baseband circuit. Using the LNA in full power mode of the transmitter

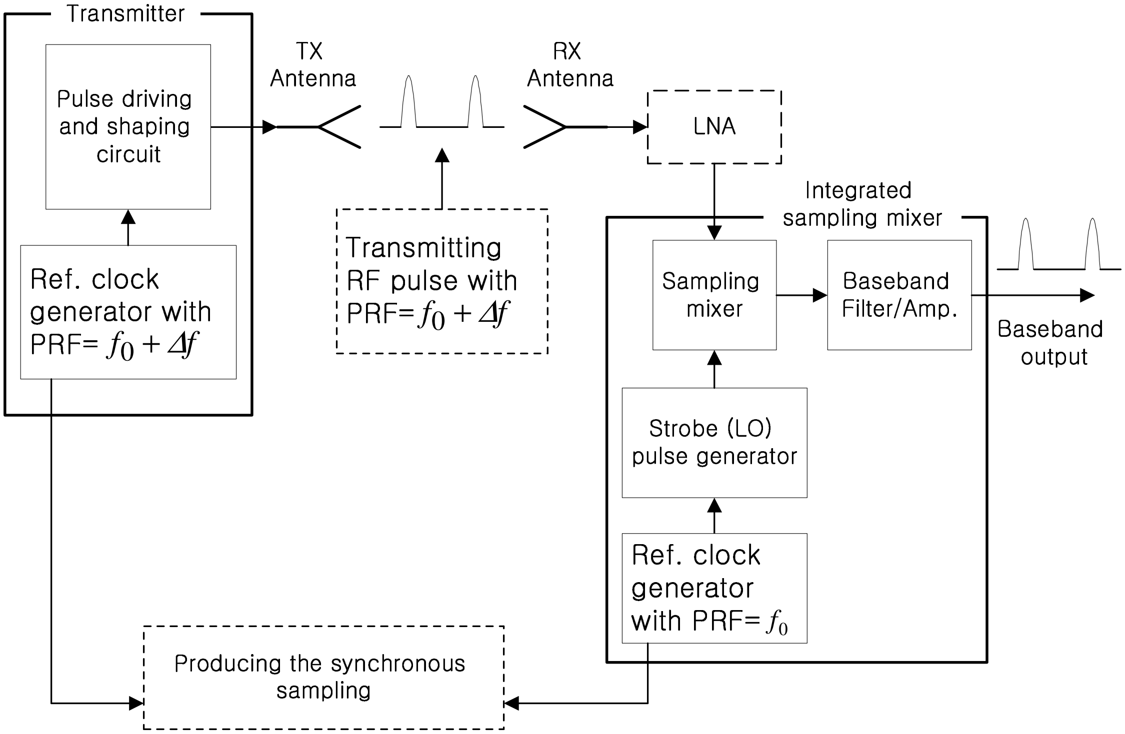

Fig. 4.2. Block diagram of the designed synchronous sampling receiver system for the impulse radar sensor.

creates a problem such as saturation of the concatenated sampling mixer through the excessively large output of the LNA, and makes distortion in the down-converted signal. This fact was found in experiments on the designed overall impulse radar system. Since the final designed system is supposed to operate in full power mode for the pavement assessment, the LNA is not included in the final system. Details of the UWB LNA design for the UWB input pulse signal are described in the last section of this chapter as a reference for other system designs or applications.

Without the LNA, the receiver of the impulse radar system is only the integrated sampling mixer itself. All of the required components for down-conversion of the RF input pulse are the sampling mixer (or sampler), the strobe pulse generator, the reference clock oscillator, and the baseband filter and amplifier, which compose the integrated sampling mixer as shown in Fig. 4.2. The integrated sampling mixer is so named since these required components are integrated in a single PCB (Printed Circuit Board) as a hybrid MIC.

The sampling mixer, the key component of the integrated sampling mixer, has been widely used for wideband frequency down-conversion in many applications. One application is for microwave instrumentation such as network analyzers, frequency counters, and digitizing oscilloscopes [52]-[66]. In this application, the sampling mixer is used for synchronous sampling (or sub-sampling) of a fast transient signal to recover it on a large time scale or for down-conversion of a continuous-wave signal. Solid-state millimeter-wave and electro-optic samplers, which are able to sub-sample picosecond transient signals, have been developed for instruments operating in the millimeter-wave band [55]-[65]. Another important application of the sampling mixer is for UWB impulse radars and communication systems, which employ sub-nanosecond short pulse as the transmitting signal [3], [48], [67], [68]. Sampling mixers for UWB applications particularly require low conversion loss and high dynamic range because of its direct conversion operation in the receiver. Some analyses have also been reported for the sampler [69], [70].

Through this research, I have developed a new UWB sampling mixer integrated with a local strobe-pulse generator and a baseband filter and amplifier. A simple equation allowing accurate prediction of the sampler's intrinsic conversion loss and RF operating bandwidth is derived. Development of the strobe pulse generators operating at such a low clock frequency as 10 MHz is also presented along with the design information for circuit components. The developed sampling mixer is called Coupled-Slotline-Hybrid (CSH) sampler stemming from its use of a CSH. Double-sided planar structure is used for low-cost fabrication and ease of integration with the strobe-pulse generator and the baseband circuit using hybrid MIC technique. The CSH sampler employs a modified version of the coupled-slotline magic-T [71] for the coupling and terminating of the RF and LO signals to the sampling-bridge circuit. The modified CSH allows the sampling bridge to be included and suppression of the ringing of the strobe pulse signal to be achieved. The developed CSH sampler achieves a conversion loss of 4.5-7.5 dB (without amplifier) and conversion gain from 6.5-9.5 dB (with amplifier) over a 3-dB bandwidth of 5.5 GHz, which is, to our best knowledge, the best-reported conversion efficiency for a hybrid sampling mixer at this frequency range. The sampler has a dynamic range greater than 50 dB and a sensitivity of -47 dBm.

In the subsequent sections of this chapter, I will first discuss the design of the strobe pulse generator efficient for low clock driving frequencies. In section B, the design and performance of the novel CSH sampler circuit is described. In section C, design parameters pertaining to the synchronous sampling receiver system as well as the signal processing unit such as the required frequency deviation between two reference clock oscillators will be derived. Finally the design of the UWB LNA circuit and its performance will be described.

A. Design of the Strobe Pulse Generator

SRD (Step Recovery Diode) impulse generators have been used for generation of sub-nanosecond strobe pulses for samplers operating up to more than 10 GHz [57]-[59]. Design methods for SRD impulse generators are well developed and used for various multiplier and sampler designs [43]-[47]. These design methods, however, are applicable for high (input) driving-source or clock frequencies. They do not provide optimized and good performance when the driving-source frequency is as low as 10 MHz. Low driving frequency is needed for various applications. In UWB radar requiring sub-sampling in the receiver, the transmitted pulse's PRF is determined by the strobe pulse's PRF in the receiver, which may be as low as 10 MHz in order to have sufficient observation time and detection range.

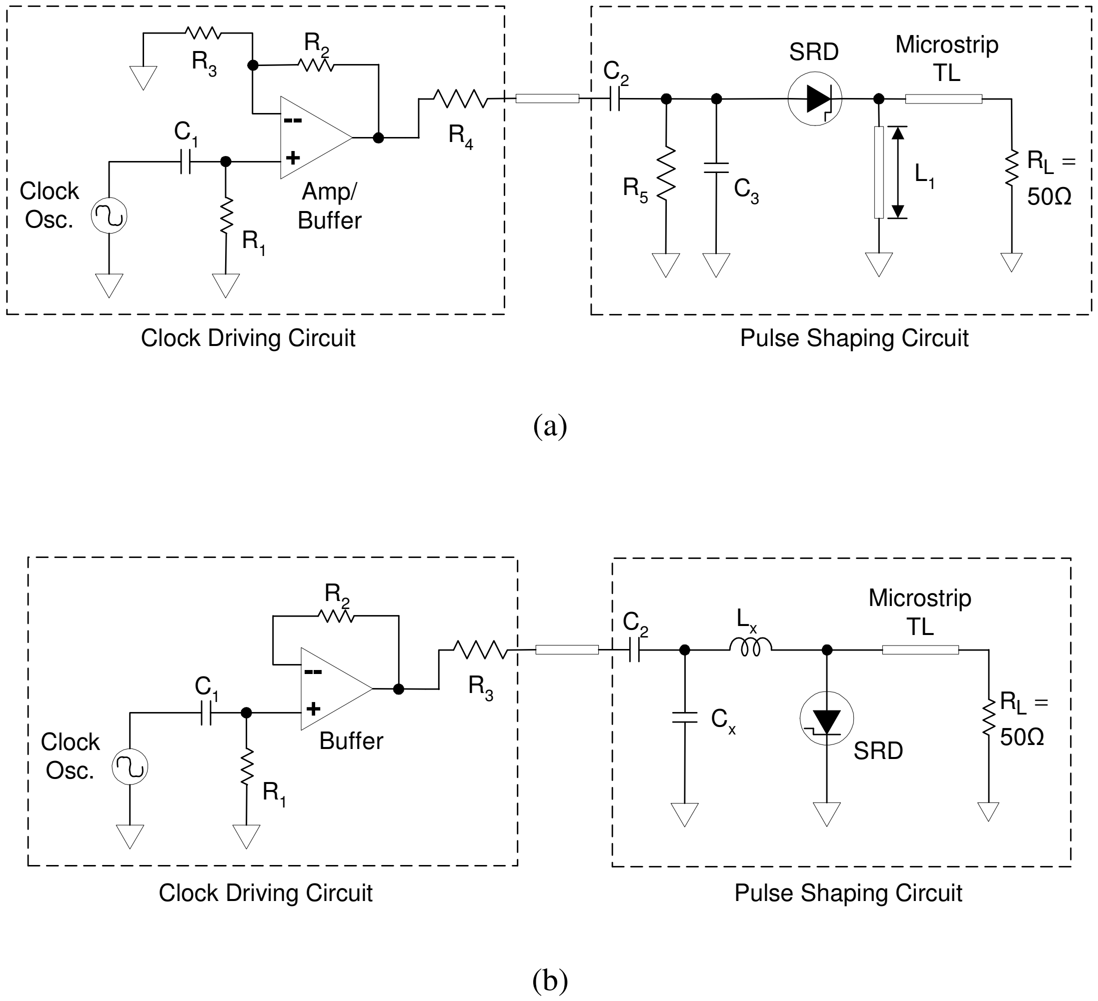

Fig. 4.3. Circuit diagrams for (a) the delay-line and (b) shunt-mode pulse generators.

In this work, modified SRD impulse generators have been developed for good performance at low driving frequency. Two different types of SRD impulse generators were designed based on well-known circuit configurations [39], [43]. One is the delay-line type and the other is the shunt-mode type. These two types were considered because the former can generate short pulse duration and the latter can produce high pulse power. Designed circuit diagrams, including the clock driving circuits, for these two different types are shown in Fig. 4.3. These pulse circuits were optimized to obtain high pulse power for low PRF with no external DC bias required for normal operation.

Since the shunt-mode pulse generator has better performance than its delay-line counterpart for sampler application and part of their designs is common, only the design of the shunt-mode pulse generator is described here. The measured performance of both types, however, will be presented.

In the shunt-mode pulse generator, as shown in Fig. 4.3(b), a clock oscillator is used as the driving source for the pulse shaping circuit. To obtain good output power efficiency and high pulse amplitude, the frequency of the driving source should be less than the minority carrier life-time of the SRD. In the case of 10-MHz driving source, SRD having at least 100-ns life-time must therefore be used. However, in reality, this kind of long life-time SRD can not have fast transition time. To alleviate this problem and satisfy both the conditions of life-time and transition time, a fast clock signal source, whose rise-time is comparable to the SRD's life-time, is used. A summarized specification of the selected clock oscillator and SRD for our design is shown in Table 4.1.

Table 4.1 Specification summary of the clock oscillator and SRD used in the pulse generator design.

Clock Oscillator	**rise-time**	Max. 5 ns
	PRF	12 MHz
	output voltage level	5 V
SRD	**minority carrier life-time**	10 ns
	turn-off transition time	70 ps

In Fig. 4.3(b), C_1 and R_1 are required for AC coupling of the source to the buffer. The buffer is used to provide a good impedance matching between the oscillator and pulse shaping circuit and to supply a sufficient current to the load. The buffer used is an opamp, which has a wide bandwidth larger than 150 MHz to maintain the fast rise-time of the input clock signal. It has a maximum output current level of 100 mA. The resistor R_3 is required to stabilize the circuit operation when the load of the buffer is in low impedance state. The pulse-shaping circuit is basically a shunt-mode SRD impulse generator [43]. C_2, SRD and R_L make up the pulse clamping circuit, which functions as a self-biasing network to provide proper bias required for the shunt-mode pulse generator. The driving inductance L_x was determined approximately for initial design value using the equations in [47], and 1 nH was chosen to include some design margin. The capacitor C_x is needed to form a RF short-circuit at the time of the diode turn-off so that L_x, C_d (depletion capacitance of SRD), and R_L form a parallel-resonant ringing circuit required for generation of the impulse. Therefore, C_x should be large enough compared to C_d such that it has a low impedance value over the pulse frequency band. But the combination of C_x and the equivalent resistance of R_3 and R_L results in a low-pass filter for the input driving signal so that C_x may not exceed some certain value to prevent the input clock signal from slewing. Therefore, $C_x < t_r/(2.2\ R_e)$, where t_r is the rise-time of the clock signal and $R_e=R_3||R_L$. In the case of $t_r=2.5$ ns, C_x is found to be less than 113 pF. Experiment with the fabricated circuit shows that C_x from 50 to 100 pF can be used.

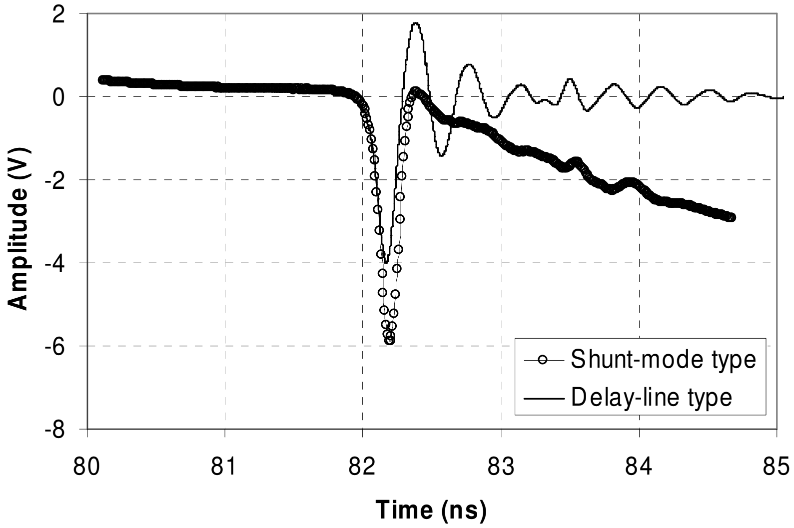

Fig. 4.4. Measured output pulse waveforms of the delay-line and shunt-mode pulse generators.

Fig. 4.4 shows the measured output impulse waveform from the fabricated circuits for the delay-line and shunt-mode types. These waveforms were measured by a digitizing oscilloscope, whose bandwidth is 12 GHz. FWHM (Full Width Half Maximum)'s of the generated pulses are about 150 ps. The pulse waveform of the delay-line pulse generator has large ringing even though the pulse duration is shorter than that of the shunt-mode pulse generator. Large ringing can cause some distortion on the down-converted output of the sampler. Its amplitude is also smaller than that of the shunt-mode type while the slew-rates of both pulses are the same. For pulses of same slew-rate, the actual sampling aperture times, which determine the bandwidth of the sampler, will be almost the same because of the clamping effect of the sampling-bridge circuit. The clamping circuit structure of the sampling bridge and the relationship between the sampling aperture time and bandwidth of the sampler will be shown in section B. Furthermore, for the same slew-rate pulses, a higher amplitude pulse improves the conversion loss and increases the 1-dB compression point of the sampler. Therefore, the shunt-mode type pulse generator is a better choice for sampler in all aspects.

B. CSH (Coupled-Slotline-Hybrid) Sampler

1) Design of the CSH sampler

The developed CSH sampling circuit is a two-diode-bridge configuration. Its equivalent circuit diagram, including the baseband buffer/amplifier circuit, is shown in Fig. 4.5 [72]. The equivalent circuit follows the split-ground configuration proposed by Grove [52] for reducing the parasitic inductance of the signal transmission line.

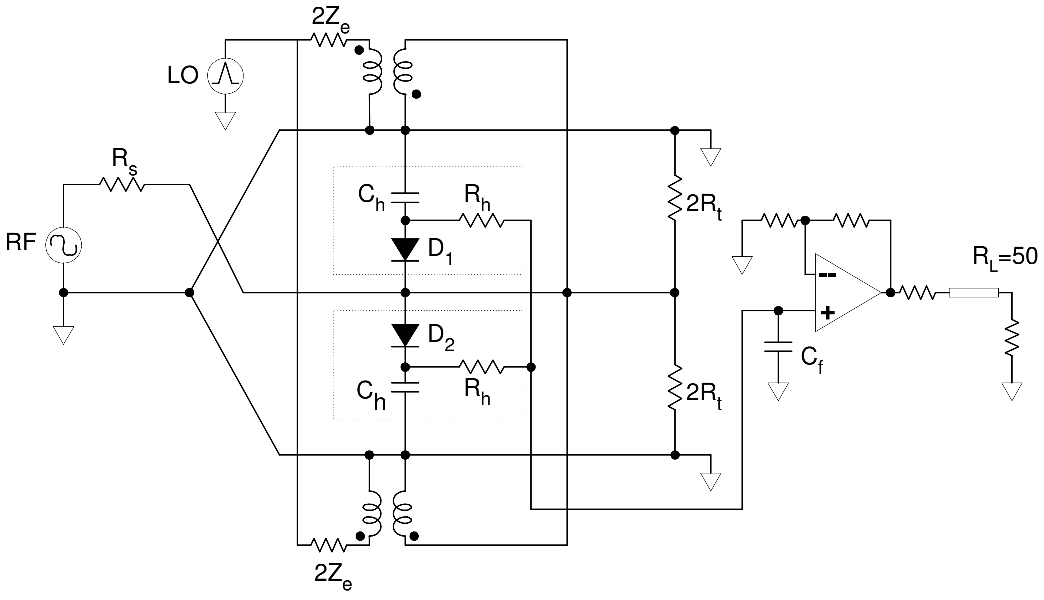

Fig. 4.5. Equivalent circuit diagram of the CSH sampler.

Each part of the sampling bridge, consisting of a Schottky sampling diode (D_1 or D_2), a holding capacitor (C_h) and a holding resistor (R_h), forms a pulse-clamping circuit. The clamping circuit acts as a self-biasing network so that no external bias network is required. In the sampling circuit, C_h also works as a coupling capacitor for the LO pulse. Its capacitance should thus be sufficiently large as compared to the junction capacitance of the sampling diode in order to increase the forward bias current and decrease the diode's junction resistance, resulting in a decrease of the charging time constant of the RF signal and eventually improving the conversion loss of the sampling mixer. In another point of view, when the sampling diode is turned-off, a large holding capacitance would reduce loss of the sampled RF voltage, effectively improving the conversion loss. On the contrary, small capacitance of C_h is desirable to facilitate good

RF input matching over a wide frequency range. With the junction capacitance of the beam-lead Schottky diodes used in our design of about 0.1 pF, proper values of C_h were estimated from 0.2 to 0.5 pF. Through circuit simulations of the designed sampler using ADS [73], a value of 0.2 pF was finally chosen for C_h to accomplish a wide bandwidth for the sampler.

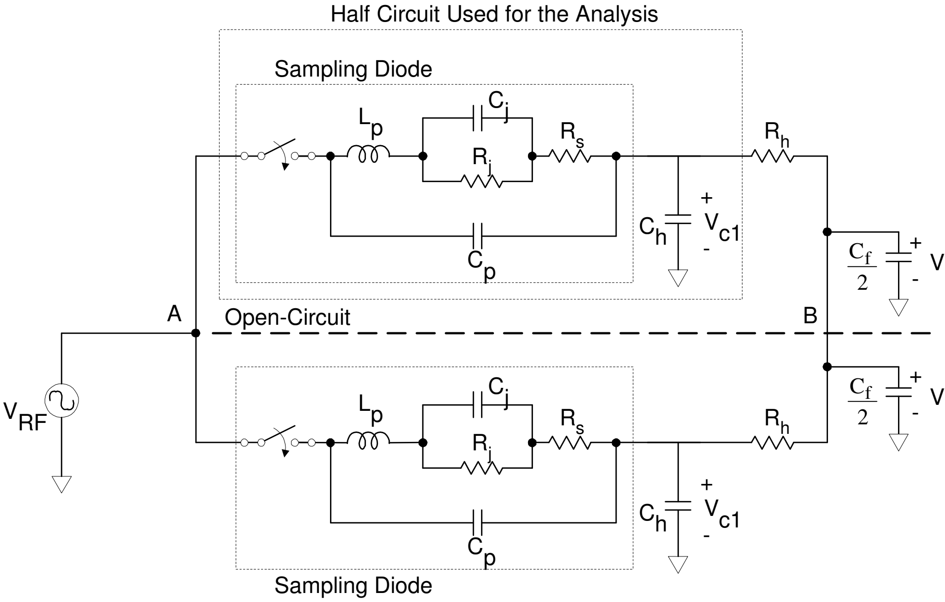

Fig. 4.6. Equivalent-circuit model of the two-diode-bridge sampler, including the baseband filter, with respect to the RF signal sampling (i.e., during the time the RF signal is sampled).

The two-diode-bridge sampling circuit is analyzed quantitatively using an equivalent circuit model shown in Fig. 4.6 to obtain analytical result for the intrinsic conversion loss and, hence, the frequency response of the sampler. As indicated in Fig. 4.6, the dashed line connected through the nodes A and B represents an open-circuit considered in the analysis. Assuming identical sampling diodes and holding capacitors, the sampled voltages V_{c1} and V_{c2} are equal. The resultant sampled voltage, V_c, through the baseband filter is equal to V_{c1} and V_{c2} because of the resistive divider form of the voltage combining structure. Therefore, only a half of the overall equivalent circuit model (without the baseband filter structure) may be considered for the analysis. The Schottky sampling diode is represented in Fig. 4.6 as a combination of a switch and diode's turn-on equivalent circuit model. L_p and C_p represent the diode's package parasitics. The switch can be modeled as a RC low-pass filter. The cut-off frequency of the switch is determined by the effective sampling time represented as

$$T_s = \sqrt{t_r^2 + t_a^2} \tag{4.1}$$

where t_r denotes the rise-time of the RF signal charging through the diode and t_a represents the sampling aperture time [61], [64]. In good sampling diodes, the junction capacitance is normally so small that t_r can be ignored. Using this model of the switch and a half of the equivalent circuit model in Fig. 4.6 without the baseband filter, the following equation can be derived:

$$\left|\frac{V_{c1}}{V_{RF}}\right| = \frac{1}{\sqrt{1+\left(\frac{\omega T_s}{2.2}\right)^2}}\sqrt{\frac{1+\left(\omega R_j C_j\right)^2}{\left(1-\omega^2 R_s C_h R_j C_j\right)^2+\left\{\omega\left[R_s C_h + R_j\left(C_h + C_j\right)\right]\right\}^2}} \tag{4.2}$$

This equation calculates the intrinsic (sampling) conversion loss of the sampler due to two sampling diodes and holding capacitors. It represents a relative conversion loss normalized to the minimum conversion loss occurred at the lowest RF frequency. The minimum conversion is due mainly to the charged RF signal leakage during the signal charging and discharging phases through a low parasitic impedance formed by the inductive and capacitive parasitic of the holding resistor R_h and is a critical performance parameter of the sampler. Its measured value for the designed sampler is given in sub-section B.2. The usefulness of (4.2) lies in the fact that it can predict accurately the conversion loss behavior and RF operating bandwidth of the sampler, as will be seen in sub-section B.2.

The sampling aperture time is dependent on the strobe pulse width and the reverse bias applied to the sampling diodes. In the designed sampling-bridge circuit, a self bias occurs due to clamping effect, effectively producing reverse bias to the sampling diodes. From the ADS simulation of the circuit shown in Fig. 4.6 with actual diode model, the sampling aperture time was estimated as 60 ~ 70 ps. Using the diode parameter values provided by the manufacturer (Rj=16 Ω, Cj=0.1 pF, Rs=11 Ω) and the estimated aperture time of 60 ps, the intrinsic conversion loss of the sampler for C_h=0.2 pF was calculated using (4.2) and is shown in Fig. 4.11 (in sub-section B.2) together with the measurement result. From this analysis, the estimated RF bandwidth can be found approximately as 5.5 GHz, which is well coincided with the measurement result.

In Fig. 4.5, when the diode is turned-off, C_h, R_h and C_f compose a discharging path for the charged RF voltage in C_h, where R_h and C_f work as a low-pass filter for the baseband signal. This baseband filter is necessary to combine sampled voltages through sampling diodes and to reduce the output noise power. The required value for the holding resistor, R_h, was initially calculated as 80 KΩ by considering the strobe pulse PRF and the required time constant. However, the final value of R_h was selected as 30 KΩ to reduce the effect of its parasitic impedance on the conversion loss and to avoid an increase of the noise in the baseband signal, which is likely to occur with a large resistance. C_f was chosen as 7 pF in order to have a cutoff frequency of 1.5 MHz for the low-pass filter. R_t is a terminating resistance for both the RF and strobe pulse signals. An opamp is used as the baseband amplifier.

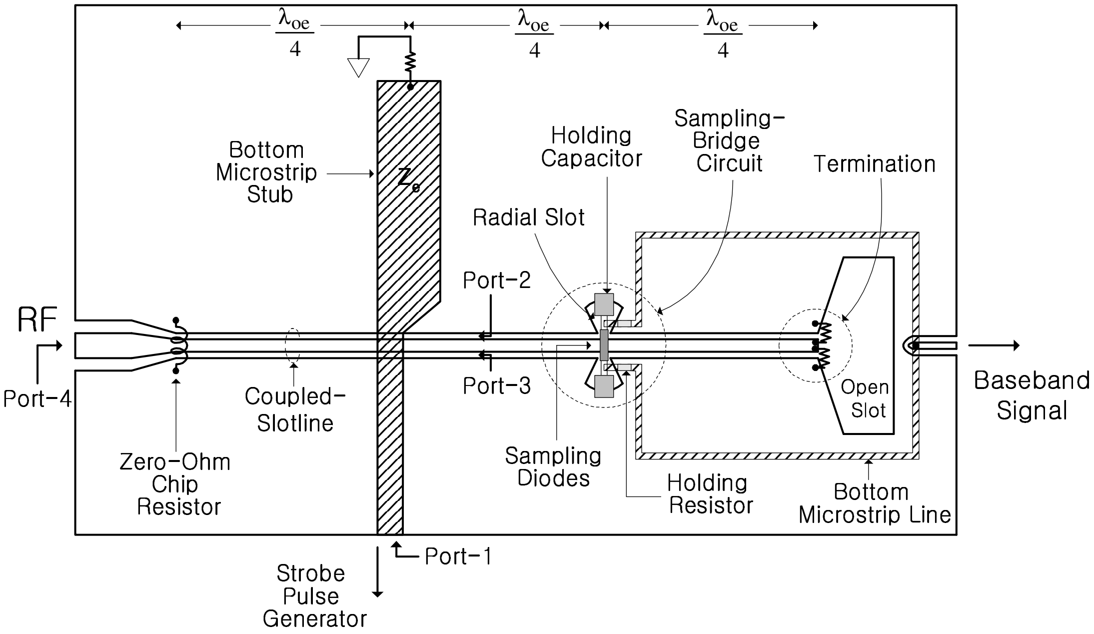

Fig. 4.7. Layout of the designed sampling circuit with main RF components. The strobe pulse generator and baseband circuits are not shown. The indicated port numbers are used for simulation purposes as shown in Fig. 4.8.

Fig. 4.7 shows a layout of the CSH sampler, including only such major components as the CSH, sampling-bridge circuit and connection to the baseband circuit. The basic configuration and design of the CSH follows the well-known coupled-slotline magic-T [71]. The LO pulse coupling is achieved through an underside microstrip line (rather than an air-bridge) because it facilitates resistive termination required for the strobe pulse generation, is easily fabricated by PCB manufacturing process, and provides more rigid, reproducible structure for hybrid MIC. The extended quarter-wavelength coupled-slotlines between the sampling bridge and terminations, and the open slot at the terminations help reduce the ringing in the strobe pulse. The two underside microstrip lines connecting to the sampling bridge facilitate integration with the baseband circuitry.

The even-mode (Z_{oe}) and odd-mode (Z_{oo}) characteristic impedances of the coupled-slotlines used in the CSH can be obtained, assuming no termination at the open end of bottom microstrip stub, as

$$\begin{aligned} Z_{oe} &= Z_o \\ Z_{oo} &= 2R_t = 2Z_o \end{aligned} \tag{4.3}$$

where Z_o is the characteristic impedance of the feeding CPW and microstrip line at the RF and LO ports, respectively. R_t is a half of the terminating resistor shown in Fig. 4.5. In Fig. 4.7, λ_{oe} is the even-mode wave-length at the center frequency. The center frequency is defined in our design as that of the composite monocycle pulse created by a concatenation of 2 opposite polarity impulses. Therefore $\lambda_{oe}/2$ is corresponding to the distance along which the strobe impulse propagates on the coupled-slotline during its duration. The CSH was implemented using Z_o=50 Ω, Z_{oe}=70 Ω and Z_{oo}=100 Ω. 70 Ω was used for Z_{oe}, instead of 50 Ω according to (4.3), in order to have reasonable transmission line dimensions and to accommodate the sampling bridge, using RT/duroid 6010 substrate having a relative dielectric constant of 10.2 and a thickness of 0.127 cm. The characteristic impedance, Z_e, of the bottom microstrip stub was determined as 25 Ω in order to attain wideband coupling of the LO pulse signal as indicated in the design of the coupled-slotline magic-T circuit. The microstrip stub is terminated with a resistor, which is needed for the sampler because the strobe pulse generator requires a resistive load for the driving clock source as well as for constructing a proper parallel tank circuit for impulse generation. Fig. 4.8 shows calculated results for the designed CSH with 50-Ω termination at the open end of the microstrip stub. Although the CSH was not measured, its operation is validated through good performance obtained for the sampler as will be seen later in sub-section B.2. The insertion loss result for the LO pulse signal in Fig. 4.8(a) shows a pass band from 1 to 5 GHz, which covers a significant portion of the frequency band of the pulse having 150 ps of FWHM. The return loss of the RF port and the isolation between the RF and LO ports displayed in Fig. 4.8(b) show good results up to 10 GHz. The transient simulation results in Fig. 4.8(c) show that the two splitted LO pulse signals (to the two sampling diodes) are well matched and 180-deg out-of-phase without significant ringing. It should be noted that the first large side-lobe signal with opposite polarity to main-lobe pulse, seen in Fig. 4.8(c), does not cause any adverse effect to the sampling, because it provides more reverse bias to the diode and effectively turns the diode off.

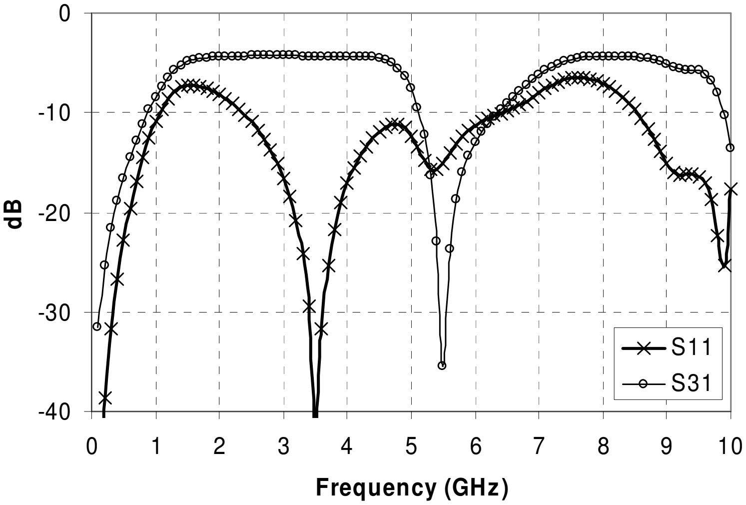

(a)

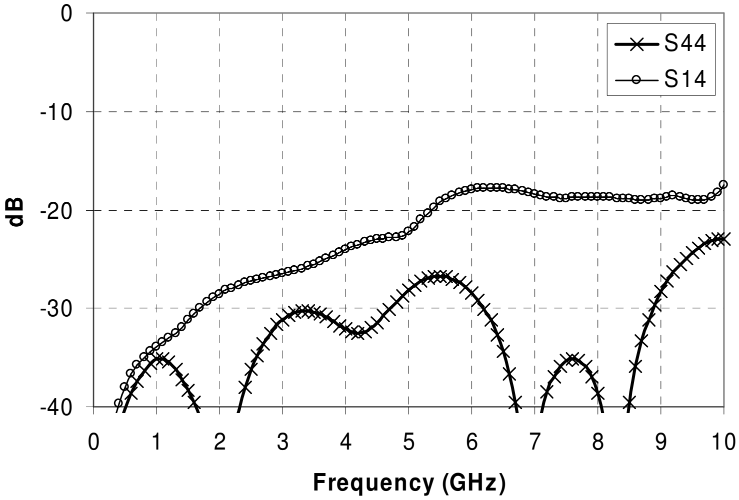

(b)

Fig. 4.8. Simulation results for the designed CSH using ADS. (a) S11: return loss at the LO-port, S31: insertion loss for the coupled LO pulse. (b) S44: return loss at the RF-port, S14: isolation between the RF- and LO-port. (c) Pulse waveforms at the coupled-slotline output ports 2 and 3. Reference port numbers are shown in Fig. 4.7.

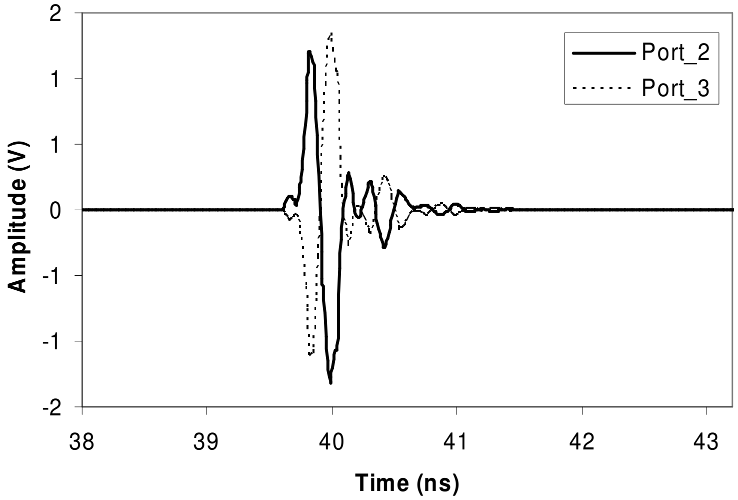

(c)

Fig. 4.8. Continued.

The layout configuration for the sampling-bridge circuit shown in Fig. 4.7 was also optimized using ADS to minimize the effect of the layout on the performance of the RF transmission. Two radial slots are used at the sampling bridge to reduce the parasitic capacitances. Connection to the baseband circuit is implemented using via-holes and two underside microstrip lines. Close contact of the holding resistor to the sampling diode-bridge provides good isolation between the RF signal line and baseband connection.

An additional quarter-wavelength coupled-slotlines is used between the sampling-bridge and termination resistors to reduce possible ringing of the LO pulse signal at the sampling bridge. Without this transmission line, a positive reflected pulse signal occurring at the termination would broaden the sampling aperture time, leading to degradation of the bandwidth of the sampler. The quarter-wavelength line causes the reflected pulse signal to be aligned 180-deg out of phase with respect to the side-lobe (ringing) of the incident pulse signal at the sampling bridge, resulting in a removal of the side-lobe of the pulse waveform. Effectively, the additional quarter-wavelength line provides better input matching at the sampling bridge for the LO pulse signal.

The use of CSH provides several advantages for the sampler. Firstly, by arranging the RF and LO ports on each side of the circuit, it is possible to make a good signal line termination taking advantage of the wide open slot. Secondly, the baseband connection can be implemented by the bottom microstrip lines, making easy integration with the baseband circuit. The designed sampling circuit does not require any wire connections or air-bridges, hence reducing fabrication efforts and enabling low-cost mass production of the circuit, especially for hybrid MICs. A zero-ohm chip resistor is used in the CSH's coupled-slotlines at the RF port to simulate an air-bridge needed for reflecting the LO pulse.

2) Fabrication and performance of the CSH sampler

The CSH sampling mixer was fabricated on RT/duroid 6010 substrate with a relative dielectric constant of 10.2, thickness of 0.127 cm and loss tangent of 0.0023. The clock driving circuit of Fig. 4.3(b) was fabricated on a separate substrate for the convenience of measurement. Fig. 4.9 shows the fabricated CSH sampling mixer assembled on a metal fixture without the clock driving circuit. The beam-lead Schottky-diode bridge used in the sampler is MSS-50244-B20, manufactured by Metelics Co. It has two diodes of high barrier needed for the sampler's high dynamic range. Each diode has a junction capacitance of 0.1 pF, junction resistance of 16 Ω and series resistance of 11 Ω. The holding capacitors, shown in Fig. 4.7, are implemented by chip capacitors having low loss and high self-resonant frequency.

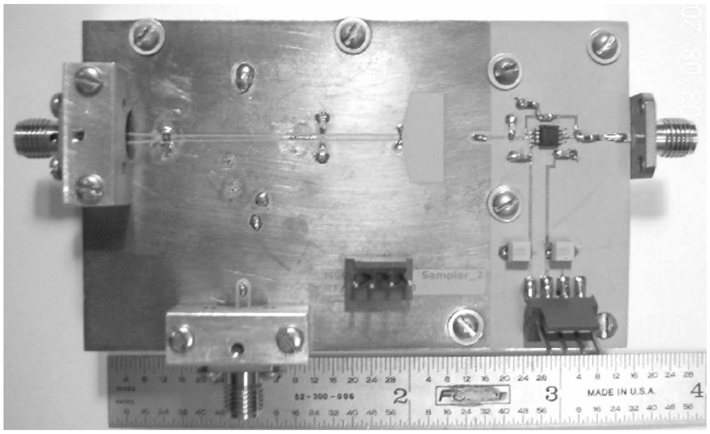

(a)

Fig. 4.9. Top and bottom view of the CSH sampler assembly. The sampling bridge and the baseband circuit are shown in the top view (a) and the SRD pulse sharpening circuit and baseband connections are shown in the bottom view of the assembly (b). The overall dimension of the assembly is 3.3"×2.0"×0.6".

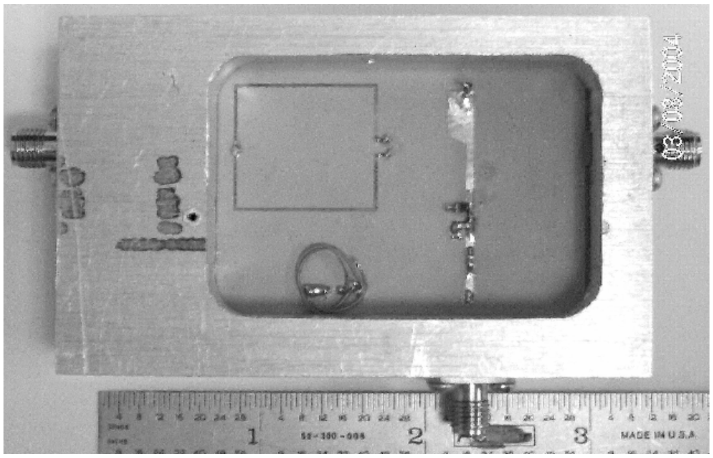

(b)

Fig. 4.9. Continued.

Fig. 4.10 shows the measured and simulated return losses at the RF port for the designed sampler. The measurement result shows a minimum return loss of 15 dB over the entire estimated 5.5-GHz bandwidth and a minimum return loss of 9 dB for a bandwidth up to 10 GHz, and was obtained without the LO pulse signal. It is expected that the return loss without the LO pulse signal should resemble that with the LO signal, because it is averaged out for a large time interval between the applied pulses. The measured return loss therefore corresponds to the diode turn-off condition. Accurate measurement for the return loss under the diode turn-on condition is not really necessary, whereas very cumbersome because it requires additional biasing networks to be attached. The measured return loss implies that the matching of the passive circuitry including the coaxial connection and CSH structure is well achieved. The simulation result, on the other hand, was done assuming the diodes were turned on, resulting in some difference with the measured data as noticed in Fig. 4.10. Nevertheless, the trend of the return loss curves matches each other reasonably well. The equivalent-circuit model shown in Fig. 4.6 was used for the sampling diodes in the simulation. It is deemed that the simulation result should provide a reasonably good estimate for the actual return loss when the sampling diodes are on.

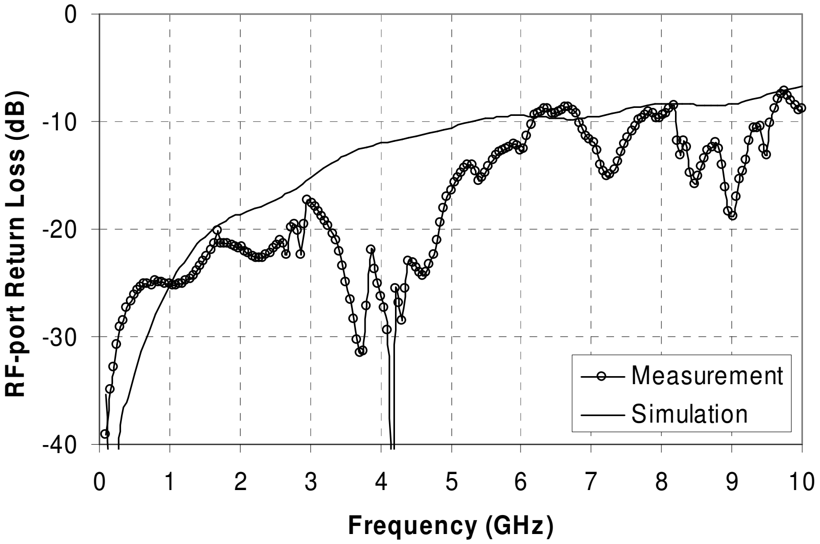

Fig. 4.10. Input return loss of the RF-port.

Fig. 4.11 shows the measured and calculated normalized (or relative) conversion loss of the CSH sampling mixer (without the baseband amplifier). The measured conversion loss is normalized to the minimum conversion loss of the sampler, which was measured as 4.5 dB. The calculated conversion loss was obtained using (4.2) and represents the intrinsic conversion loss of the sampler (normalized to the minimum conversion loss) as described in sub-section B.1. It is noted that the calculated intrinsic conversion loss matches very well with the actual measured normalized conversion loss, signifying the accuracy of (4.2) in predicting the normalized conversion loss and the operating bandwidth of the sampler. As can be seen in Fig. 4.11, the measured 3-dB bandwidth of the sampler is 5.5 GHz, which is in good agreement with the calculated one. With the measured 4.5-dB minimum conversion loss, the sampler exhibits a conversion loss from 4.5-7.5 dB for an RF signal from DC to 5.5 GHz and baseband signal of 20 KHz, representing, to the best of our knowledge, the best conversion efficiency reported to date. The sampler with a 14-dB-gain (opamp) baseband amplifier shows a measured conversion gain from 6.5 to 9.5 dB over a 5.5-GHz RF bandwidth.

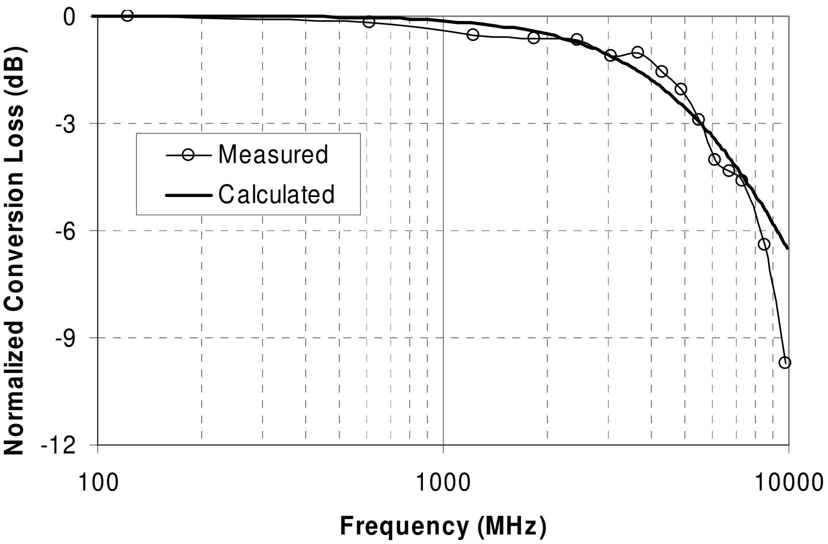

Fig. 4.11. Measured and calculated normalized conversion losses of the CSH sampler.

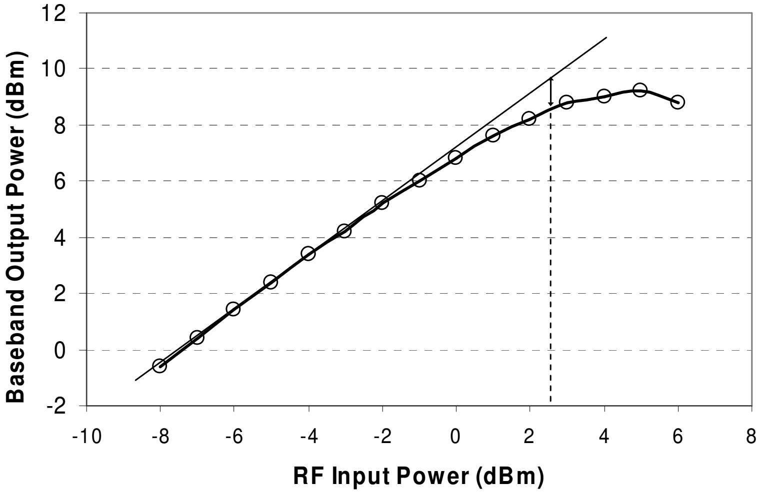

Fig. 4.12. Measured baseband output power of the CSH sampler.

Fig. 4.12 shows the measured baseband output power as a function of the RF input power at a RF frequency of 3 GHz, which is near the center frequency of the designed sampler. The measured 1-dB compression point is 2.5 dBm. To determine the harmonic distortion in the baseband signal, the spurious signal, which is the second harmonic of the down-converted signal, was measured using a spectrum analyzer. For a RF signal of 3 GHz and 0 dBm, the spurious signal level is as low as 20 dBc.

The sensitivity of the sampler was obtained by measuring the noise output power of the baseband signal using a spectrum analyzer. The measured output noise power is -33 dBm for a 3-GHz, -9.9-dBm RF input signal and 2 dBm of the baseband signal output. Using the sensitivity of the spectrum analyzer and the baseband filter bandwidth (1.5 MHz) of the sampler, the sampler's sensitivity, defined as 8-dB tangential sensitivity, was determined as -47 dBm. The dynamic range of the sampler was measured to be more than 50 dB. A summary of the sampler's performance is shown in Table 4.2.

Table 4.2. Summary for the performance of the designed CSH sampler.

Conversion loss (-) and Gain (+)	-7.5 to -4.5 dB (without amp.) 6.5 to 9.5 dB(with amp.)
Baseband Amp. Gain	14 dB
RF Input Bandwidth	5.5 GHz
LO clock source PRF	12 MHz
Spurious	20 dBc typical
-1dB Compression	2.5 dBm
8-dB Sensitivity	-47 dBm
Dynamic Range	> 50 dB
RF VSWR	1.3:1

3) Summary for the CSH sampler

A new planar sampling mixer realized using a combination of coupled-slotlines, CPW and microstrip line has been developed for sub-sampling of UWB video pulse signals. The sampler achieves unprecedented conversion loss of 4.5-7.5 dB (without amplifier) and conversion gain of 6.5-9.5 dB (with amplifier) across a 5.5-GHz RF bandwidth. Its dynamic range is more than 50 dB. The integration of the sampler with the strobe pulse generator and baseband circuit is made without any wires or air-bridges, enabling the circuit to be fabricated using standard low-cost PCB fabrication process with significant reduction in the assembly effort. The design of strobe pulse generators for sampling applications requiring low PRF was also presented. The measured normalized conversion loss agrees well with that calculated using a simple equation. The presented detailed design of the sampler for achieving low conversion loss, suppression of the pulse ringing for low harmonic distortion and good matching along with the newly derived equation for accurate prediction of the conversion loss should be useful for sampler design for UWB applications.

C. Synchronous Sampling Receiver System

1) Design of the synchronous sampling receiver

For the synchronous sampling, two reference clock oscillators should provide proper pulse repetition rate for the LO strobe pulse signal and the RF input signal, respectively. If the sampling mixer properly works, the design problem of the sampling receiver in the system level is to determine PRF's of two clock oscillators required for proper synchronous sampling.

Let us assume that the PRF of the LO strobe pulse is fo and that of the RF input signal is $fR=Nfo+\Delta f$, where N is an arbitrary integer and Δf is a deviation. This relationship between the PRFs of LO and RF is the familiar form in harmonic mixing theory and N=1 in our particular case. Referring to Fig. 4.1, the periods for the RF and LO pulse signal, T_R and T_o, can be written as,

$$T_R = \frac{1}{f_R} = \frac{1}{f_o + \Delta f} \tag{4.4}$$

$$T_o = \frac{1}{f_o} = T_R + \Delta t \tag{4.5}$$

Using (4.4) and (4.5), we can obtain the equation for the deviation frequency Δf,

$$\Delta f = \frac{\Delta t\, f_o^2}{1 - \Delta t\, f_o} \tag{4.6}$$

in terms of the equivalent sampling time interval Δt and the reference frequency f_o. Note that $f_o \approx f_R$ in our case and f_R is needed to determine the proper value of Δf.

The PRF of the transmitting pulse, f_R is determined by two factors. One factor is the required observation time interval for a particular application and the other is the scanning velocity of the radar sensor. The required observation time interval is dependent on the EM wave propagation velocity in the objective medium and the maximum desirable detection range. For the application of the pavement assessment, the calculation of required observation time-interval is straightforward, using the information of the pavement structure shown in Table 2.1 and 2.2, and the result is greater than 10 ns. The scanning velocity of the sensor may be more than 70 mi/h if the sensor is operating on the moving vehicle. Considering the required observation time interval and scanning velocity of the sensor operating on the moving vehicle, we can derive a compromised value for the PRF of the transmitting pulse, f_R=10 MHz. Assuming that $f_o \approx f_R$=10 MHz and Δt=1 ps, the required deviation frequency Δf=100 Hz can be calculated from (4.6).

One interesting question is how many sample points will be produced for a single pulse repetition period of the RF input. In other words, this problem is determining the value M for a single period T_R in Fig. 4.1. We know that Δf is the PRF of the down-converted signal according to general harmonic mixing theory. Therefore, a single pulse repetition period of the down-converted signal,

$$\frac{1}{\Delta f} = M\,T_R \tag{4.7}$$

$$M = \frac{f_o + \Delta f}{\Delta f} \tag{4.8}$$

where (4.8) was derived from (4.4) and (4.7). Using f_o=10 MHz, Δf=100 Hz, M=100 K-samples can be calculated from (4.8). The calculated number of sample points, 100 K, looks too large for a single pulse repetition period, which is a single scan data at one location in the target structure. However, the actual number of sample points per single scan is varied by the ADC processing upon the down-converted signal. For instance, if the sample rate of the ADC, f_s, is the same as f_o=10 MHz, the sampled time interval on the RF input pulse, Δt=1 ps. That means, in the case of 450-ps duration monocycle pulse being used as a transmitting pulse, 450 sample points are reproduced in baseband for a time interval corresponding to the pulse duration, which is obviously an excessively large number of samples. A rule of thumb in the sampling process is that 10 samples for a pulse-duration of a pulse signal can provide good resolution in ADC process. If the sample rate of the ADC is 45 times less than f_o=10 MHz, that is f_s=220 KHz, we can make 10 samples per pulse-duration in this example. In the case of our design, the minimum RF pulse duration is 450 ps, so the sample rate f_s=220 KHz is also appropriate. Using this lower sample rate, the cost for the ADC is significantly down, and the actual number of sample points per single scan is reduced to 2.2 K-samples for 100 Hz baseband PRF. Table 4.3 summarizes the result of the design parameters derived for implementation of the synchronous sampling receiver.

Table 4.3. Design parameters for implementing the synchronous sampling receiver (in the case of minimum transmitting pulse duration, 450 ps, as in our designed transmitter).

Reference clock frequency, fo	10 MHz
Equivalent sampling time interval, Δt	1 ps
Deviation frequency, Δf	100 Hz
Sample rate of ADC, fs	220 KHz
Samples/scan	2.2 K

Selecting two appropriate reference clock oscillators for the transmitter and the receiver is a very critical problem for implementation of the synchronous sampling receiver. First, we need to select the reference clock oscillators according to the design parameters of f_o=10 MHz and Δf=100 Hz. Second, the oscillator output frequency should be very stable with respect to the circuit temperature variation. Third, the oscillators should have small jitter (or phase noise) because large jitter may cause distortion and conversion loss on the down-converted signal due to the sample timing error.

TCXOs (Temperature Controlled Crystal Oscillators) producing 5V HCMOS logic output are usually unable to meet these requirements at low cost. One way to achieve low-cost implementation is to use VC-TCXO (Voltage Controlled TCXO). Most of VC-TCXO manufacturers provide about 10 ppm of the frequency adjustment through the voltage control by which 100 Hz frequency variation is possible for our design. An even larger frequency adjustment range can be achieved by additional mechanical trimmer of the VC-TCXO. Two VC-TCXOs were finally selected for our design as the GTXO-536V model, manufactured by Golledge Electronics because it has very low phase noise (-135 dBc/Hz @ 1 KHz) and is a low-cost product.

2) Fabrication and performance of the synchronous sampling receiver

A selected VC-TCXO is used in the clock driving circuit of the transmitter as a reference clock. Another identical model of VC-TCXO is used in the clock driving circuit of the strobe pulse generator of the receiver. As indicated in Fig. 4.2, the integrated sampling mixer is a complete receiver circuit for our application, which includes the sampling mixer, the strobe pulse generator, VC-TCXO, and baseband circuit. Fig. 4.13 shows the photograph of the integrated sampling mixer fabricated on a single PCB using the same substrate as the one used for the CSH sampling mixer.

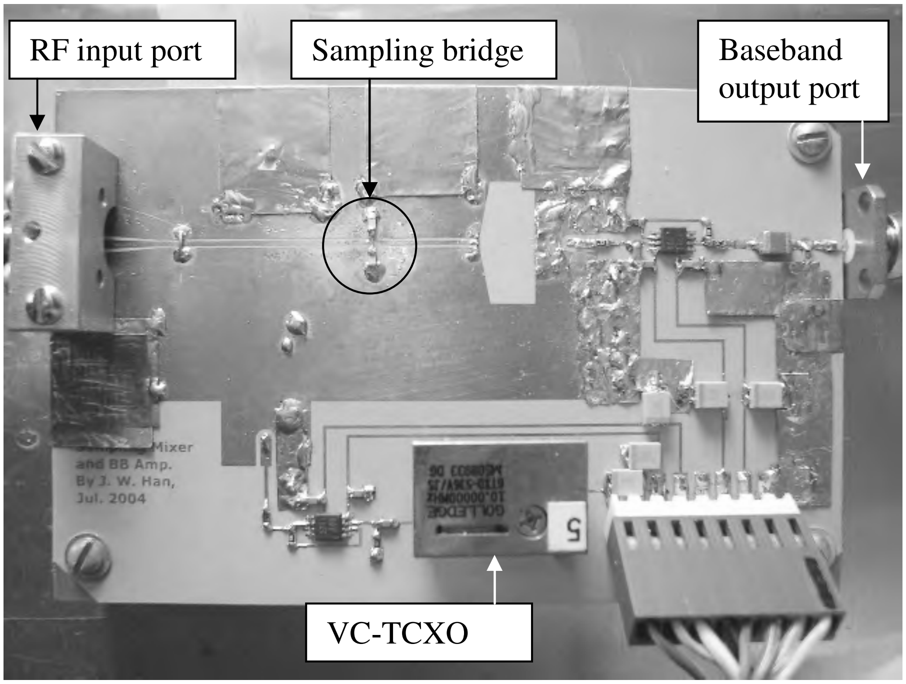

Fig. 4.13. Top view of the receiver circuit (integrated sampling mixer) fabricated as a MIC.

The performance of the designed receiver (the integrated sampling mixer) is measured in terms of the quality of the reproduced baseband signal by the receiver itself in comparison with the reproduced signal through the commercial sampling oscilloscope. The measurement system shown in Fig. 4.14 was used to measure both down-converted (reproduced) signals by the sampling oscilloscope and the designed receiver. In Fig. 4.14, path 1 represents the fact that the transmitted pulse from the transmitter is directly measured by the sampling oscilloscope by its own down-conversion function. Path 2 represents the fact that the same transmitted pulse is down-converted by the designed receiver and the down-converted signal is then measured by the sampling oscilloscope. The designed transmitter should be used here to test the performance of the entire synchronous sampling receiver system incorporating the transmitter.

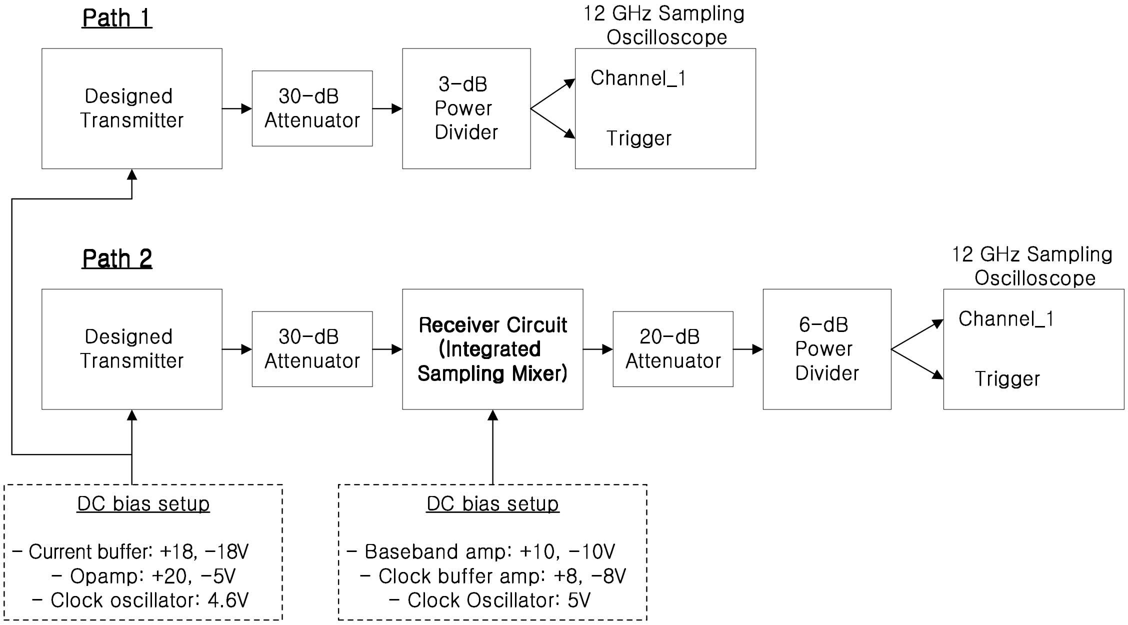

Fig. 4.14. System setup for measuring the performance of the synchronous sampling receiver system.

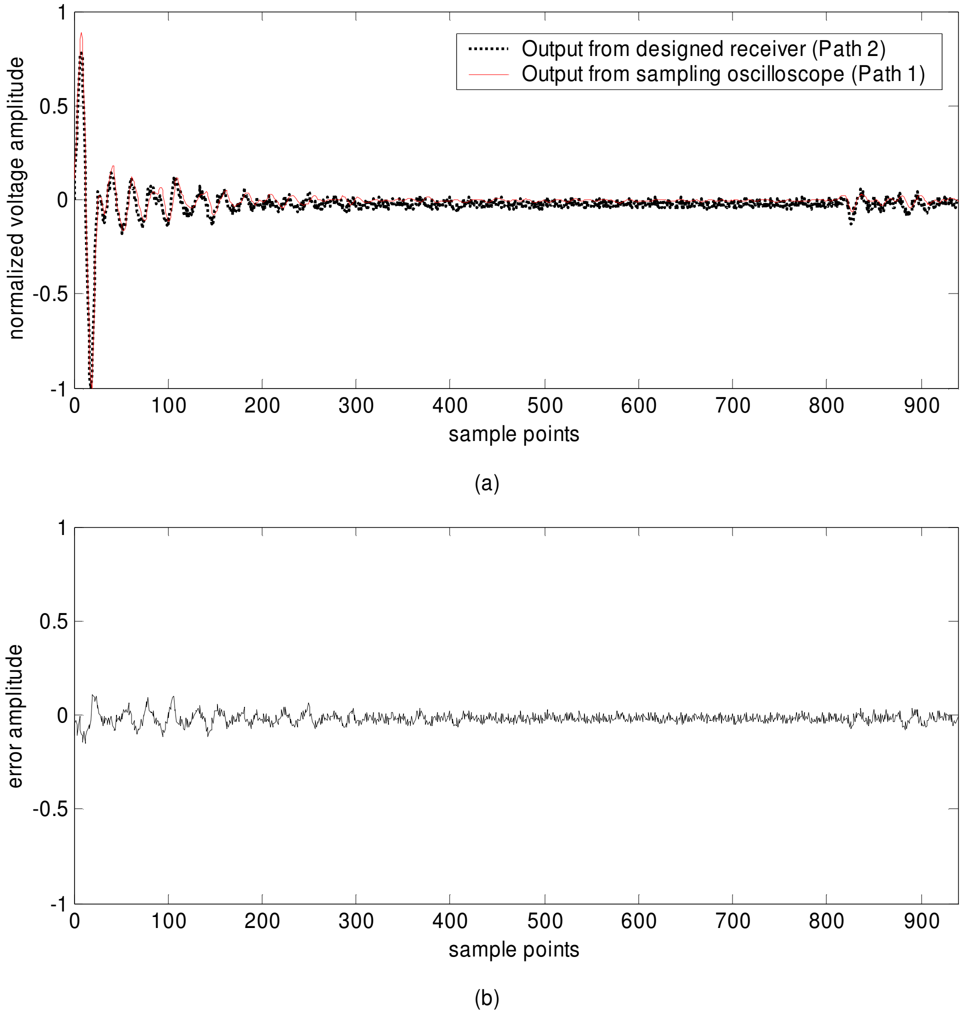

Fig. 4.15. (a) Two measured waveforms through the sampling oscilloscope; one is the direct measurement of the transmitter output; the other is the measurement on the down-converted signal by the designed receiver. (b) Errors between two measured waveforms are shown in (a).

Two measurements for each of path 1 and 2 were done and down-converted signals were recorded in the sampling oscilloscope. The measured results are shown in Fig. 4.14. The transmitter output signal used for this measurement was the monocycle pulse with duration 450 ps, which is the minimum pulse duration of the designed transmitter. The minimum pulse duration was used to test whether the BW of the designed receiver can cover up to the maximum BW of the transmitting pulse. In Fig. 4.14(a), two down-converted signals by the designed receiver and by the sampling oscilloscope itself are plotted together and show good coincidence with each other. Fig. 4.14(b) shows the measured error values between two signals. The calculated RMS (Root Mean Square) error value based on the measured error values is 0.035, which means that the difference between two down-converted signals is only 3.5 % of the peak amplitude of the signal. As a conclusion, the performance measurement result shows that the designed synchronous sampling receiver can reproduce the transmitted pulse signal with negligible error.

D. UWB LNA (Ultra-Wideband Low Noise Amplifier)

The designed LNA uses a wideband MMIC amplifier, MMA710-SOT89, which is a Darlington HBT amplifier manufactured by Metelics. This MMIC amplifier has a wideband flat gain over 100 KHz to 4 GHz, which agrees with our required bandwidth for the transmitting pulse signal. The typical specifications of the amplifier are shown in Table 4.4.

Table 4.4. Typical specifications of the MMIC amplifier, MMA710-SOT89.

Parameter	**Typical value @ 7V bias**	**Maximum value**
Gain	12 dB	
Output Power (P_{1dB})	21 dBm	
Input Match	1.5:1	2:1
Output Match (10MHz-2.2GHz)	1.8:1	2:1
Output Match(2.2GHz-4GHz)		3.5:1
Noise Figure	6.5	7
OIP3	35 dBm	

The main reason for selecting this amplifier among many other commercial products with similar performance is the higher 1-dB compression output power of this amplifier. As indicated in Table 4.4, the noise figure of the amplifier seems unsuitable for normal LNA, while in our impulse radar applications, the clutter signal rather than noise is usually the limiting factor; hence this noise figure may be acceptable.

The stability of the amplifier was examined through the circuit simulation using ADS [73], in which the measured S-parameter data of the amplifier provided by the manufacturer was used. Fig. 4.16 shows the circuit simulation results, in which “without stabilization” is for the amplifier device only and “with stabilization” is for the revised circuit by a stabilization technique that will be described subsequently. The design frequency band of interest is 0.2 to 5 GHz, which is a little wider than the instantaneous frequency band of the input pulse signal.

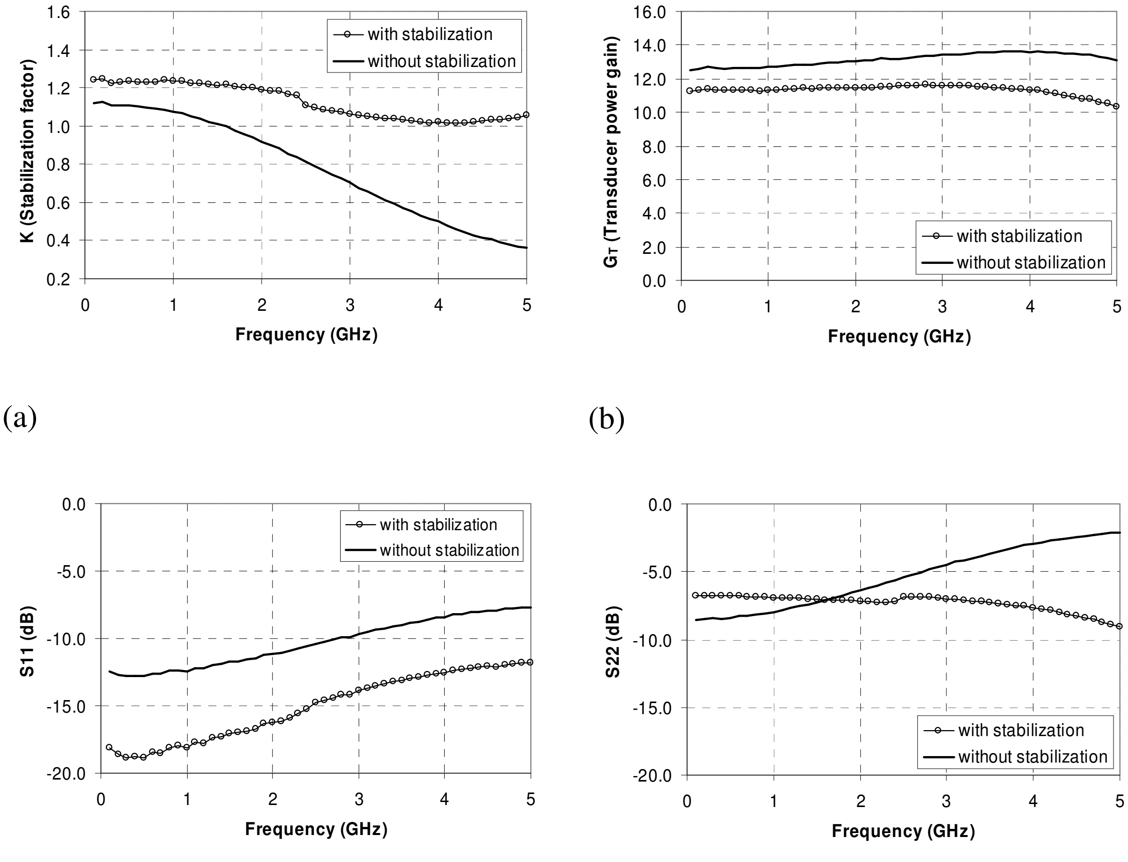

(a) (b)

(c) (d)

Fig. 4.16. Circuit simulation results for the LNA circuits designed with and without stabilization.

Using the well known stabilization factor K, we can examine the stability of the amplifier circuit [74]. The simulation result for the stabilization factor K in Fig. 4.16(a) shows that for the circuit including only the amplifier itself without stabilization, K is less than 1 at more than 1.5 GHz, which means that the circuit is not unconditionally stable at higher frequency range. Furthermore, the performance of the input and output matching with respect to the normalization impedance 50 Ω is also not good enough.

The output return loss is much less than the normal standard value of 10 dB or equivalently is much higher than 2:1 VSWR.

Design of the LNA circuit is required to solve the stabilization problem and to improve the matching performance for the input and output port. A well–known and simple way to achieve broadband stabilization is to use a series or shunt resistive loading at the output of the amplifier [74]. This simple approach is also attractive in view of the fabrication of an MIC amplifier. The stabilization problem using the resistive loading method can be described as in the circuit diagram shown in Fig. 4.17.

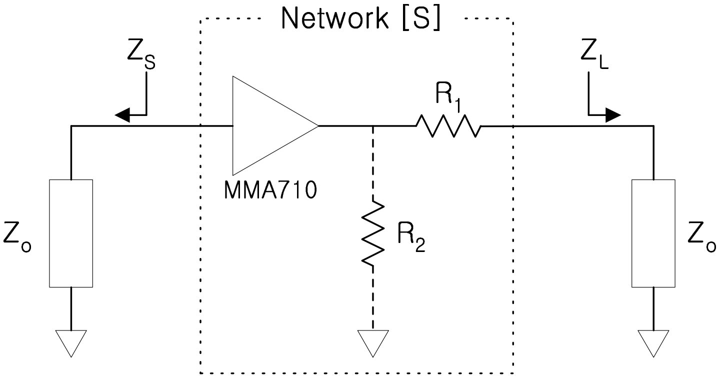

Fig. 4.17. Circuit diagram representing the stabilization of the amplifier using resistive loading technique.

In Fig. 4.17, the overall circuit including the amplifier device and the stabilization resistor R_1 or R_2 is defined as a generic network represented by an S-parameter [S].

Notice that from the definition of the transducer power gain G_T, $G_T=|S_{21}|^2$ when $\Gamma_s=\Gamma_L=0$ in the case such as that shown in Fig. 4.17.

The first design objective is to find an optimum R_1 or R_2 that can support unconditional stability of the circuit and maximize G_T. Using the parameter sweep function of ADS circuit simulation, it has been found that, in our case, the series resistive loading is more effective than the shunt one in terms of the stability and G_T. The optimum value of R_1 is also determined by the parameter sweep of R_1 in ADS, which is 25 Ω with respect to the stability and G_T. The simulation result for the stabilized circuit using R_1=25 Ω is shown in Fig. 4.16, which is represented as "with stabilization." As shown in the simulation result, the stabilized circuit has unconditional stability for full frequency band and even better input and output matching performance, whereas the gain is sacrificed in 1dB. Notice, however, that the output matching performance is still not satisfactory with 2:1 VSWR.

An additional output matching circuit needs to be designed to improve the output matching performance. The circuit diagram shown in Fig. 4.18 illustrates the required matching circuit design problem. We need to design an output matching circuit that makes $Z_t=Z_o$.

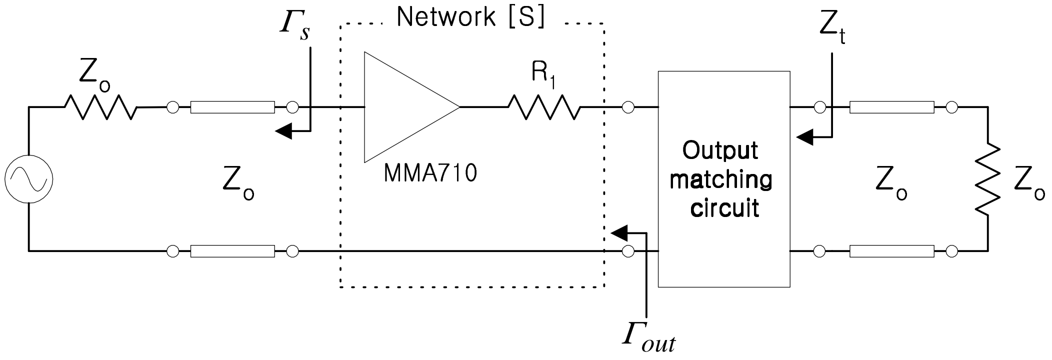

Fig. 4.18. Circuit diagram illustrating the problem of output matching circuit design.

First, we need to know the value of Γ_{out} defined in Fig. 4.18 and,

$$\Gamma_{out} = S_{22} + \left.\frac{S_{12}S_{21}\Gamma_s}{1-S_{11}\Gamma_s}\right|_{\Gamma_s=0} = S_{22} \tag{4.9}$$

where the condition $\Gamma_s = 0$ was used. we have already calculated the S-parameters of the network [S] at the previous stage through ADS circuit simulation and Γ_{out} @ 3GHz = S_{22} @ 3GHz = $0.45\angle{-60^\circ}$, where the reference frequency 3 GHz is chosen arbitrarily to improve output matching at higher frequency band. Using the Smith-chart, it can be found that the normalized impedance $z_{out} = Z_{out}/Z_o = 1\text{-}j1$. In order to make z_t=1, the output matching circuit should be a series inductance L_s having the normalized reactance value 1, and the value of L_s turns out to be 2.65 nH for 3 GHz. This design approach only considers a single component for the matching circuit and also a single frequency; thus the matching performance may not be good enough to cover a wide frequency band.

The simulation result for the circuit including the single matching component shows that the output return loss is not acceptable, especially for a higher frequency than 4 GHz. To complete the design of the matching circuit, additional components need to be added to the initial design for improving the performance at other frequency bands.

The subsequent design follows a similar procedure to that followed in the initial design. Now, the network [S] includes the matching component L_s as well as MMA710 and R_1. For this updated network [S], S_{22} @ 4.3 GHz = $0.4\angle 90°$ can be obtained by the circuit simulation, where the frequency 4.3 GHz was chosen arbitrarily to consider the higher frequency band. The resulting normalized output impedance $z_{out}= 0.72+j0.7$ and the admittance $y_{out}= 0.72-j0.7$. We consider the admittance value here to obtain shunt matching components, which makes L-matching circuit by concatenation with the previous series inductance component L_s. From the matching condition, $y_t = 1 = y_{out}+y_m$, where y_m represents the normalized admittance of the additional matching circuit. Therefore we can obtain $y_m = 1-y_{out} = 0.28+j0.7=g_m+jb_m$, which means that the additional components to be concatenated are a shunt resistance and a shunt capacitance. It is straightforward to calculate these component values and the result is that the resistance R_m=180 Ω and the capacitance C_m=0.5 pF. The overall LNA circuit diagram including the designed output matching circuit is shown in Fig. 4.19(a). The simulation results for the circuit in Fig. 4.19(a) are shown in Fig. 4.20 and represented as “before optimization.” The results show that the output return loss has been improved over the entire frequency band compared to the case without matching circuit, while the output return loss has deep null at 4.3 GHz and the input return loss is deteriorated. It is reasonable to attempt the optimization of the matching circuit to improve this result: to have flat output return loss across overall frequency band and to improve the input return loss.

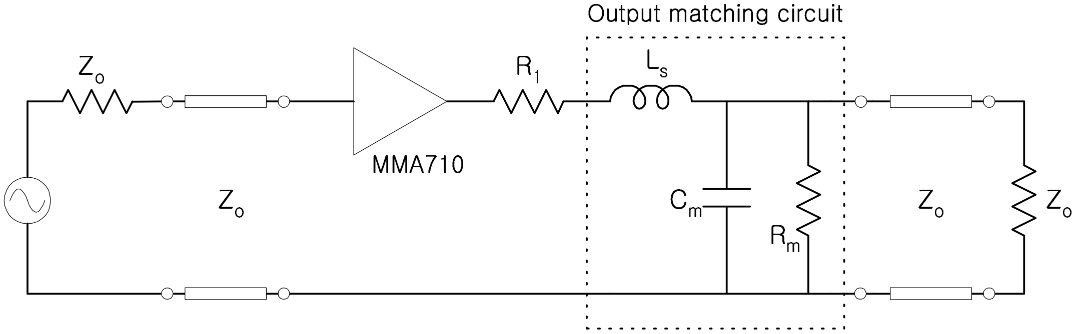

(a)

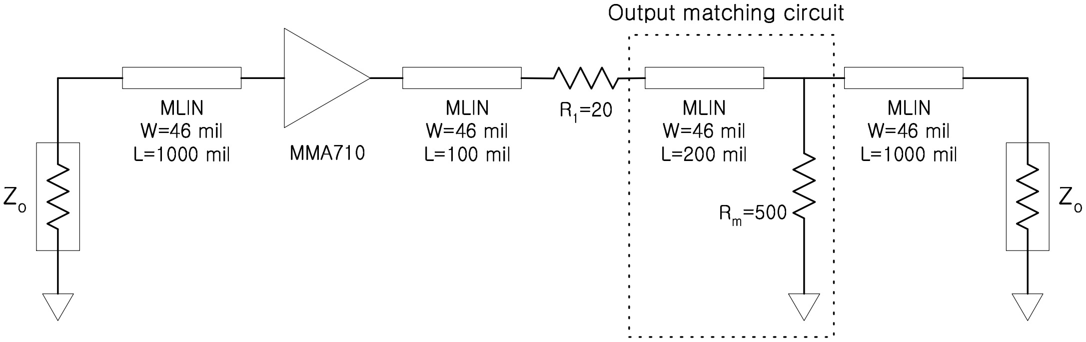

(b)

Fig. 4.19. Circuit diagram of the stabilized LNA circuit including the output matching circuit. (a) Design result using only lumped elements, and (b) Design result using distributed elements (final design).

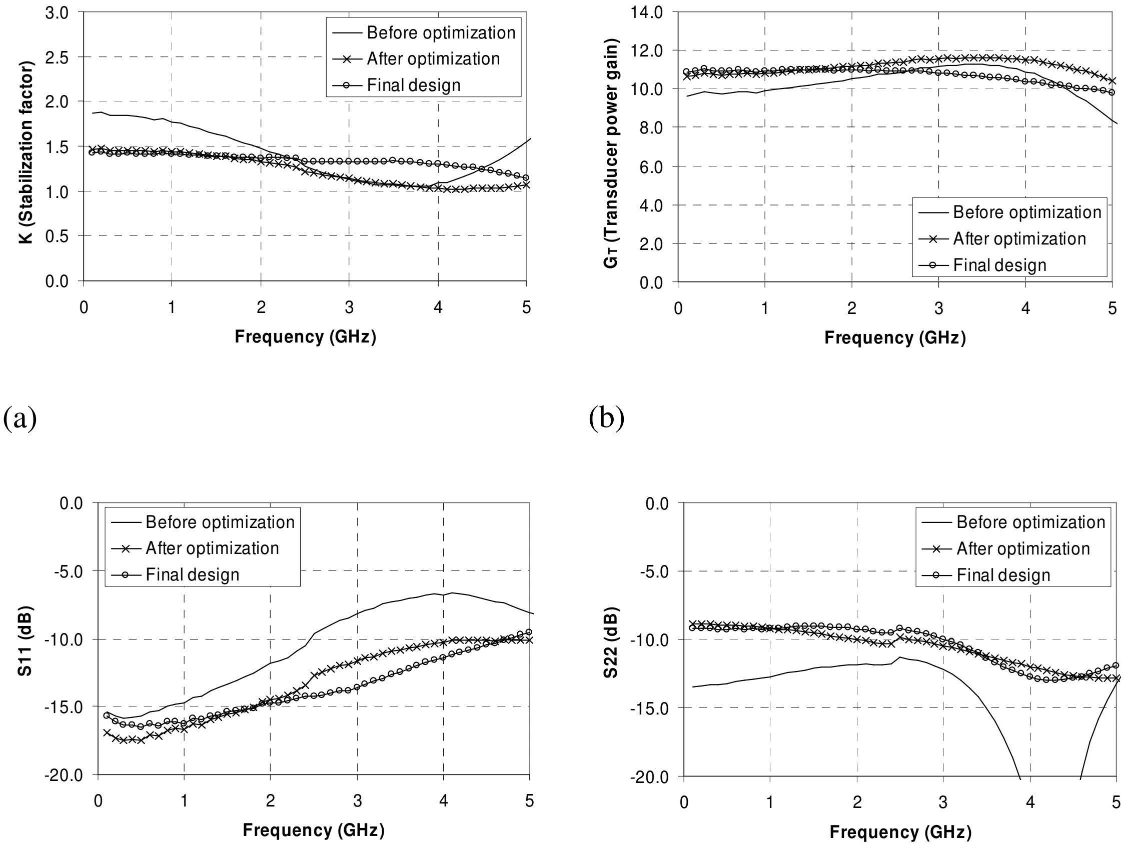

(a)

(b)

(c)

(d)

Fig. 4.20. Circuit simulation results for the designed LNA circuits shown in Fig. 4.19.

I have used the optimization tool in ADS to optimize the output matching circuit with respect to the input and output return loss and stabilization factor K. The resulting optimized component values are Ls=1 nH, Cm=0.1 pF and Rm=500 Ω. The performance simulation results are shown in Fig. 4.20 and represented as “After optimization.” The results show that the overall performance of the stabilization and the input and output matching are acceptable. In particular, the optimization leads to significant improvement in input return loss while it sacrifices output return loss.

Even though the optimized circuit of Fig. 4.19(a) has satisfactory performance, we did not consider any transmission lines in the circuit structure for its implementation. Based on the optimized circuit components, I have designed the final LNA circuit that can be implemented on the microstrip structure. The substrate used in the final design is the same the one as used in the sampling mixer, which is RT/duroid 6010 with a relative dielectric constant 10.2, thickness 0.127 cm, and loss tangent 0.0023. The final designed circuit is shown in Fig. 4.19(b) in which MLIN represents a microstrip line with the width W and the length L. The original output matching circuit is replaced by a short length microstrip line and a resistance R_m. This is reasonable if we consider that a microstrip transmission line has a series inductance and a shut capacitance components. One factor to be noted is that the shunt resistance R_m can be replaced by an internal resistance of the wideband RF-choke (RFC) to be used for the DC bias. Although the final circuit does not show the bias circuit, the bias voltage should be applied through a wideband RF-choke (RFC), by which the RF performance should not be disrupted. I have used the same RFC as used in the design of the tunable pulse generator, which is ADCH-80A manufactured by Mini-Circuits. This RFC is known to have an internal resistance 500 to 800 Ω and hence it can replace the shunt resistance R_m. The simulation results for the final circuit of Fig. 4.19(b) are shown in Fig. 4.20 as “Final Design.” The results are very similar to those of the optimized circuit and show acceptable performance in all aspects.

Fig. 4.21 shows the photograph of the fabricated circuit, which includes the necessary bias circuit as well. Fig. 4.22 shows the measured output waveform of the fabricated LNA circuit along with the input monocycle pulse signal. The input signal is generated by the designed transmitter and its pulse duration is 450 ps. The measurement result shows that the designed LNA can amplify the pulse signal with polarity inversion and only small side-lobe ringing occurs in the output. The measured gain of the LNA for the pulse signal is 9.2 dB, which is close to the design value of 10 dB.

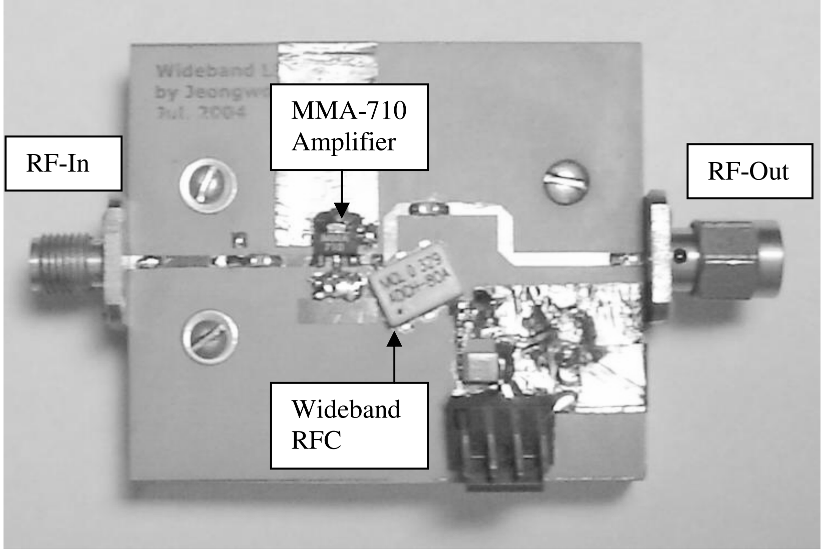

Fig. 4.21. Photograph of the fabricated UWB LNA circuit.

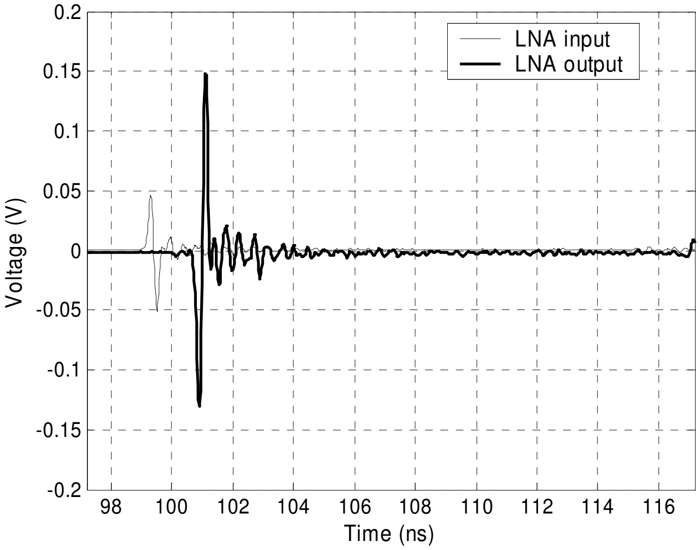

Fig. 4.22. Measured input and output monocycle signal waveforms of the designed LNA circuit.

CHAPTER V

ANTENNA DESIGN

The antenna of the impulse radar system is another critical component for pulse signal transmission. For the impulse radar system, the antenna should be ultra-wideband (UWB) and be able to radiate or receive a short pulse signal without undesirable distortion on the transmitting or receiving signal waveform. The antenna gain is also important in our design. The high gain antenna is of benefit in respect of signal transmission efficiency and signal detection. In respect of transmission efficiency, the high gain antenna enables signal transmission with low loss of transmitting power. In respect of signal detection, the high gain antenna enables us to reduce the clutter signal coming from scatters other than the pointing target, since the narrow beam width of the high gain antenna supports greater focusing of the radar sensor to the target. The antenna input reflection should be minimized to avoid multiple reflections between antenna and transmitter or antenna and receiver, which may produce some clutter-like signals and increase the false alarm rate. It is difficult to find a UWB antenna satisfying the required performance for a specific frequency band in the commercial market, and hence it is usual to design and fabricate the antenna for each purpose.

There are well-known types of UWB antennas available for short pulse transmission. Typical examples are TEM horn, bow-tie, vivaldi and conical antennas [32], [75]-[80].

The interesting characteristic of these antennas is their radiation characteristics for short pulse signals, showing much less undesirable distortion on the transmitting and receiving signal waveform.

Historically, most impulse radar sensors have used TEM horn type antennas because of their high gain, linear phase characteristic and easy fabrication. A modified version of the TEM horn antenna, called microstrip quasi-horn antenna or quasi-horn antenna for short, was developed in our lab and has been used successfully for other subsurface penetrating radars [14], [81]. The conventional TEM horn is basically a Non-Uniform Transmission Line (NUTL) structure realized by parallel-plate transmission line. The microstrip quasi-horn also uses the NUTL but realized by microstrip-line structure. There are advantages in the microstrip quasi-horn antenna compared to the conventional TEM horn. First, its physical size is relatively smaller than the TEM horn. Second, since the input feeding structure of the quasi-horn is compatible with the microstrip line, easy implementation of input feeding is possible in most designs without any special transition. Lastly, when two identical antennas are used for a bi-static configuration of a radar system, two quasi-horn antennas can be assembled into an antenna system with ease thanks to its smaller size because of their inherent structure using ground plate.

The microstrip quasi-horn antenna was designed for transmission of monocycle pulse signals with pulse duration in the range of 400 to 1200 ps, which corresponds to the output pulse duration of the designed tunable pulse generator. The measured performance of the designed antenna shows 2:1 input VSWR for 0.3 to a more than 6 GHz frequency band. A more rigorous design procedure following the design method of TEM horn proposed by Theodorou was applied to our design [22], [82]. The applied design method is to optimize the antenna dimensions for given allowable input reflection and especially to minimize the pulse stretching effect of the TEM horn type antenna. The performance of the designed antenna was examined first through EM simulation using Microwave Studio [83]. The time domain simulator of Microwave Studio lends itself to the simulation of the microwave structure using a UWB pulse signal. More optimization on the antenna design was done using Microwave Studio with respect to the terminating impedance at the open-end of the antenna to minimize reflection occurring at the open-end transition [84].

The measured antenna gain for the designed microstrip quasi-horn antenna is more than 12 dBi for frequencies higher than 2.5 GHz. To measure the waveform distortion occurred by the designed antenna, I placed transmitting and receiving antennas facing each other at some distance and measured the transmitted waveform in time domain. The measurement results show that the designed antenna can transmit and receive 400 to 1200 ps monocycle pulses effectively with only small ringing.

A. Design of the Microstrip Quasi-Horn Antenna

The basic structure of the microstrip quasi-horn antenna is shown in Fig. 5.1. As indicated in the figure, the antenna is an end-fire traveling-wave antenna using NUTL. The top conductor and the bottom ground plate constitute a non-uniform microstrip transmission line.

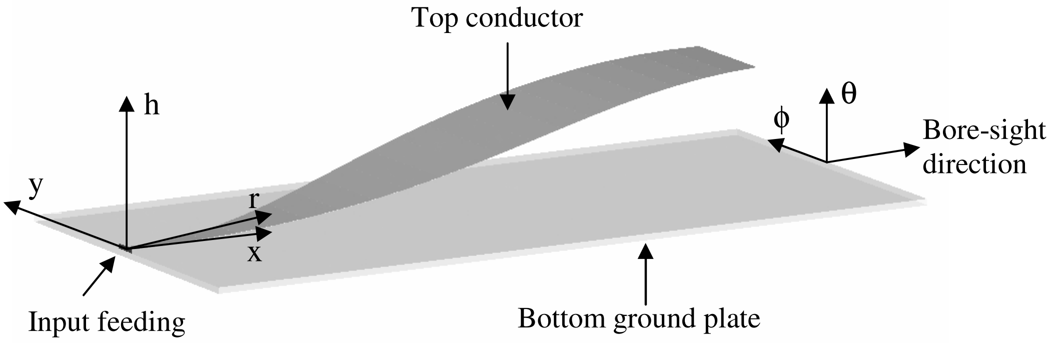

Fig. 5.1. Generic configuration of the microstrip quasi-horn antenna.

An optimum design of the quasi-horn antenna can be achieved by following the design method for the TEM horn antenna proposed by Theodorou since both antennas are basically NUTL structures. In view of electromagnetic analysis, there is also a good similarity between the TEM horn and the quasi horn because the parallel-plate transmission line of the TEM horn has a similar structure to the microstrip line structure of the quasi-horn if the image theory is applied to the microstrip line.

Let us define the x-axis and r-axis along the top conductor as indicated in Fig. 5.1. X is defined as the total length of the antenna in x direction and L as the total length of the antenna in the radial axis r direction. As in case of the TEM horn antenna, E-plane of the quasi horn is along the θ direction and H-plane is along the ϕ direction, according to the notation defined in Fig. 5.1.

Hecken derived a solution for optimum characteristic impedance variation of the NUTL for a given maximum allowable input reflection coefficient [85], which is

$$ln\, Z(x) = \frac{1}{2} ln[Z(0)Z(X)] + \frac{1}{2} ln\left[\frac{Z(X)}{Z(0)}\right] G\left(B, \frac{2x}{X}\right) \tag{5.1}$$

where Z(x) represents the characteristic impedance at position x. The function G and its parameter B are defined by Hecken as shown in the following equations, (5.2) to (5.4). The G function is defined as

$$G(B,\xi) = \frac{B}{sinh\, B} \int_0^{\xi} I_o\left(B\sqrt{1-\xi'^2}\right) d\xi' \tag{5.2}$$

where $\xi = 2x/X$, X is the length of the NUTL impedance transformer and $I_o(\cdot)$ is the Bessel function of the first kind with zero order. The parameter B is related to the maximum allowable magnitude of input reflection coefficient R(0) such that

$$|R(0)|_{max} = tanh\left[\frac{B}{sinh\,B}(0.21723)\sqrt{\left\{\frac{Z(X)}{Z(0)}\right\}}\right] \tag{5.3}$$

The parameter B is also related to the length and the lower frequency limit of the antenna such that

$$\beta_{min} X = \sqrt{\left(B^2 + 6.523\right)} \tag{5.4}$$

where β_{min} represents the phase constant for the lower frequency limit f_{min}.

Theodorou verified in theory that the radiated pulse signal through TEM horn is stretched owing to different traveling paths of the signal along the antenna structure and the pulse stretching is minimized in boresight direction. He derived a simple equation for the maximum pulse stretching time in boresight direction on the E-plane [22],

$$t_{max} = \frac{L}{u}(1 - cos\,a) \tag{5.5}$$

where u is the phase velocity of the electromagnetic wave assumed as TEM wave and a is the apex angle between x and r axis. This result implies that the maximum pulse stretching comes from two the most different traveling paths along the antenna, one is the path along the conductor and the other is the path along the center axis of the TEM horn. The pulse traveling in the TEM horn is similar to that in the quasi-horn if we consider it after applying the image theory to the microstrip structure of the quasi horn. Therefore equation (5.5) is valid for the quasi horn design to obtain only an approximate result.

Using design equations from (5.1) to (5.5), we may begin the design of the quasi horn antenna. Assume that maximum allowable input reflection $|R(0)|_{max} = 0.3$, which corresponds to 10 dB of input return loss. For this value of allowable input reflection, the design parameter B can be determined as 2.1 using (5.3). Assuming that the lower limiting frequency of the antenna is 0.3 GHz and the apex angle a=10°, the required total length of the antenna, X, can be calculated as 0.526 m using (5.4). The total length in the radial direction, L, is 0.534 m since $X=L\ cos(a)$. Using (5.5), the calculated pulse stretching time in boresight direction is only 27 ps, which is an acceptable value for our design and means that the assumption for the apex angle 10° is reasonable.

To calculate the characteristic impedance variance along the conductor, Z(x), using (5.1), we need not only to know the required values of the design parameter B and the total length X but also to decide the value of the terminating characteristic impedance at the open end of the antenna, Z(X). We know that the intrinsic impedance of the free space is 377 Ω, which is correct only for the spherical wave in free space. However, the transmission mode at the end of the antenna is not the same as the spherical wave in free space so that 377 Ω of the intrinsic impedance may not be the optimum value of the terminating impedance Z(X) in order to obtain smooth transition at the end of the antenna [85]. As will be shown later, I decided the optimum value of Z(X) through simulations of the antenna structures with several different values of the Z(X) using a 3D EM simulator, Microwave-Studio. The optimum values of Z(x) for a certain value of Z(X) were obtained by calculation of (5.1) and (5.2) using Matlab [86] programs.

The next step is the design of the antenna shape in h-direction, in other words, determination of the height values along the x-axis. Any kind of traveling-wave antenna with NUTL structure needs to avoid any abrupt transition in the shape across the entire antenna structure to minimize the chance of undesirable reflection occurring in the transition. Another factor to be considered with care is the shape at the aperture end of the antenna. If the shape of the aperture end is flaring, then the radiating wave is likely to be a spherical wave producing distortion in the pulse waveform. Therefore, it is important to maintain the top conductor in parallel with the bottom ground plate at the end of the aperture so that the radiating wave not be spherical but planar [2]. Keeping in mind these design factors, we may come up with several smooth antenna shapes. Lee has attempted to make several different antenna shapes in h-direction for quasi horn antenna [14], though the result does not show any noticeable difference for different designs in terms of antenna gain. This implies that the antenna shape in h-direction is not so sensitive to minor changes; only making smooth transition and parallel aperture end is important design factors for the antenna shape.

I designed the antenna shape in h-direction using a sine square function, which satisfies the required design factors for the antenna shape. The height values of the top conductor along the x-axis is represented as h(x) and is defined by the equation,

$$h(x) = h_i + h_o \sin^2\left(\frac{\pi}{2}\frac{x}{X}\right) \tag{5.6}$$

where $h_o = X \tan(a)$ and $h_a = h_i + h_o$ as defined in Fig. 5.2. The resulting shape is similar to that shown in Fig. 5.2, representing a side view of the quasi horn antenna.

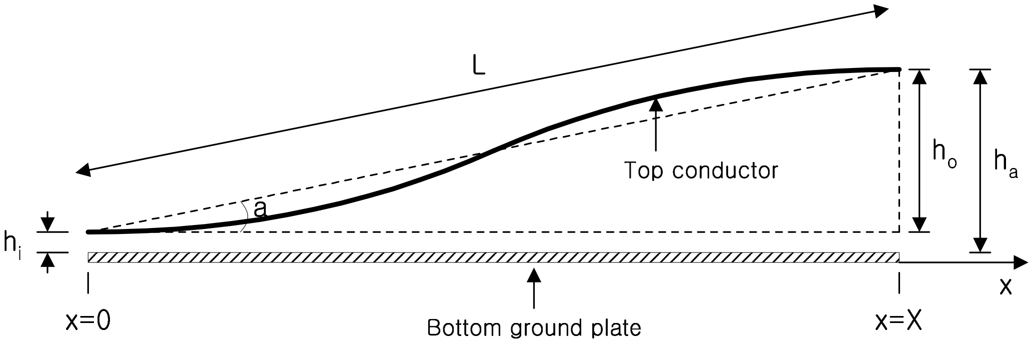

Fig. 5.2. Side view of the microstrip quasi-horn antenna when the antenna shape is designed as sine square function.

We already know all the parameter values required to calculate (5.6) except h_i. This parameter is also an important one related to the higher-order mode generation inside of the antenna aperture in the case of TEM horn type antenna structure. For the TEM horn antenna using parallel-plate transmission line structure, there is a cutoff frequency pertaining to each higher order mode. For higher frequencies than the cutoff frequency of a higher order mode, the antenna may generate the corresponding higher order mode signal. The cutoff frequency is related to the plate separation between top and bottom conductors at the input feeding of the antenna such that,

$$\lambda_c = \frac{2S}{n} \tag{5.7}$$

where λ_c is the wavelength at the cutoff frequency, S is the plate separation at the input feeding, and n is the mode number of the higher order mode. In our case, the frequency band of the transmitting pulse is 0.15 to 3.7 GHz. Taking into account some margin, the required cutoff frequency in our design may be 5 GHz. The mode number n should be 1 because we do not want the generation of higher order mode larger than 1. In this case, the required separation at the feeding can be calculated as 30 mm using (5.7). In case of a quasi horn antenna, the separation at feeding h_i is half of S, hence h_i should be less than 15 mm. In actual design, I used only h_i=2 mm in order to make a simple transition from antenna input feeding to the SMA coaxial connector, which is necessary to build a SMA coaxial input feeding to the antenna.

The final step to complete the initial antenna structure design for given variance of characteristic impedance Z(x) and height values h(x) is the determination of the width dimensions of the top-conductor, which are y-direction values along the x-axis. For each sampled coordinate of the x-axis, the width value W(x) is determined in such a way that it could make the corresponding characteristic impedance value Z(x) for given height h(x). The number of sample coordinates in the x-axis should be large enough not to cause any abrupt transition on the antenna shape. In our case, I used 21 equivalently sampled coordinate values on the x-axis. Table 5.1 shows an example of the design result for given conditions, $|R(0)|_{max}=0.3$, $B=2.1$, $f_{min}=0.3$ GHz, and $Z(X)=130\ \Omega$. Table 5.1 specifies the characteristic impedance Z(x), the height H(x), and the width W(x) for each coordinate value of the x-axis.

Table 5.1. Design results for the dimensions of the microstrip quasi-horn antenna.

x-axis (mm)	Z(x), (Ω)	H(x), (mm)	W(x), (mm)
0.0	50.0	2.0	9.7
26.3	51.4	2.6	12.0
52.6	53.1	4.3	19.2
78.9	55.2	7.1	30.1
105.2	57.7	10.9	43.4
131.5	60.5	15.6	58.0
157.8	63.8	21.1	72.5
184.1	67.4	27.3	86.2
210.4	71.4	34.0	98.1
236.7	75.9	41.1	107.5
263.0	80.6	48.4	114.6
289.3	85.7	55.6	118.6
315.6	91.0	62.7	120.3
341.9	96.4	69.4	119.9
368.2	101.9	75.6	117.7
394.5	107.4	81.2	114.1
420.8	112.7	85.9	109.5
447.1	117.7	89.7	104.5
473.4	122.3	92.5	99.2
499.7	126.4	94.2	93.9
526.0	130.0	94.8	88.7

The antenna design needs to be optimized especially for the terminating characteristic impedance Z(X) at the open-end of the antenna. I have tried to find the optimum value of Z(x) through multiple simulations for different antenna structures designed for some typical Z(X) values 377, 180, 130 and 100 Ω.

Fig. 5.3 shows two designed antenna structures selected to show two extreme cases of design. The antenna in Fig. 5.3(a) is designed for Z(X)=377 Ω, which corresponds to the design with inferior performance and the one in Fig 5.3(b) is designed for Z(X)=130 Ω, which corresponds to the design with superior performance.

3D EM simulation was performed for the designed antenna structure using the time-domain simulation package of Microwave Studio. Fig. 5.4 shows the input return loss data obtained from simulations for two designed antenna structures shown in Fig. 5.3. The results shown in Fig. 5.4 indicate that the antenna structure of Fig. 5.3(b) using Z(X)=130 Ω has significantly improved performance for the input matching.

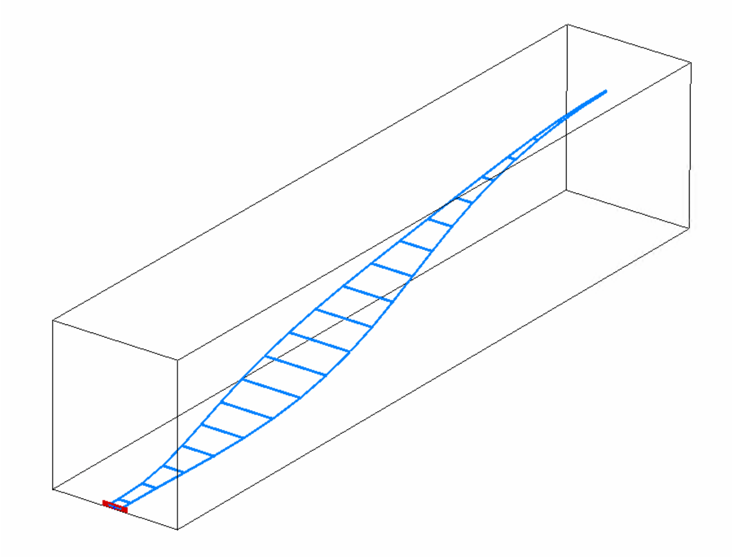

(a)

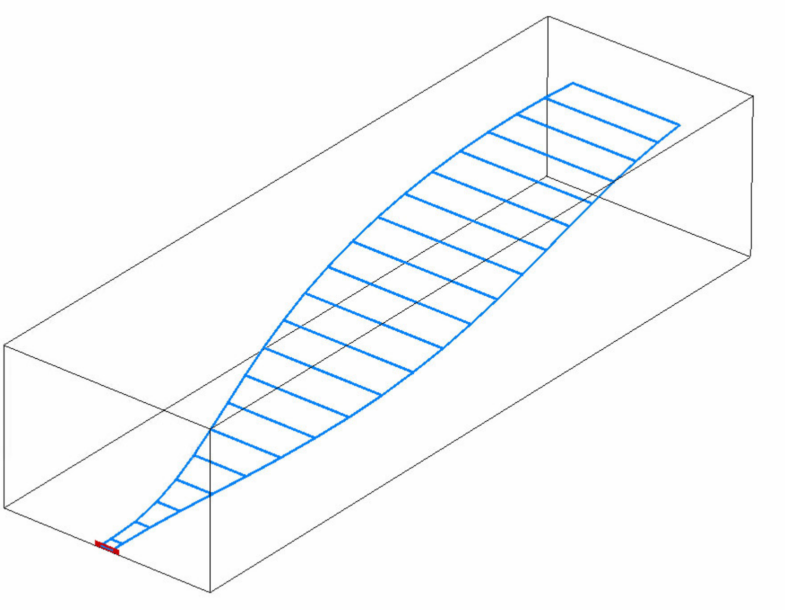

(b)

Fig. 5.3. Design results of the microstrip quasi-horn antenna for different open-end impedance value, Z(X). (a) for Z(X)=377 Ω, (b) for Z(X)=130 Ω.

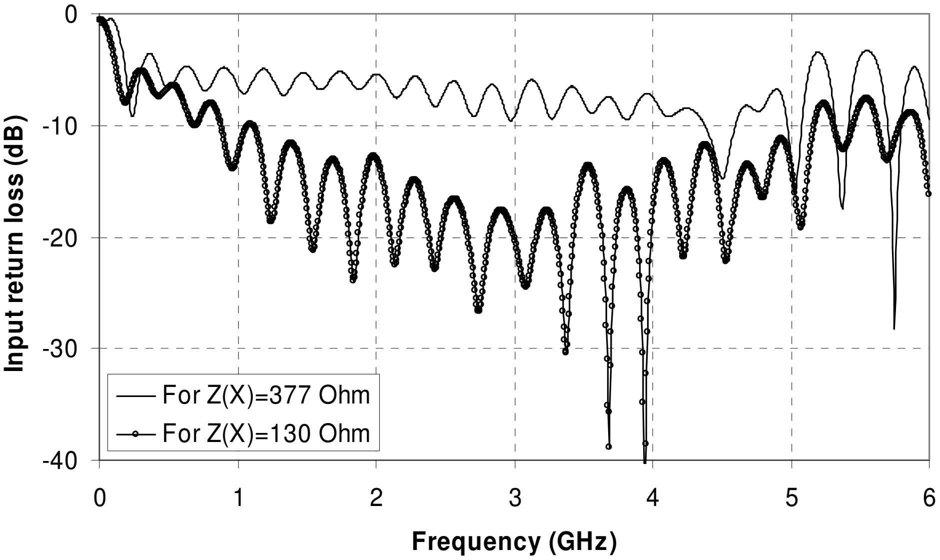

Fig. 5.4. EM simulation results for the input return loss of the designed microstrip quasi-horn antennas shown in Fig. 5.3.

Time domain reflection results are shown in Fig. 5.5, representing the reflected signal across the entire antenna structure for the input monocycle pulse signal with pulse duration 400 ps. This result indicates that significant reduction in input reflection at the open end of the antenna aperture can be achieved for the design of Z(X)=130 Ω.

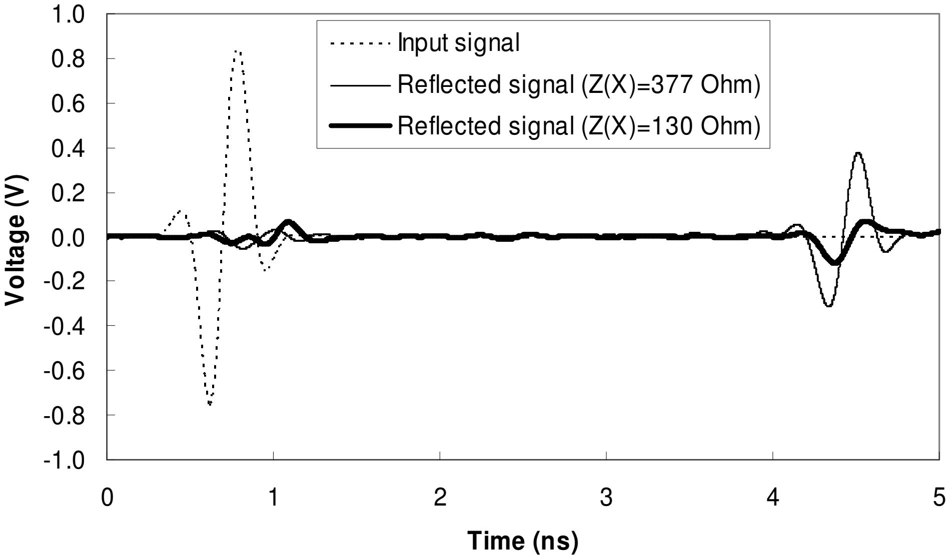

Fig. 5.5. Time-domain EM simulation results for the input reflection of the microstrip quasi-horn antennas with respect to the incident 400-ps monocycle pulse signal.

Fig. 5.6 shows the simulated result of the antenna gain for the design of Z(X)=130 Ω. These results indicate that the maximum antenna gain is more than 10 dB for our interesting center frequency of 2.5 GHz, which is about the center frequency of a 450 ps pulse signal.

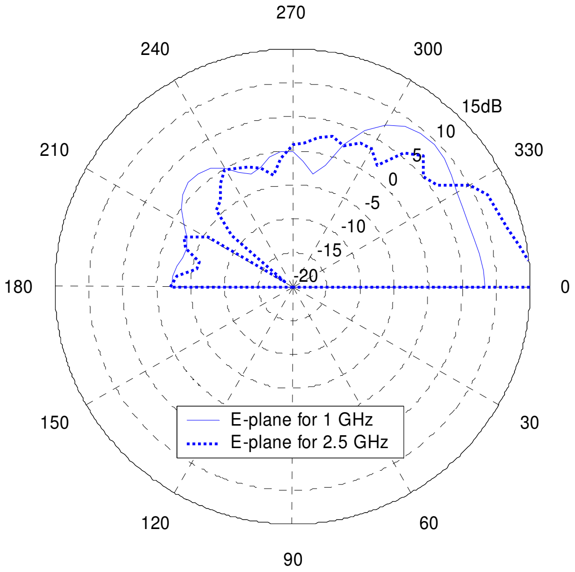

(a)

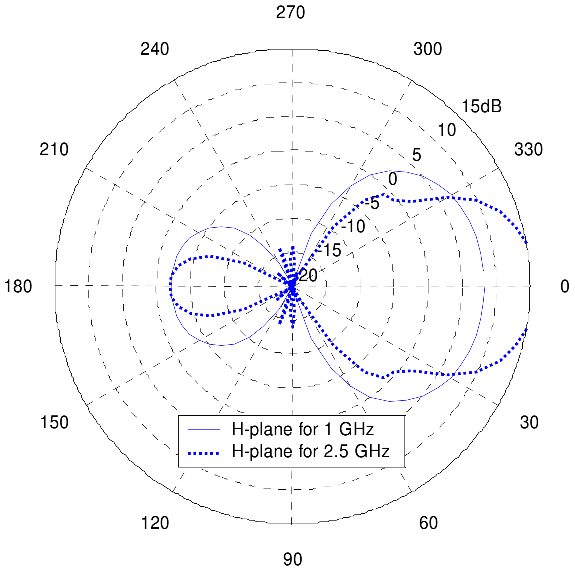

(b)

Fig. 5.6. Antenna pattern simulation results for the designed antenna with Z(X)=130 Ω shown in Fig. 5.3(b); (a) E-plane patterns, and (b) H-plane patterns for the frequencies 1 and 2.5 GHz.

As a final result of the simulations, Fig. 5.7 shows the radiated electric field intensity, which is computed in the simulation package, at a distance of 10-cm from the input feeding of the antenna and in boresight direction (θ=0, ϕ=0), for the input excitation signal of 400-ps monocycle pulse. The radiated field waveform shown in Fig. 5.7 is the first derivative of the monocycle pulse signal, which is the well known phenomenon for a TEM horn antenna verified by Theodorou in theory and measurement. The simulation result in Fig. 5.7 indicates that the antenna design using Z(X)=130 Ω produces a radiating pulse signal with good waveform shape (having low side-lobe ringing) and higher radiation power.

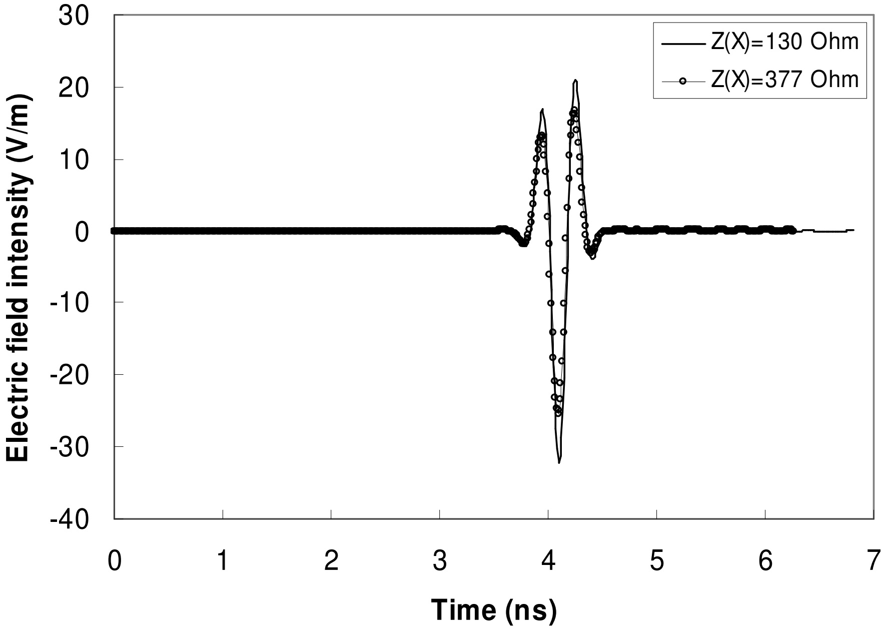

Fig. 5.7. Simulation results of the radiated field intensity in time domain for the designed microstrip quasi-horn antennas shown in Fig. 5.3 with respect to a 400-ps monocycle excitation pulse signal.

From these simulation results, we can conclude that the optimum design of the quasi horn antenna for our application is the design shown in Table 5.1 and Fig. 5.3 using the terminating impedance Z(X)=130 Ω.

B. Fabrication and Performance of the Designed Antenna

I fabricated the microstrip quasi horn antenna based on the optimized design result. Fig. 5.8 shows the fabricated quasi horn antenna with basically the same structure as the one in Fig. 5.3(b); however, the fabricated one uses an absorber covering the top conductor of the antenna.

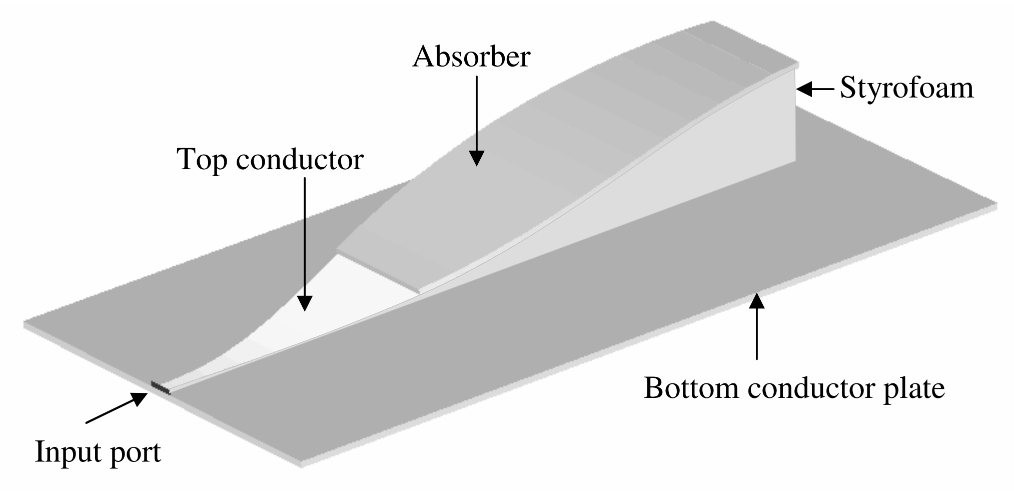

Fig. 5.8. Structure of the fabricated microstrip quasi-horn antenna.

The absorber used here is the laminated radar absorber, AEL-0.375 manufactured by Advanced Electromagnetics. The technique using the absorber in the design of the antenna has often been used to control the beam pattern of the antenna [80]. By using the absorber in our design, we could obtain some improvement in the performance of the input matching and the antenna gain.

Fig. 5.9 shows the measurement result for the input return loss of the designed antenna using network analyzer. This result shows the benefit of using an absorber in the antenna input matching, and especially for a low frequency range below 1 GHz, the improvement is noticeable. The measurement results indicate that the designed antenna with the absorber supports at least 2:1 input VSWR for a frequency range of 0.5 to 6 GHz.

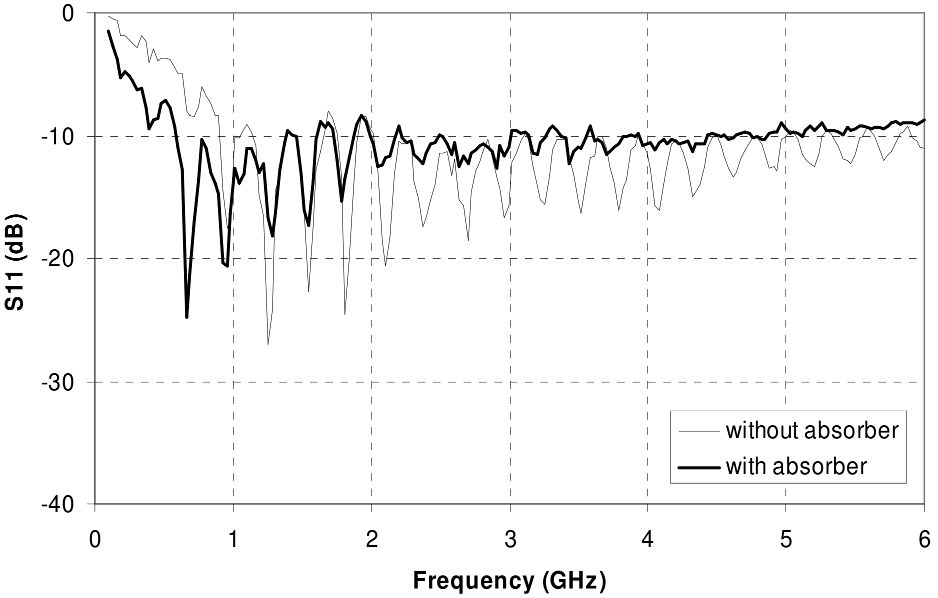

Fig. 5.9. Input return loss measurement results for the fabricated quasi-horn antenna.

We are more interested in the time-domain performance of input matching with respect to the short pulse input. Fig. 5.10 shows the system block diagram used to measure the time-domain waveform of the reflected pulse signal from the antenna for the input pulse signal. The transmitter represented in Fig. 5.10 is the designed one introduced in the previous chapter for the generation of a monocycle pulse. This measurement system enables us to measure the reflected signal for wideband excitation signal covering up to 12 GHz, which is the upper limiting frequency of the digitizing oscilloscope, whereas it requires an extra calibration process to measure the reflected signal from the antenna. The reason for requiring extra calibration is obvious from the system diagram of Fig. 5.10, in which the reflected signal toward the oscilloscope undergoes 6 dB of additional power loss through the resistive power divider compared to the transmitter output signal. The additional loss can be calibrated by separating the reflected signal portion from the recorded overall signal in the oscilloscope and then multiplying it by 2.

Fig. 5.11 shows the measured waveform of the pulse input to the designed antenna, that is the transmitter output, and the reflected pulses from the antenna after calibration. The reflected signal shows two main reflections from the input port of the antenna and the open end. The voltage amplitudes of the main reflections are comparable with the side-lobe ringing of the transmitting pulse, which implies an acceptable performance for the input matching.

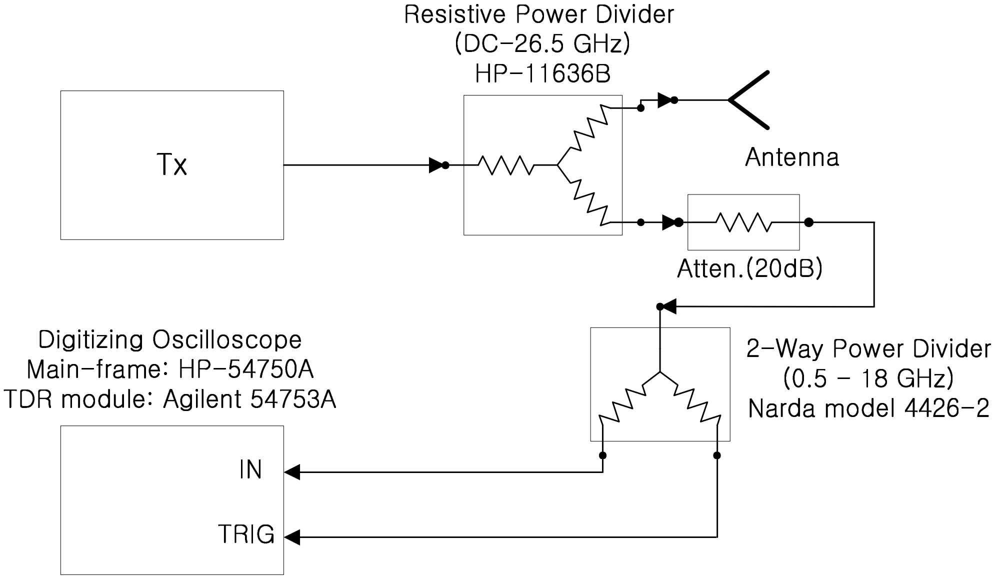

Fig. 5.10. System block diagram for the time domain measurement of the input reflected signal from the designed antenna.

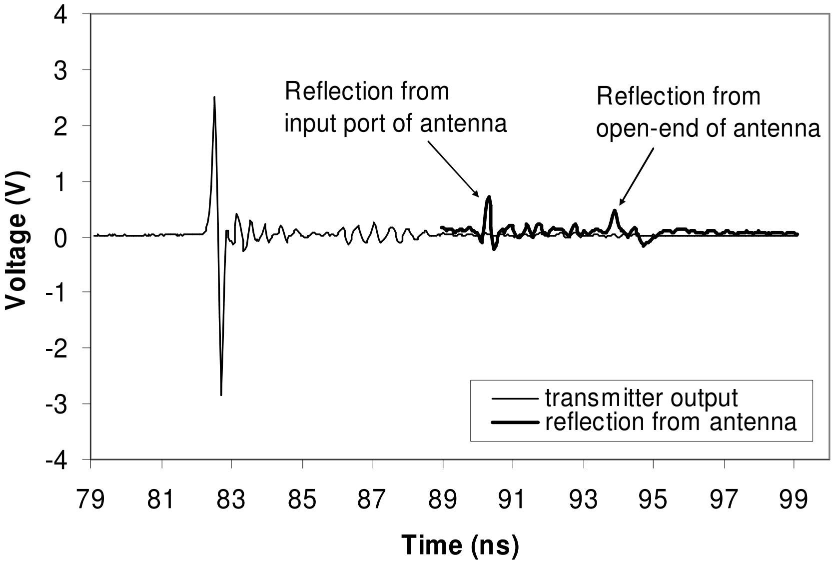

Fig. 5.11. Time-domain input-reflection measurement results.

Another important performance parameter, the antenna gain, was measured for the designed antenna. The antenna gain measurement results are shown in Fig. 5.12 to 5.14. These measurements were done in the antenna chamber room. I have only measured the radiation patterns for 2.65 GHz and 4 GHz because of the absence of the standard horn antenna in our antenna measurement facility; but the results are enough to show the typical performance of the designed antenna. The measurement results show both design cases, with absorber and without absorber, for comparison. As seen from Fig. 5.12 to 5.14, use of an absorber in the antenna results in increased antenna gain especially for higher frequency band, causing the radiation pattern to have a single main-lobe and the main beam axis to 5° in E-plane.

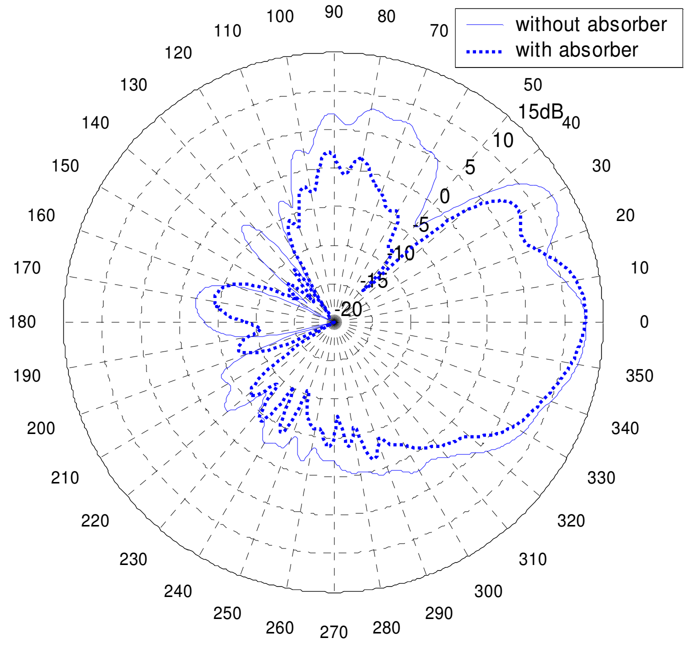

Fig. 5.12. E-plane radiation patterns of the fabricated quasi-horn antenna for 2.65 GHz.

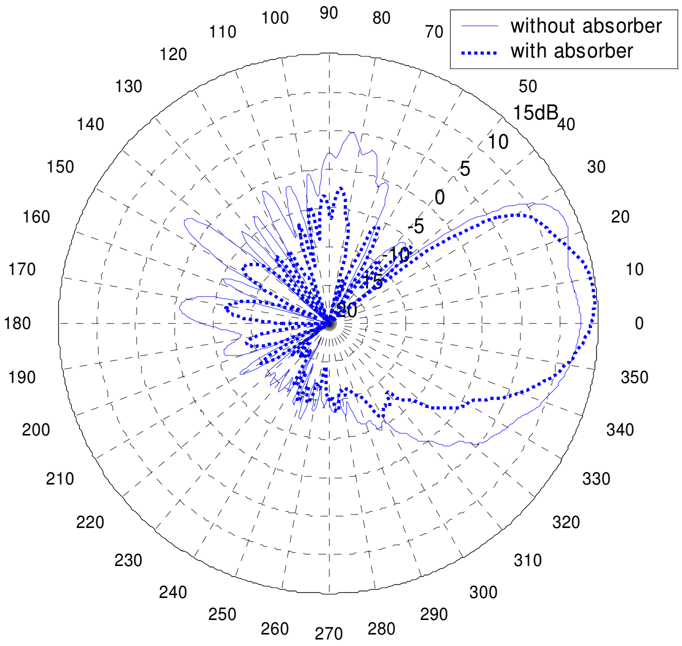

Fig. 5.13 E-plane radiation patterns of the fabricated quasi-horn antenna for 4 GHz.

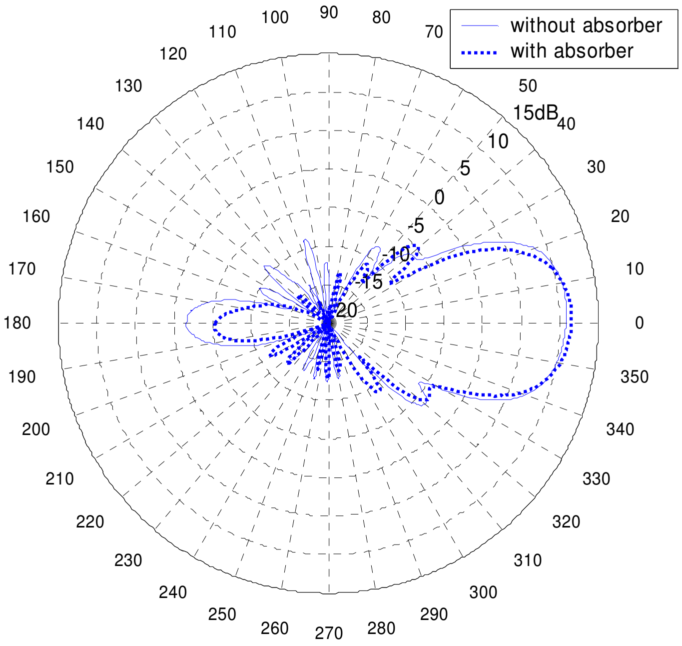

Fig. 5.14. H-plane radiation patterns of the fabricated quasi-horn antenna for 2.65 GHz.

Finally, I measured the overall performance of the fabricated antenna through a direct pulse transmission test. Fig. 5.15 shows the measurement system block diagram for the test. The transmitting and receiving antennas with the same structure face each other and are set apart at a distance of 4-ft 3-in. The designed transmitter and the same resistive power divider and oscilloscope as shown in Fig. 5.10 are used here.

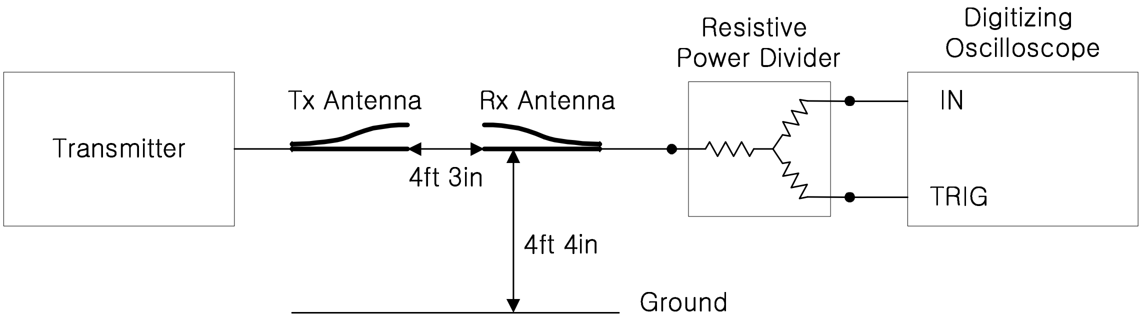

Fig. 5.15. System block diagram for the direct pulse transmission test.

Fig. 5.16 shows the received pulse signals through the antennas for four different transmitting monocycle pulses with different pulse durations, which are generated from the designed tunable monocycle pulse generator. All received waveforms follow the expected receiving waveform shape that is the first derivative of the monocycle pulse as shown in Fig. 5.7. There is no serious distortion in the received waveforms and almost no ringing except the small ringing in the transmitter output already discussed. A spurious signal can be observed in each of the received waveforms after around 10 ns from the main pulse, which is considered as a clutter signal from surrounding structures because this measurement was carried out in an indoor environment. One more factor to be noticed is that the maximum beam axis for the pulse signal was also identified as approximately 5° through this experiment, which is coincident with the results of the antenna gain measurement.

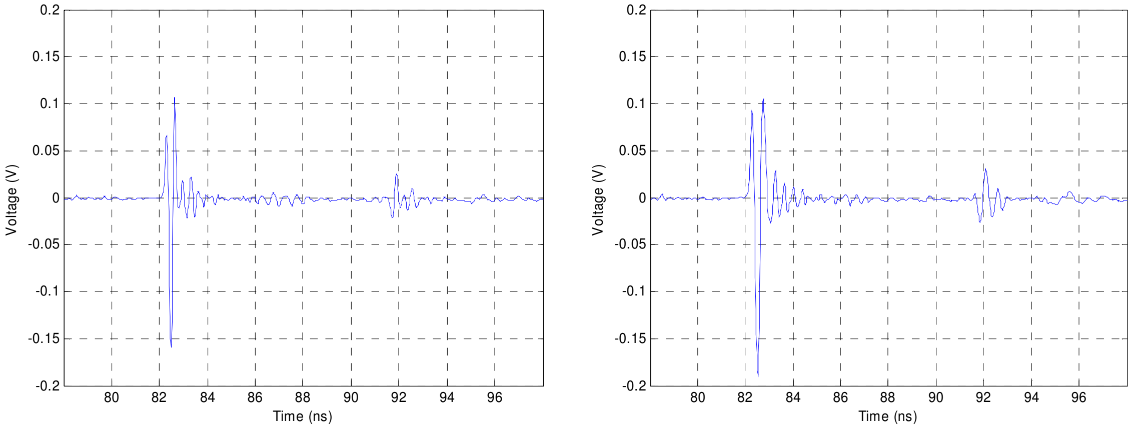

(a) for 450-ps pulse duration

(b) for 660-ps pulse duration

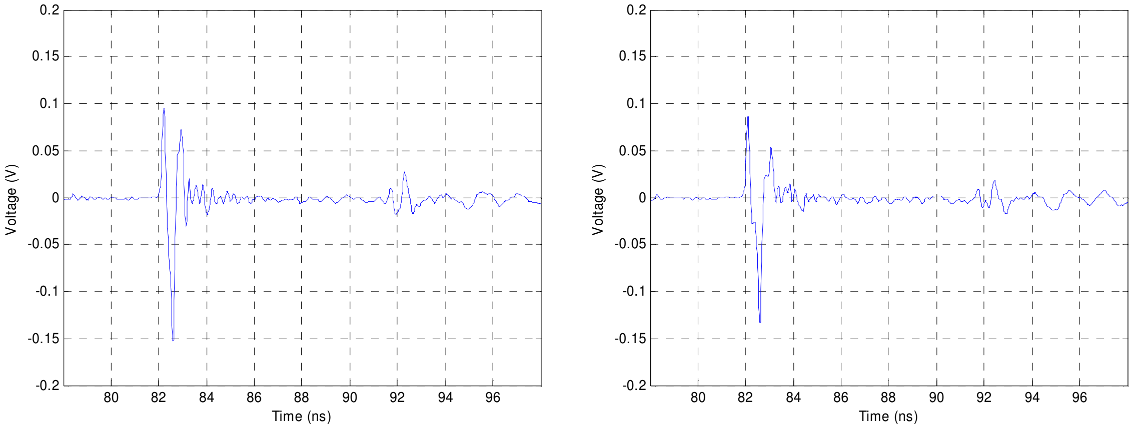

(c) for 850-ps pulse duration

(d) for 1170-ps pulse duration

Fig. 5.16. Measured received-signals through direct pulse transmission test for four different transmitting monocycle pulses with different pulse durations.

The received pulse amplitudes of Fig. 5.16 are considered as reasonable results by comparison with the calculated result of the receiving pulse amplitude. The estimation of the receiving pulse amplitude is made possible by simply using the well known signal transmission equation [18],

$$P_r = P_t \frac{G_r G_t \lambda^2}{(4\pi R)^2} = P_t \frac{G^2 \lambda^2}{(4\pi R)^2} \tag{5.8}$$

where P_r is the available power at the receiver, P_t is the available power from the transmitter, λ is the wavelength at a certain frequency, R is the distance between transmitting and receiving antenna, and both G_t and G_r represent antenna gains for transmitting and receiving respectively, especially in our case $G_t=G_r=G$. The typical antenna gain of the TEM horn antenna, 10 dB [3], was used in the calculation to take into account the wideband pulse signal even though the measured designed antenna gain at 2.65 GHz is about 12 dB. For 450 ps pulse duration, the transmitter output pulse amplitude is 5.8 V_{p-p}, which corresponds to 336 mW of RMS power level. Considering the center frequency as 2.65 GHz, the wavelength λ=4.45 in. Using (5.8) and R being 4-ft 3-in, the calculated available power at the receiver is 1.59 mW, which corresponds to 2 dBm. Including 1 dB of impedance mismatching loss per antenna and also 1 dB of antenna radiation efficiency per antenna, the received power turns out to be -2 dBm, which corresponds to the 251 mV_{p-p} amplitude of the received pulse. This calculation result is almost the same as the measurement result.

Summarizing the measurement results for the fabricated antenna, the performance of the designed antenna can be represented as shown in Table 5.2.

Table 5.2. Summarized performance of the designed quasi-horn antenna.

Input VSWR (for 0.5 to 6 GHz)	2:1
Input return loss (measured in time-domain)	13 dB
Antenna gain (for CW signal)	12 dB @ 2.65 GHz 15 dB @ 4 GHz
Antenna gain (for pulse signal)	10 dB
Main beam axis (for pulse signal)	θ=5°, ϕ=0°
Transfer function of the transmitting antenna	First derivative of the input pulse current waveform
Transfer function of the receiving antenna	No distortion
Radiation efficiency of the antenna	1 dB

CHAPTER VI

SYSTEM INTEGRATION AND TEST

Up to now, I have described in detail the design of the microwave circuit and antenna components comprising the impulse radar sensor, which are the transmitter, the receiver, and antennas. These components are integrated to build an impulse radar sensor. Another component of the sensor system that we have not yet discussed is the signal processing unit. The signal processing unit was implemented on a notebook PC using a commercial A/D converter and Labview instrument programming language [87].

The transmitter and the receiver section were constructed first by integrating the transmitter and the receiver circuit with transmitting and receiving antennas, respectively. These two microwave sections were tested before the complete construction of a single radar sensor through a direct-path transmission test to evaluate the performance of those integrated microwave sections. The direct-path transmission test mentioned here is similar to the direct pulse transmission test described in Chapter V, but the designed receiver was used instead of using only the digitizing oscilloscope to test receiver performance after integration with the designed antenna.

The complete microwave module of the impulse radar sensor was constructed by integrating the transmitting and receiving sections into a single physical structure. The important thing to be considered at this stage is the arrangement of the two antennas, which affect the performance of detecting the signal reflected from the target. I made some experiments to find the best arrangement of the antennas supporting higher receiving power and a lower clutter signal level.

The signal processing technique commonly used in the impulse radar system is simple, which is one of merits of the impulse radar system. In this research, a more sophisticated signal processing technique was not investigated because it lies outside the research scope. In our system, the down-converted signal coming out from the receiver is digitized by an ADC (Analog-to-Digital Converter). For the received digital data, simple signal processing, the background subtraction technique, was used to remove direct cross-coupled signal from the transmitting antenna to the receiving antenna. The background subtraction technique is a well-known and crucial technique in detecting a target signal from the modulated input signal by the direct cross-coupling signal [77].

Experiments testing the performance of the completed impulse radar sensor were performed for several different target structures. These experimental results show the validity of the developed impulse radar sensor as a UWB subsurface penetrating radar sensor as well as the usefulness of the designed novel components, the transmitter and the receiver, and the antennas.

A. Direct-Path Transmission Test

This test was done to test the performance of the transmitter and the receiver section, which are the transmitter and the receiver circuit integrated with antennas, respectively. Fig. 6.1 represents the block diagram of the system used for the direct-path transmission test.

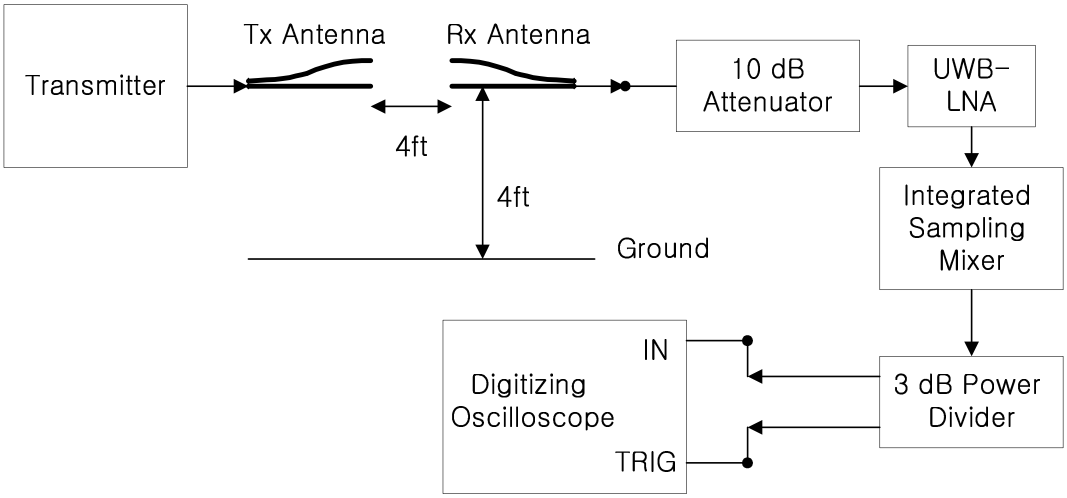

Fig. 6.1. System block diagram for the direct-path transmission test.

We already know that the transmitter and two antennas are working with good performance as examined by the pulse transmission test introduced in the antenna design in Chapter V. Therefore, the main purpose of the test shown here is to determine the performance of the designed receiver including the UWB LNA after it is integrated with the receiving antenna. The UWB LNA will not be used in the final system designed for the pavement assessment application because the LNA is not necessary in such an application using full-power mode for the designed transmitter, and using LNA only causes problems with saturating the sampling mixer. However, it may be useful for other applications that allow using low output power for the transmitter. I tested both of the systems with the LNA and without it, but only the results for the system with LNA are presented here since both results are similar. In the system shown in Fig. 6.1, 10-dB attenuator, 3-dB power divider, and the digitizing oscilloscope are used only for measurement, not as part of the final designed sensor system. The transmitter was operated in full power mode and hence the 10-dB attenuator was used to prevent the sampling mixer from saturating due to the large amplified input pulse from the LNA. The main beam axes of both antennas were matched with each other.

The test was done for four different transmitting pulses with different pulse durations, which are generated from the tunable monocycle pulse generator. The down-converted pulse signals for four different transmitting pulses were recorded in the digitizing oscilloscope and their waveforms are shown in Fig. 6.2. Notice that the unit of the time scale in Fig. 6.2 is 500 us. This time scale of the down-converted signal is predictable as follows. For synchronous sampling, two reference clock oscillators are used in the transmitter and the receiver, respectively. The deviation in frequency between two clock oscillators is about 10 ppm, which corresponds to 100 Hz for a reference frequency of 10 MHz. As (4.7) in Chapter IV implies, a single pulse repetition period of the transmitting signal, 100 ns, is transformed into 10 ms in the time scale of its down-converted signal. Therefore, 1 ns of the pulse duration in the transmitting signal corresponds to 100 us in down-converted signal. The time transformation can be seen more easily in Fig 6.2(c), where the 880 ps pulse duration occupies about a 100 us time span.

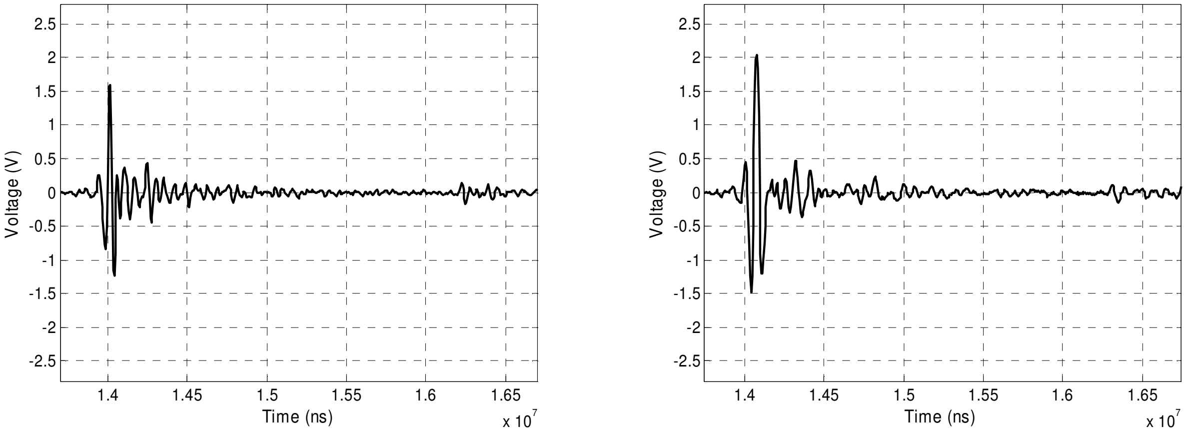

(a) for 450-ps pulse duration

(b) for 600-ps pulse duration

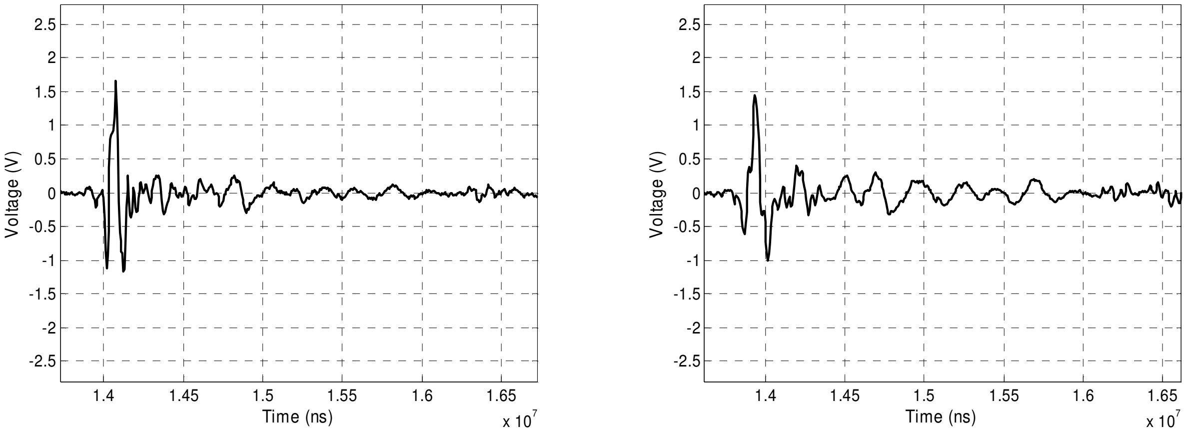

(c) for 880-ps pulse duration

(d) for 1170-ps pulse duration

Fig. 6.2. Measured down-converted signals through the direct-path transmission test for four different transmitting monocycle pulses with different pulse durations.

In Fig. 6.2, the main-lobe part of the pulse waveform does not show significant distortion, while there are some ringing signals in the side-lobe of the pulse. These side-lobe ringings are caused by some clutters around the sensor system in indoor environments.

B. System Integration

The overall impulse radar sensor was constructed by integration of the transmitter, the receiver microwave sections, and the signal processing unit. The integrated part of both microwave sections, which is called microwave module for convenience, will be discussed first and then the signal processing unit, especially its processing technique, will be described.

1) Microwave module

The microwave sections are integrated into a single physical structure, the microwave module, using a solid wood frame as shown in Fig. 6.3.

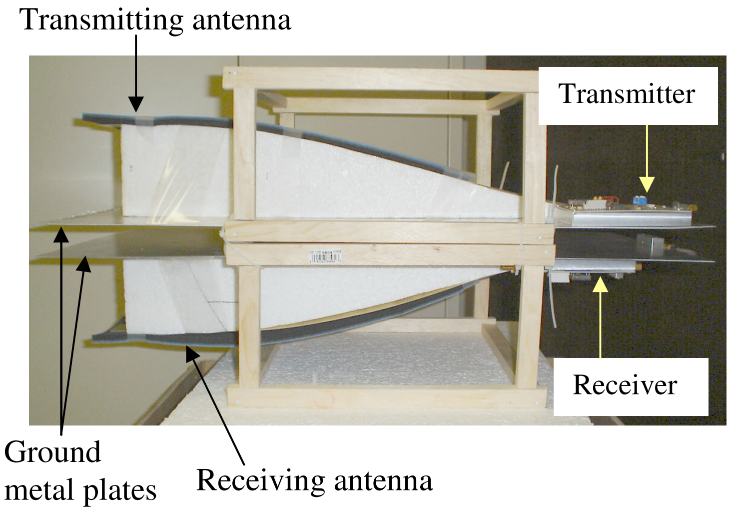

Fig. 6.3. Photograph of the microwave module.

Fig 6.3 shows clearly the benefits of using microstrip quasi horn antennas in view of system integration. The size of the space occupied by the two antennas in longitudinal direction is almost the same as that of a single TEM horn antenna so that the total size of the sensor could be significantly reduced from that of the sensor using TEM horn antennas. Another benefit of using a quasi horn antenna is due to its inherent structure in using a bottom ground metal plate. The ground metal plate provides a good place to hook up the transmitter and the receiver circuit with antennas, as shown in Fig. 6.3. Usability of the ground metal plate of the antenna may reduce the integration cost and the total size of the sensor.

An important factor in combining the transmitter and the receiver microwave sections is the arrangement of the two antennas. Fig. 6.4 shows two possible arrangements of the antennas, where the MBA (Main Beam Axis) of the antenna was measured as 5° in θ-axis in Chapter V. The arrangement in Fig. 6.4(a) is for both MBAs of two antennas to be matched with each other. This arrangement may result in maximized return signal power from the target while cross-coupling between two antennas is increased. The other arrangement in Fig. 6.4(b) shows the same structure as that used in the final microwave module shown in Fig. 6.3. In this arrangement, the MBAs of both antennas are deviated a little from each other but a great deal of decreased cross-coupling may be obtained. When using the background subtraction technique in the signal processing, I found in experiments that the cross-coupled signal may often produce spurious signal detection and an increase in the false alarm rate. To reduce this spurious signal detection caused by the cross-coupling signal, the arrangement shown in Fig. 6.4(b) is recommended for the final system.

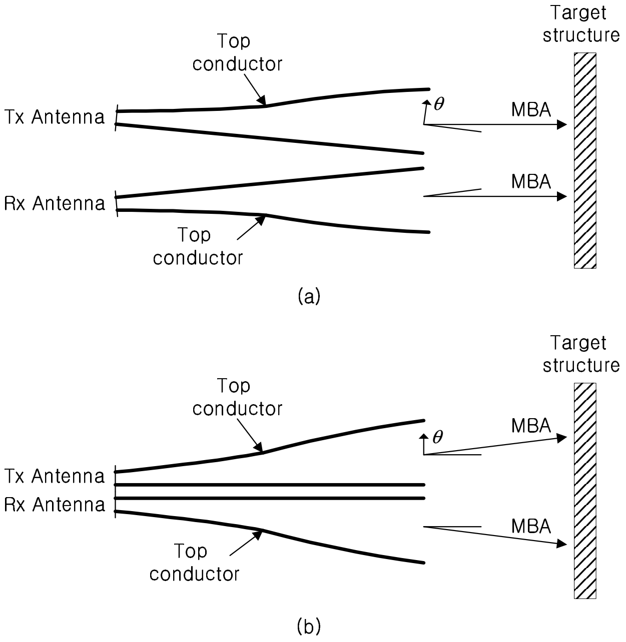

Fig. 6.4. Illustration of two possible antenna arrangements to achieve matching of MBA (Maximum Beam Axis) between two antennas (a) and to reduce cross coupling (b).

The completed microwave module was packaged inside a paper box as shown in Fig. 6.5. Fig. 6.5(a) shows how the microwave module is placed inside the box and Fig. 6.5(b) shows the microwave module completely packaged by covering the top of the box for protecting the circuits from physical damage. The external lines shown in Fig. 6.5(a) are for the DC bias of circuits and output down-converted signal.

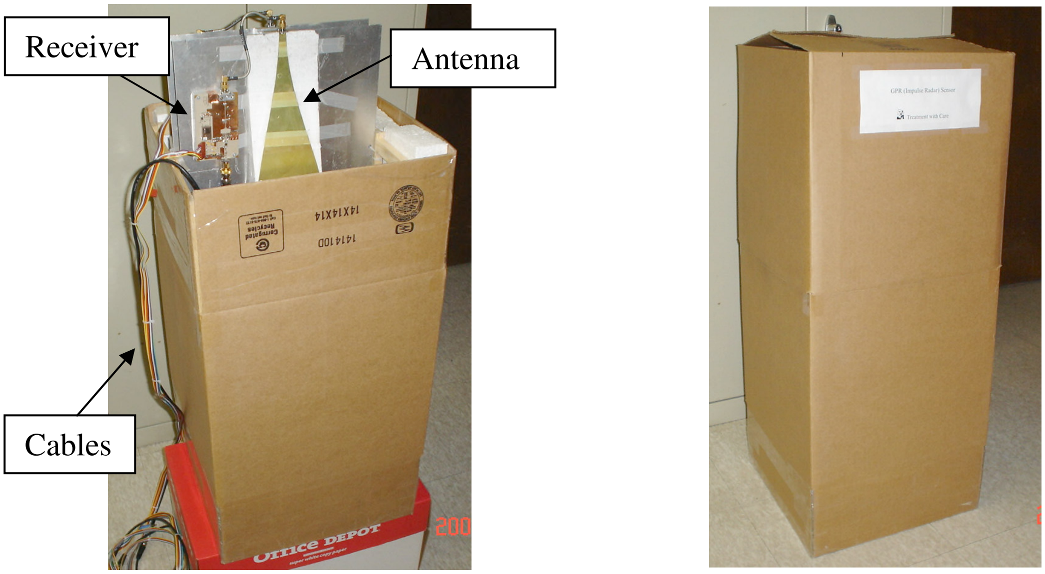

(a) (b)

Fig. 6.5. Photograph of the microwave module packaged inside a box after removing the top cover of the box (a) and with the top cover (b).

2) Signal processing

Signal processing is required to digitize the signal down-converted by the receiver, to visualize the digitized data, and to detect the target signal from background noise or clutter signals. The signal processor was implemented on a notebook PC using Labview instrumentation programming language. The Labview software package provides a convenient environment to build the ADC (Analog-to-Digital Conversion), signal processing and a variety of display formats.

ADC was implemented by using the data acquisition (DAQ) card, DAQCard-6036E manufactured by National Instrument, and Labview programming. The data length of each digitized sample supported by the DAQ card is 16 bits, from which the dynamic range of ADC can be calculated as 20log(2^{16})=96 dB. This dynamic range is much higher than the 50 dB of the sampling mixer's dynamic range, and hence the quantization error induced by ADC is negligible. The sampling rate for the input down-converted signal is set up as 220 KHz according to the design parameter of the synchronous sampling receiver derived in Chapter IV.

The digitized receiving data includes a relatively high level of background cross-coupling signal, which is directly coupled from the transmitting antenna. Without removing this background cross-coupled signal (or background signal), it is hard to identify the signal reflected from the target, which is the amplitude modulated by the background signal. The background subtraction technique is a well-known method in the impulse radar technology to detect an interesting signal. This technique, a kind of a demodulation process, consists simply of first recording the background signal as a reference and then subtracting the reference from the real measurement signal (or real signal) for the target structure. Assuming the reference is the same as the background signal included in the real signal, there remains only the reflected signal from the target after the subtraction. The background subtraction method is simple but has the fatal drawback of producing spurious detected signals if the background signal included in both the reference and the real signal are not identical. A method will be introduced to overcome this problem. The background signal was measured and recorded after setting the antenna boresight direction to the open space since it should not include any reflected signals apart from the direct cross-coupling signal. Therefore, the background signal does not need to be measured every time the real measurement is carried out; usually, a single accurate measurement of the background signal is enough.

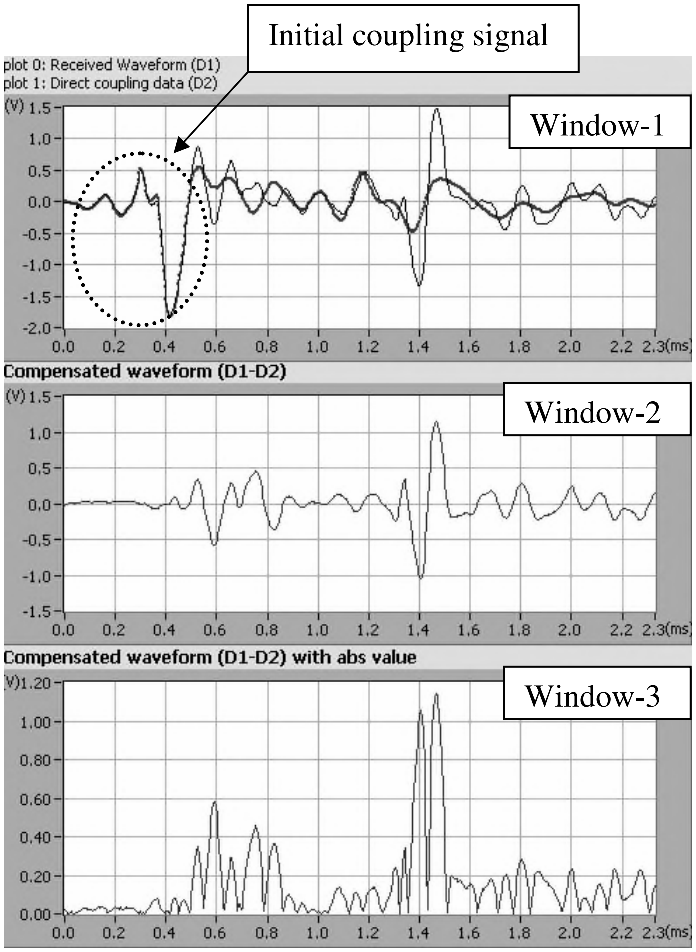

Fig. 6.6. Display window of the signal processing to detect the target reflected signal using background subtraction technique.

Fig. 6.6 shows a display window of the signal processing, programmed by Labview, to detect the target reflected signal by means of the background subtraction technique. The display window includes 3 sub-windows, each of which shows different data according to the processing steps. Window-1 in Fig. 6.6 represents two signals, one is the reference signal depicted as a thick line and the other is the real signal depicted as a thin line.

The data shown in Window-1 plays a very important role in the detection of the target reflected signal. As indicated in Window-1, each of the reference signal and the real signal has a section partially matched with the other in their entire waveform, which is called the initial coupling signal. There is an initial coupling signal in all measurements because this part of the waveform appears due to the initial coupling of the transmitting signal into the receiving antenna and is not affected by whether the target structure is present or not. The initial coupling signal can be used as a pilot signal in synchronization because it can be an indicator of the matching status of two background signals included in the reference and the real signal. If both initial coupling signal parts are not matched exactly, indicating that both the background signal in the reference and the real signal are not identical any more, then the subtraction process may produce significant spurious signals after subtraction and may generate false alarms. To maintain matched initial coupling signals, the DAQ (or ADC) parameters such as the trigger slope and the trigger level should be maintained when measurements are carried out to obtain the reference signal and the real signal. Even though the DAQ parameters are maintained, mismatching of the initial coupling signals can occur because of the frequency variation in the reference clock oscillators. Small frequency modulation in the reference clock oscillator causes the down-converted signal to be stretched or shrunken in time scale, which is a frequency modulation effect on the down-converted signal. If this frequency modulation effect occurs in real signal measurement after recording the reference signal, there will be significant mismatch between two background signals in the reference and the real signals. To compensate this mismatch between background signals, the control voltage of the VC-TCXO should be adjusted to compensate the frequency modulation effect. By monitoring the pilot signal, which is the initial coupling signal, we can detect the frequency modulation effect on the down-converted signal and compensate it by adjusting the control voltage of the VC-TCXO. However, monitoring of the matching status in the short time interval of the initial coupling signal is very difficult and impractical because an insensible mismatch in the initial coupling signals could cause significant errors in the subtraction process. To overcome this monitoring problem, a revised monitoring method was used. Fig. 6.7 shows a simplified schematic representation of the problem in the monitoring of the matching status of the initial coupling signals. In Fig. 6.7, the pulse signals represented as a solid line is the initial coupling signal of the reference signal, and another pulse signal represented as a dotted line is the initial coupling signal of the real signal. One cycle of pulse signals with a standard clock period T_c is presented here. In ideal conditions, there is a time interval of a standard clock period T_c between two peak pulses for each signal. In other words, for the ideal matched condition of initial coupling signals, there is no frequency modulation in the reference clock so that the standard clock period T_c is maintained and the real signal coincides perfectly with the reference signal. However, if frequency modulation occurs, the situation depicted in Fig. 6.7 can appear, and the initial coupling pulses are not matched. As shown in Fig. 6.7, the deviation between the reference and the real signals is as small as Δt_1 in trigger position, which is the same situation as in Window-1 in Fig. 6.6. On the other hand, after one cycle of the clock, the amount of deviation Δt_2 is much larger than Δt_1, which means that monitoring of matching status in a single clock period after the trigger position can easily identify small mismatching that may not be detected at the trigger position.

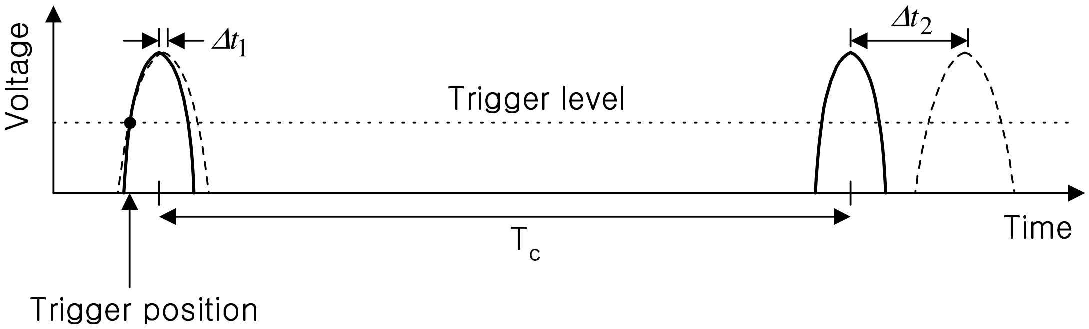

Fig. 6.7. Illustration of the monitoring problem in obtaining matching of the initial coupling signals included in the reference and the real signal.

Using this revised monitoring method, we can detect minor deviation in the background signals to be subtracted, compensate the frequency modulation of the clock oscillator by adjusting its control voltage, and eventually obtain accurate reflected signals from the target only by background subtraction.

Returning now to Fig. 6.6, Window-2 represents the resulting data of background subtraction. This is a general A-scope display format of a radar system, and most of the subsurface penetrating radars have commonly used it for target signal detection. The data in Window-3 is simply the absolute value of the data in Window-2. Comparing the data in Window-2 and Window-3, we see that the data in Window-3 alleviates some visual ambiguity in identifying target reflected signal from background clutter signals because the data of Window-3 has a single polarity rather than the dual polarity of the Window-2 data. The data format in Window-3 enables us not only to enhance signal detectability but also to create the B-scan data format, which will be shown below.

In practical applications of the impulse radar such as pavement assessment, the B-scan data format shown in Fig. 6.8 is commonly used to detect target signatures reflected from layer interfaces and to visualize the internal structure of the illuminated target structure. The horizontal axis of the plot represents depth information from the end of the antenna aperture and the vertical axis represents number of scans, where a scan is defined as a measurement with selected pulse duration and at a certain location on the target structure. If the sensor is moving for measurements over the target structure, the scan number corresponds to the displacement of the moving sensor with respect to a certain reference position on the target structure. The intensity level represents the amplitude of the detection data, defined as the amplitude level obtained from Window-3 of the detection program in Fig. 6.6. In Fig. 6.8, a darker intensity level represents higher amplitude of the returned signal, which is more likely to be a target reflected signal. Using the B-scan format, multiple scan data can be gathered into a single format and help us visualize the overall scan information. Especially, with the impulse radar having multiple frequency bands such as the designed system in this research, the B-scan format is unavoidable in comparing all the detection data obtained from multiple frequency bands.

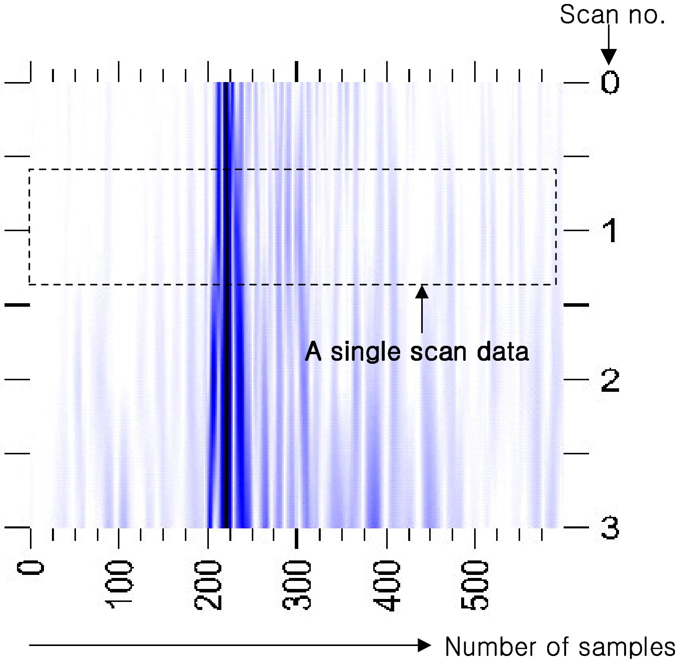

Fig. 6.8. Display format of the B-scan data format. The horizontal axis represents the number of samples (The time interval between two adjacent samples is the sampling interval, which is an inverse of the sampling rate of ADC). The vertical axis represents the number of scans.

C. Test and Evaluation of the System

The complete impulse radar system developed in this research was tested for some sample target structures. I first tested for some simple structures arbitrarily chosen to evaluate the performance of the system in terms of the radiating waveform shape, detectability of layer interfaces, detection range, and range resolution. Finally, I tested the developed system for a pavement sample structure constructed for the test of the subsurface penetrating radar sensors. The objective of these tests is to show the validity of the designed system as a subsurface penetrating radar sensor. These test results also reflect the fact that the newly-designed components such as the tunable transmitter, the integrated sampling mixer, and the quasi-horn antenna are useful in the development of an impulse radar system.

1) Test for a metal plate

The metal plate is a perfect reflector for the electromagnetic pulse; thus the test using the metal plate is a rudimentary one for the complete system. For this test, the metal plate is placed on the bottom, and the sensor (specifically the microwave module) is placed 18 in apart from the metal plate in an upper direction and in the center of the metal plate in a horizontal direction. Fig. 6.9 shows the detection data obtained by illuminating four different pulses having different pulse durations with respect to the metal plate. From the results in Fig. 6.9, we can see that not all detected waveforms for different transmitting pulses have severe distortion in the main-lobe or serious ringing in the side-lobe, except for the1170-ps transmitting pulse. The detection data for the 1170-ps pulse shows large ringing in the side-lobe caused by multiple reflections from surrounding clutter. This means that the designed antenna has too large a beam width for a 1170-ps pulse to focus on a spot on the object. The need for more optimization of the antenna for 1170-ps pulse is clear from this result.

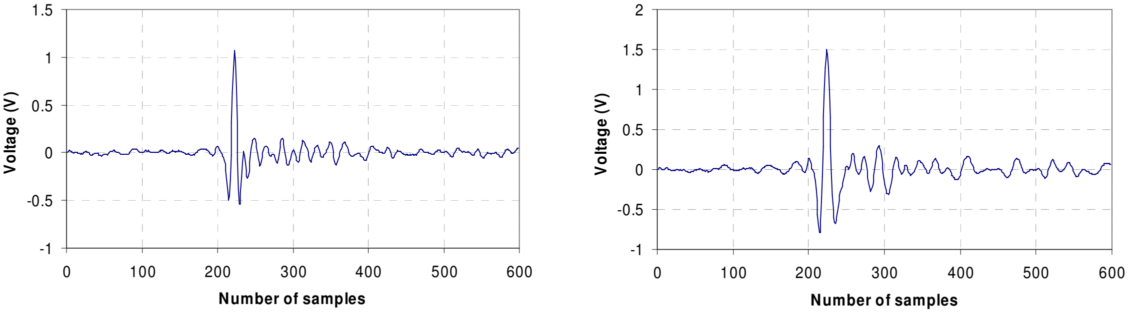

(a) for 450-ps pulse duration

(b) for 600-ps pulse duration

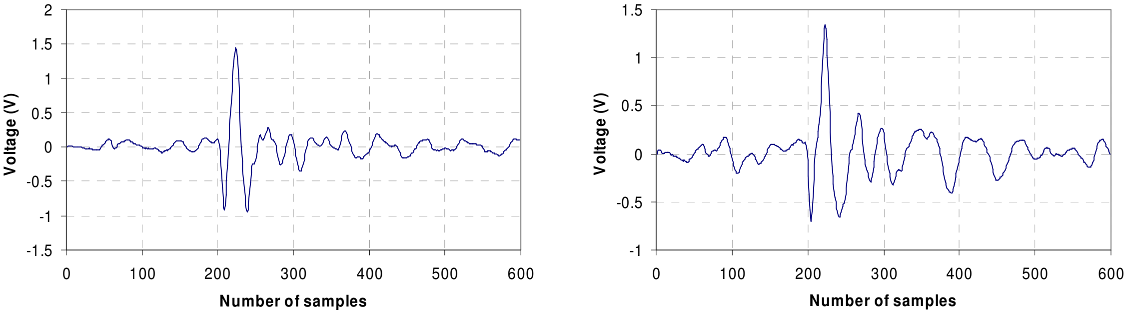

(c) for 880-ps pulse duration

(d) for 1170-ps pulse duration

Fig. 6.9. Detection results for a metal plate.

Fig. 6.10 shows the B-scan format of the detection data for the metal plate, in which each scan represents the data for a specific transmitting pulse duration with a corresponding instantaneous frequency band.

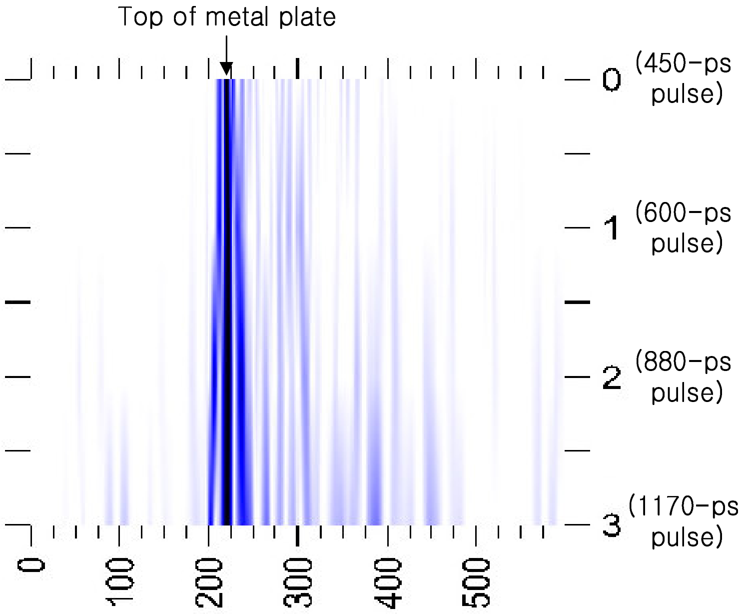

Fig. 6.10. B-scan format result for a metal plate.

2) Test for the sample structures with wood layer

The detection performance of the system was tested for some simple structures with wood layers. Three sample structures were built as shown in Fig. 6.11 to evaluate the detection performance in different situations. The sample structure shown in Fig. 6.11(a), which is called as sample structure A, is to evaluate the detection range-resolution of the system using a thin wood layer with a thickness of about 1 in. The sample structure of Fig. 6.11(b), sample structure B, has a much thicker wood layer than structure A to show the effect of a thick material on detection performance. The sample structure of Fig. 6.11(c), sample structure C, has an embedded wood layer to show detection results for a more complex multilayer structure. In all measurements, the sensor was placed on the top of the upper first layer with a downward illuminating direction. Notice that the

Styrofoam has a relative dielectric constant almost identical to that of air. Wood is known to have a very wide range of dielectric constant, 1.2 to 5, and loss tangent value, 0.004 to 0.4167.

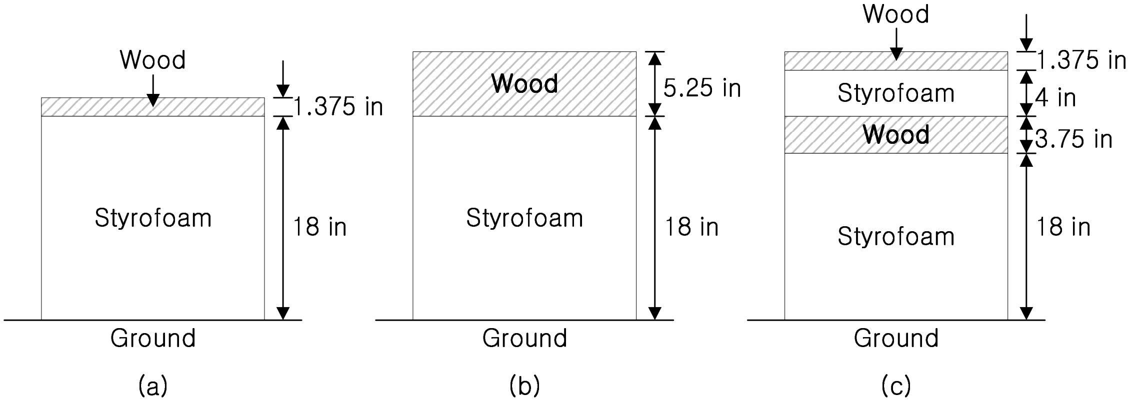

Fig. 6.11. Architecture of three sample structures with wood layers built for the system test. (a) sample structure A, (b) sample structure B, and (c) sample structure C.

Fig. 6.12 shows the detection data result for sample structure A in the B-scan format to display all data for different frequency bands at the same time. As indicated in Fig. 6.12, three interfaces between layers are clearly detected, which are the air-wood interface (or the top of wood), the wood-Styrofoam interface (or the bottom of wood), and the Styrofoam-ground interface (or the top of the ground). From the results in Fig. 6.12, we find that a 450 ps pulse duration can definitely support about 1-in of the range resolution, as we expected. For 600 and 880-ps pulse durations, the system can unexpectedly detect the bottom of the wood, which means that it can also support about 1-in of the range resolution. The reason of this unexpectedly finer range resolution for relatively large pulse durations will be explained below in detail.

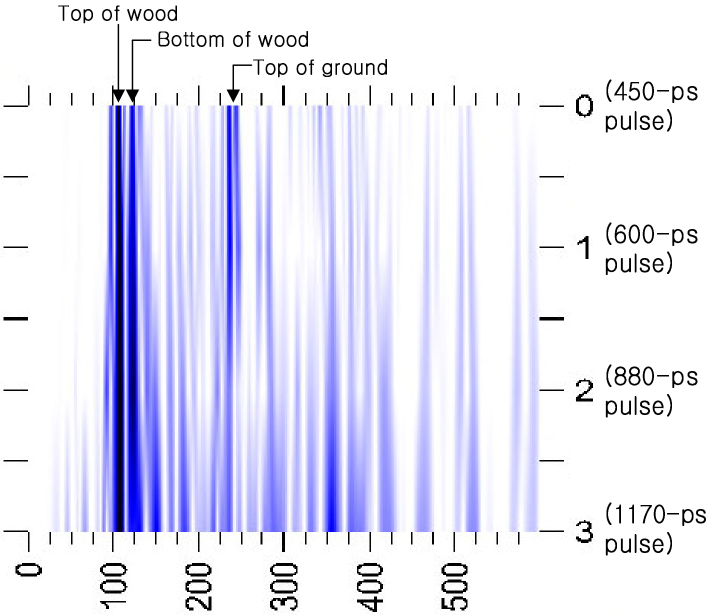

Fig. 6.12. B-scan format of the detection result for sample structure A.

Fig. 6.13 shows the detection data results for sample structure B. As indicated in the figure, the system clearly detects the 2nd and 3rd interfaces, which are at the bottom of the wood layer and on top of the ground. However, we may observe that a clutter signal between the 2nd and 3rd interface reflected signals. From this result we may realize that the target structure having a layer greater than 5-in in thickness may produce some internal clutter signals. However, in the case of 450 and 600-ps pulse durations, the clutter signal is relatively much weaker than the target signals from interfaces.

Fig. 6.14 shows the detection results for sample structure C. As in previous cases, it shows clear detection of all interfaces between layers and also the clutter signal between the 4th and 5th interface reflected signals. From the experiments for these different types of sample structures, we may find that 450- and 600-ps pulse duration is more useful than others because those shorter duration pulses may support higher range resolution and reduced clutter signals. Between two shorter pulse durations, 600-ps may be the best choice to have modest penetration depth and range resolution.

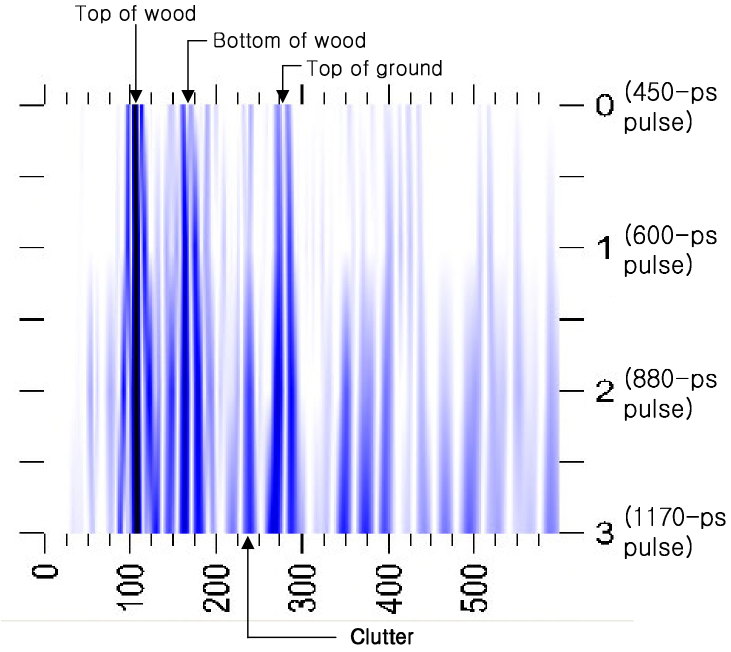

Fig. 6.13. B-scan format of the detection result for sample structure B.

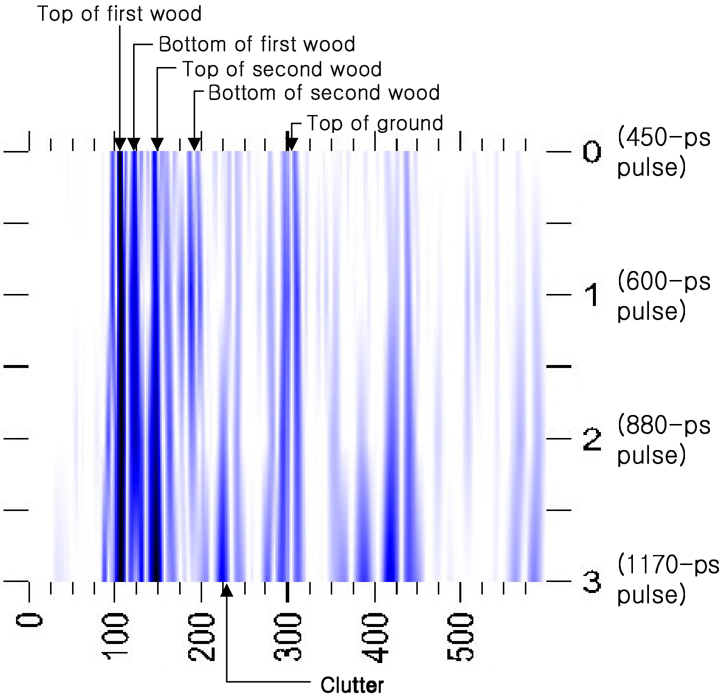

Fig. 6.14. B-scan format of the detection result for sample structure C.

In the detection results of Fig. 6.12 and 6.14, we may realize that the bottom of the first thin wood layer with about 1-in of thickness can be detected by using not only a 450-ps pulse duration, but also 600-ps and 880-ps pulse durations. Considering the estimated minimum pulse duration required to achieve 1-in of range resolution for the asphalt layer detection was 400-ps in Chapter II, the experimental detection results show that even larger pulse duration may obtain 1-in range resolution. The main reason for this discrepancy between estimated and measured range resolution can be found through the actual detection waveform shown in Fig. 2.3. The detected signal in Fig. 2.3 represents two non-overlapped reflected signals from two adjacent interfaces. We may observe that the two reflected signals may still be discernable even when they come closer to each other. This means that the actual range resolution obtainable from the selected pulse duration is higher than the estimated one, based on the assumption of non-overlapped reflected signals, which indicates that the actual range resolution of 600-ps and 880 ps pulse duration is higher than the expected one, and may even detect 1-in thickness.

From these detection results, measurement of the dielectric constant and the thickness of each layer composing a multi-layer structure are possible. The measurement method introduced in [6] is basically used here. For a stratified medium shown in Fig. 2.2, it is straightforward to derive (6.1) representing the relationship between the reflected electric field intensity and the incident one.

$$\frac{E_{rn}}{E_i} = \Gamma_{n(n-1)} \left(\prod_{m=1}^{n-1} T_{m(m-1)} T_{(m-1)m} \; e^{-2\alpha_m d_m} \right) \tag{6.1}$$

where E_{rn} is the reflected electric field intensity from nth layer interface, E_i is the incident electric field intensity on the top of the whole structure as indicated in Fig. 2.2, $\Gamma_{n(n-1)}$ is the reflection coefficient for the incident wave from (n-1)th layer to nth layer, $T_{m(m-1)}$ is the transmission coefficient for the propagating wave from (m-1)th layer to mth layer, α_m and d_m are the attenuation constant and the thickness of the mth layer, repectively. The reflection coefficient for normal incidence can be expressed in terms of intrinsic impedances as,

$$\Gamma_{n(n-1)} = \frac{\eta_n - \eta_{n-1}}{\eta_n + \eta_{n-1}} \tag{6.2}$$

where η_n is the intrinsic impedance of n^th^ layer and it can be approximated as a real number for low-loss and non-magnetic material as,

$$\eta_n \cong \sqrt{\frac{\mu_0}{\varepsilon_0 \varepsilon_{rn}}} \tag{6.3}$$

By substituting (6.3) for (6.2), we may derive an equation for the dielectric constant of n^th^ layer as,

$$\varepsilon_{rn} = \varepsilon_{r(n-1)} \left(\frac{1 - \Gamma_{n(n-1)}}{1 + \Gamma_{n(n-1)}} \right)^2 \tag{6.4}$$

A procedure of calculating the dielectric constant and the thickness of each layer of the target substrate is recursive as shown in Fig. 6.15. For instance, from (6.1), Γ_{10} can be calculated as,

$$\Gamma_{10} = \frac{E_{r1}}{E_i} \tag{6.5}$$

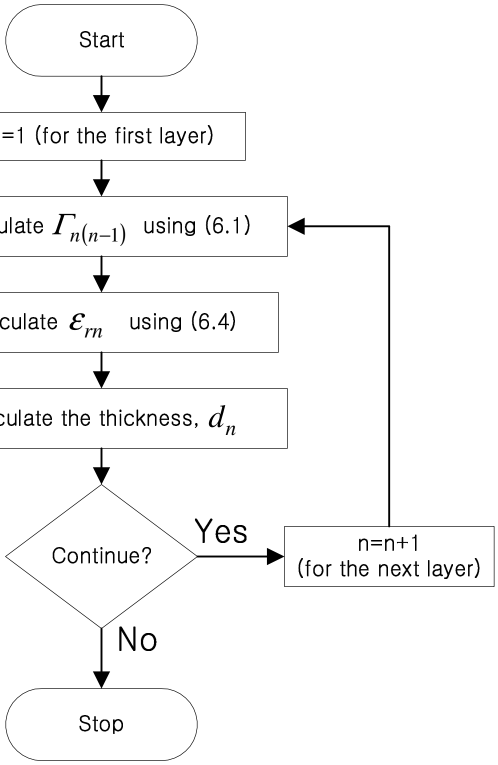

Fig. 6.15. Procedure of calculating the dielectric constant and the thickness of substrate layers.

Notice that if the target substrate is a perfect metal plate, Γ_{10} = E_{r1}/E_i = -1, and hence E_i=-E_{r1}=-E_m, which means E_i can be determined by the amplitude of the reflected signal, E_m, from the metal plate. Therefore, Γ_{10}=-E_{r1}/E_m, which can be calculated by the ratio of two measured voltage amplitudes of the reflected signals: one is from the target structure and the other is from the metal plate. After calculation of ε_{r1}, we may calculate the thickness d_1 using the relationship, d_1=v_pt_0, where v_p is the phase velocity of the wave in the first layer and t_0 is the time interval between two reflected signals from upper and lower layer interface boundaries, which is the theoretical propagation time in the air. Let us define a time interval t_d as a measured time interval in the time scale of down-converted signal. There is a linear relationship between these two time interval values, t_0 and t_d, such that $t_0=t_d \cdot TSF$, where TSF is the time scale-factor. The TSF can be measured by using two reflected signals from a metal plate placed in two different locations. I carried out two measurements for a metal plate placed in two different distance with difference d=1.5-in, and measured t_d=9.04 ms. The theoretical propagation time t_0=d/c=127-ps, where c is the phase velocity in free-space. Therefore, the measured TSF=t_0/t_d=14.0487×10^{-9}. After all, the thickness of n^th layer, d_n, can be obtained by,

$$d_n = v_{pn} t_{0n} = \frac{c}{\sqrt{\varepsilon_{rn}}} \cdot t_{dn} \cdot TSF \tag{6.6}$$

Using (6.1) and the fact $E_i=-E_m$, Γ_{21} can be expressed as,

$$\Gamma_{21} = \frac{\left(-\frac{E_{r2}}{E_m}\right)}{T_{10}\, T_{01}\, e^{-2\alpha_1 d_1}} \tag{6.7}$$

T_{10} and $T_0$1 can be easily determined from Γ_{10} by using the relationship,

$$\begin{aligned} T_{n(n-1)} &= 1 + \Gamma_{n(n-1)} \\ T_{(n-1)n} &= 1 - \Gamma_{n(n-1)} \end{aligned} \tag{6.8}$$

In (6.7), the calculation of $-E_{r2}/E_m$ is similar to the case of $-E_{r1}/E_m$ in Γ_{10} calculation, d_1 is the calculated value in the previous stage and α_1 is the attenuation constant of the first layer in units of Np/in. Notice that this measurement method requires the information for the attenuation constant of each layer to calculate reflection coefficients. In fact, the prerequisite of this method is that we have already known the material type of each layer composing the target structure and its attenuation constant in advance. As shown in the procedure of Fig. 6.15, after calculation of Γ_{21}, we may obtain ε_{r2} and d_2 using (6.4) and (6.6).

Table 6.1. Measurement results for the dielectric constant and the thickness of each layer of sample structure A, B, and C. The assumed value of loss tangent, tanδ, in the table is chosen from known typical values.

		Assumed ε_r	**Measured ε_r**	**Actual thickness**	**Measured thickness**	**Assumed tanδ**	**Assumed α**
Sample structure A	**Layer 1: Wood**	1.2 to 5	**4.0**	1.375	**1.389**	0.1	0.106
	Layer 2: Styrofoam	1.0	**1.16**	18.0	**17.53**	0.0	0.0
Sample sturucture B	**Layer 1: Wood**	1.2 to 5	**4.0**	5.25	**4.7**	0.1	0.106
	Layer 2: Styrofoam	1.0	**1.16**	18.0	**17.2**	0.0	0.0
Sample structure C	**Layer 1: Wood**	1.2 to 5	**4.0**	1.375	**1.43**	0.1	0.106
	Layer 2: Styrofoam	1.0	**1.22**	4.0	**3.52**	0.0	0.0
	Layer 3: Wood	1.2 to 5	**4.47**	3.75	**3.24**	0.1	0.106
	Layer 4: Styrofoam	1.0	**0.9**	18.0	19.2	0.0	0.0

Table 6.1 represents measurement results for the dielectric constant and the thickness of each layer of sample structure A, B and C shown in Fig. 6.11 using the detected signals. Measurement results show the performance of accurate measurement with small error as well as good detection performance of the developed sensor system. Note that in table 6.1, the assumed loss tangent value of wood is chosen from known typical values in the range of 0.004 to 0.4167.

3) Test for the pavement sample structure

Finally, I tested the sensor system for a pavement sample structure. Fig. 6.16 (a) and (b) show the layer structure and the photograph of the pavement sample constructed for the test of a subsurface penetrating radar sensor, respectively. The real pavement structure consists in general of the asphalt, the base, and the sub-base. Here, in the pavement sample, a wood-air (void)-wood structure therefore replaces the sub-base in real situations. This is a reasonable replacement because even in real structures, the air void is occasionally encountered and the detection of the air void is a critical objective in the pavement assessment. Typical values of dielectric constants and other physical values for the asphalt and the base are given in Tables 2.1 and 2.2 of Chapter II.

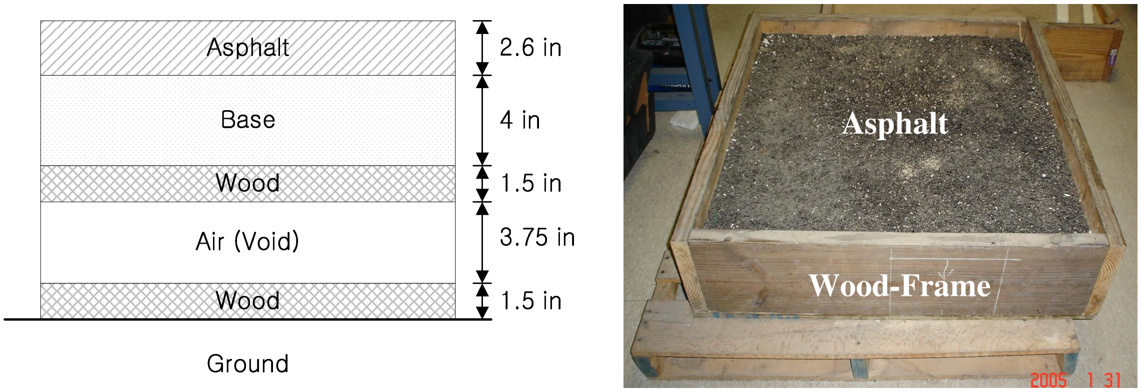

(a) (b)

Fig. 6.16. (a) Architecture of the pavement sample used for the system test. (b) Photograph of the pavement sample structure.

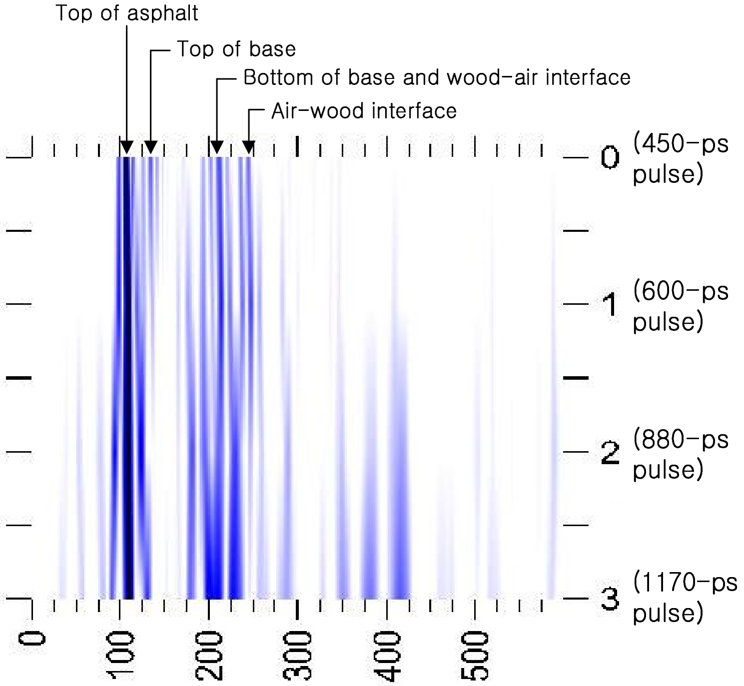

Fig. 6.17. B-scan format of the detection result for the pavement sample structure.

Fig. 6.17 shows the detection results for the pavement sample of Fig. 6.16. In Fig. 6.17, detected signals are reflected from all of the major interfaces, which are the top of the asphalt, the asphalt-base interface (or the top of the base), the bottom of the base and the wood-air interface, and the air-wood interface. The third detected signal reflects that the two interfaces, the bottom of the base, and the wood-air interface, can not be clearly distinguished. It is noticeable that the top of the base is only detected by 450 and 600-ps. pulse. From this result, I was able to conclude that 450 and 600-ps pulses may be the most useful pulse signals for pavement assessment, which is similar to the previous results for the sample structure with wood layers.

Table 6.2. Measurement results for the dielectric constant and the thickness of asphalt and base layer of the pavement sample structure. The assumed value of loss tangent, tanδ, in the table is chosen from known typical values.

	Assumed ε_r	**Measured ε_r**	**Actual thickness**	**Measured thickness**	**Assumed tanδ**	**Assumed α**
Layer 1: Asphalt	5 to 7	**3.72**	2.6	**2.376**	0.004	0.006
Layer 2: Base	8 to 12	**7.0**	4.0	**4.234**		

Table 6.2 represents the measurement results for the dielectric constant and the thickness of the asphalt and base of the pavement sample structure shown in Fig. 6.16 using the detected signals. Measurement results show accuracy of the measurement as well as good detection performance of the developed sensor system for the pavement structure.

Note that in table 6.2, the assumed loss tangent value of the asphalt is chosen from known typical values in the range of 0.004 to 0.01.

CHAPTER VII

CONCLUSIONS

A. Conclusions of Research

Through this research I have made a novel impulse radar system with tunable operating frequency band. The first objective of the research was the development of novel microwave components, such as transmitter, receiver, and antennas, all useful for a impulse radar system. The second objective was the integration of these newly developed microwave components into a single system along with the signal processing unit to develop the complete prototype of an advanced impulse radar system.

At first, through the system analysis of the impulse radar, especially for the application of the pavement assessment, we were able to estimate that the minimum required peak power of the transmitting pulse is 80 mW and the required pulse duration is 400 ps to obtain 1 in of range resolution. The receiver and antennas as well as the transmitter were designed to accommodate these requirements, in particular the upper limiting frequency of about 4 GHz.

To implement the impulse radar system with tunable frequency band, I developed a novel transmitter with frequency-band tuning capability, which is a tunable monocycle pulse generator. This transmitter can generate four different monocycle pulse durations, 450, 600, 880, and 1170 ps, which are UWB signals covering 0.15 to 3.7 GHz of ultra-wideband, and is tuned by switching of PIN diode pairs with a novel anti-parallel configuration. The output monocycle pulse durations can be reconfigurable by simple modification of the position of the PIN diode switches. The proposed transmitter circuit may generate a relatively high pulse peak power of 200 to 400 mW for 50 Ω load using a low DC bias voltage level of as much as maximum ±18 V. By using high-speed opamp and buffer ICs at the driving stage of the transmitter, the circuit structure is compact and the design and fabrication are possible at low cost.

For the receiver circuit, a novel CSH sampling mixer was developed, and all other components required for down-conversion such as local strobe pulse generator and the baseband video amplifier were integrated with the CSH sampling mixer into a single PCB, which is called the integrated sampling mixer. The proposed sampling mixer circuit has unprecedented low conversion loss of as little as 2.5 dB for a 450-ps monocycle pulse signal and 4.5 dB for a continuous wave signal. The 3-dB operating frequency band is 5.5 GHz, which is wide enough to cover most operating frequency range of the subsurface penetrating radar. A UWB LNA circuit was developed only for the application of low power pulse transmission and detection. This circuit might be also useful for many test and measurement applications required for the development of the subsurface penetrating radar system. Similarly to other impulse radar systems, the receiver system is a synchronous sampling receiver using two reference clock oscillators. The feature of the designed receiver system is that it uses low-cost VC-TCXO as the reference clock oscillator and the inherent frequency modulation effect of the VC-TCXO occurred by jittering of the clock is compensated at the signal processing stage by using a novel signal monitoring method.

The synchronous sampling receiver system was designed by derivation of simple but useful equations from which design parameters for the signal processing unit as well as the receiver were derived.

The designed microstrip quasi-horn antenna has acceptable performance for all of four transmitting pulse durations. The quasi-horn antenna was designed initially according to the optimized design method for TEM horn antenna and further optimized with respect to the open-end termination impedance of the antenna using the EM simulator, Microwave Studio.

All of the microwave circuit components were integrated into a microwave module with compact structure, taking advantage of the inherent structure of the quasi-horn antenna. The complete system was built by connecting the integrated microwave module to the signal processing unit implemented in Labview programming language.

The test and measurement results have shown the validity of the developed sensor system through detection of all layer interfaces embedded in the sample structure and measurement of the dielectric constant and the thickness of the layer with accuracy. The detection results displayed on the B-scan format for some sample structures have shown the validity of the developed system by detecting all the layer interfaces embedded in the sample structure. The test results also show that 450 and 600-ps pulses are the most useful ones among available pulse durations since these higher frequency band signals render low clutter signal levels and better range resolutions.

All of the developed components--transmitter, receiver, antenna, and UWB-LNA--can be utilized for the development of a low-cost short-range high-resolution SPR for applications such as pavement assessment, geophysical prospecting, UXO and landmine detection, as well as UWB communication systems. The developed tunable monocycle pulse generator with relative high pulse power can be used for many UWB applications. Its tuning capability for pulse duration may provide more flexibility in sensor operation such as using different pulse durations suitable for the investigated object, and makes achieving higher range resolution and deeper penetration depth at the same time by multi-band processing possible. This novel integrated CSH sampling mixer may provide superior performance in most high-resolution UWB applications because of its 5.5 GHz wide bandwidth characteristic and low conversion loss. The designed microstrip quasi-horn antenna and its design technique have shown the possibility of pulse transmission with low distortion and low side-lobe ringing for multiple pulse durations. The designed UWB-LNA may be a useful device for weak signal detection, especially in long range detection applications or test and measurement experiments of the UWB radar sensor. The developed prototype system may apply to many UWB applications and further modifications as described in the next section may improve the performance and complete the development of more realistic UWB radar sensor.

B. Recommendations for Future Work

There are some recommendations for improving system performance in terms of efficiency of system operation and for greater optimization in system level for a specific application.

The operating efficiency of the current system is not at a satisfactory level because of the manual control and compensation with respect to the frequency modulation effect on the down-converted signal. To improve this situation, we can first apply a PLL (Phase Locked Loop) circuit to both reference clock oscillator outputs; one output is used as a reference signal of the PLL and the other is used as an input of the PLL so that the input signal can always follow the frequency change of the reference signal; as a result, the output of the PLL and the reference signal can maintain the fixed frequency deviation required for the synchronous sampling even in a situation where both clock outputs are not stable. Therefore, using PLL circuit, we may convert manual compensation to automatic, which leads to improvements in the operating efficiency of the system.

If the frequency modulation effect is automatically compensated, then the signal processing could be also simplified. The development of real time processing, including

B-scan format display, may facilitate tests of the system and optimization of system configuration.

A greater optimization at system level is required for real system development through more experiments for real target structure. The height of the sensor from the surface of the object is the system configuration factor that needs to be optimized at system level. More experimental results on more sample structures close to real situations may provide helpful information in tuning the system configuration.

Using a single antenna as a monostatic configuration is a desirable approach in the design of the system since it can avoid direct cross-coupling problem and render a more compact system structure if the precedent design problem of wideband diplexer can be solved.

Finally, for easy testing and experiments on the real target, especially in outdoor environments or for real system development, the DC power supply module might be embedded into the microwave module.

REFERENCES

[1] M. I. Skolnik, “An introduction to impulse radar,” Naval Research Laboratory, Washington, DC, NRL Memorandum Report 6755, Nov. 1990.

[2] J. D. Taylor, *Introduction to Ultra-Wideband Radar Systems*, Boca Raton, FL: CRC Press, 1995.

[3] D. J. Daniels, *Surface Penetrating Radar*. London, U.K.: IEE Press, 1996.

[4] D. J. Daniels, D. J. Gunton, and H. F. Scott, “Introduction to subsurface radar,” *IEE Proc.*, vol. 135, no. 4, pp. 278-320, Aug. 1988.

[5] J. D. Taylor, *Ultra-Wideband Radar Technology*, Boca Raton, FL: CRC Press, 2001.

[6] J. Park, “Development of microwave and millimeter-wave integrated-circuit stepped-frequency radar sensors for surface and subsurface profiling,” Ph.D. Dissertation, Dept. of Electrical Engineering, Texas A&M Univ., College Station, TX, Dec. 2003.

[7] R. J. Fontana. (2000, May). “Recent applications of ultra wideband radar and communications systems,” in *Ultra-Wideband, Short-Pulse Electromagnetics 5*, P. D. Smith and S. R. Cloude, Ed. New York: Kluwer Academic/Plenum Publishers, 2002, pp. 225-234.

[8] J. P. Warhus (1994, Sep.). Advanced ground-penetrating, imaging radar for bridge inspection. Lawrence Livermore National Laboratory, CA. [Online]. Available: http://www-eng.llnl.gov/dsed/documents/em/jwpctta93.html

[9] Time Domain Corp., AL. PulsON Technology: Time modulated ultra-wideband for wireless applications. [Online]. Available: http://www.time-domain.com/Files/downloads/techpapers/PulsONoverview.pdf

[10] S. Azevedo and T. E. McEwan, "Micropower impulse radar," *Science & Tech. Review*, pp. 17-29, Jan./Feb. 1996.

[11] A. Duzdar and G. Kompa, "Applications using a low-cost baseband pulsed microwave radar sensor," in *Proc. 18th IEEE Instrumentation and Measurement Technology Conf.*, 2001, pp. 239-243.

[12] A. Yarovoy and L. Ligthart, "Full-polarimetric video impulse radar for landmine detection: Experimental verification of main design ideas," in *Proc. 2nd Int. Workshop on Advanced Ground Penetrating Radar*, 2003, pp. 148-155.

[13] L. Ligthart and A. Yarovoy, "STW Project: Advanced relocatable multi-sensor system for buried landmine detection," in *Proc. 2nd Int. Workshop on Advanced Ground Penetrating Radar*, 2003, pp. 5-8.

[14] J. S. Lee, "Design of high-frequency pulse subsurface penetrating radar for pavement assessment," Ph.D. Dissertation, Dept. of Electrical Engineering, Texas A&M Univ., College Station, TX, Dec. 2000.

[15] J. S. Lee, C. Nguyen, and T. Scullion, "Impulse ground penetrating radar for nondestructive evaluation of pavements," in *2002 IEEE MTT-S International Microwave Symposium Digest*, 2002, pp. 1361-1363.

[16] A. P. Annan and J. L. Davis, "Radar range analysis for geological materials," *Geological Survey of Canada*, vol. 77-1B, pp. 117-124, 1977.

[17] J. L. Davis and A. P. Annan, “Ground-penetrating radar for high-resolution mapping of soil and rock stratigraphy,” *Geophysical Prospecting*, vol. 37, pp. 531-551, 1989.

[18] W. L. Stutzman and G. A. Thiele, *Antenna Theory and Design*. New York, NY: John Wiley & Sons, 1998.

[19] D. K. Cheng, *Fundamentals of Engineering Electromagnetics*. Reading, MA: Addison-Wesley, 1993.

[20] *The Criterion for the Tangential Sensitivity Measurement*, Agilent Technologies Inc., Palo Alto, CA, Application Note 956-1.

[21] K. Chang, *Microwave Solid-State Circuits and Applications*. New York, NY: John Wiley & Sons, 1994.

[22] E. A. Theodorou, M. R. Gorman, P. R. Rigg, and F. N. Kong, “Broadband pulse-optimised antenna,” *IEE Proc.*, vol. 128, pt. H, no. 3, pp. 124-130, Jun. 1981.

[23] E. K. Miller, *Time-Domain Measurements in Electromagnetics*, New-York, NY: Van Nostrand Reinhold, 1986.

[24] J. Millman and H. Taub, *Pulse, Digital, and Switching Waveforms*, New-York, NY: McGraw-Hill, 1965.

[25] A. M. Nicolson, “Subnanosecond risetime pulse generators,” *IEEE Trans. Instrum. Meas.*, vol. 25, no. 2, pp. 104-107, Jun. 1976.

[26] R. Tielert, “Subnanosecond-pulse generator employing 2-stage pulse step sharpener,” *Electron. Lett.*, pp. 84-85, Dec. 1976.

[27] W. B. Herden, “Application of avalanche transistors to circuits with a long mean time to failure,” *IEEE Trans. Instrum. Meas.*, vol. 25, no. 2, pp. 152-160, Jun. 1976.

[28] H. A. Sayadian, M. G. Li, and C. H. Lee, “Generation of high-power broad-band microwave pulses by picosecond optoelectronic technique,” *IEEE Trans. Microwave Theory and Techn.*, vol. 37, no. 1, pp. 43-50, Jan. 1989.

[29] R. J. Forcia, E. Schamiloglu, and C. B. Fleddermann, “Simple techniques for the generation of high peak power pulses with nanosecond and subnanosecond rise times,” *Rev. Sci. Instrum.*, vol. 67, no. 7, pp. 2626-2629, Jul. 1996.

[30] R. J. Fontana, E. A. Richley, L. C. Beard, and J. Barney, “A programmable ultra wideband signal generator for electromagnetic susceptibility testing,” in *2003 IEEE Conf. on Ultra Wideband Systems and Technologies*, 2003, pp. 21-25.

[31] J. R. Andrews, “Picosecond pulse generators for UWB radars,” Picosecond Pulse Labs, Boulder, CO, Application Note AN-9, May 2000.

[32] J. R. Andrews, “UWB signal sources & antennas,” Picosecond Pulse Labs, Boulder, CO, Application Note AN-14, Feb. 2003.

[33] K. Daneshvar and L. Howard, “High current nanosecond pulse generator,” in *Proc. IEEE Southeastcon ’89*, 1989, pp. 572-576.

[34] U. A. Uhmeyer and J. C. Libby, “A fast variable transition time pulse generating circuit,” in *Proc. 9th IEEE Instrumentation and Measurement Technology Conf.*, 1992, pp. 152-157.

[35] J. Han and C. Nguyen, “Ultra-wideband electronically tunable pulse generators,” *IEEE Microwave Wireless Compon. Lett.*, vol. 14, no. 3, pp. 112-114, Mar. 2004.

[36] J. S. Lee and Cam Nguyen, “A uniplanar picosecond pulse generator using step-recovery diode,” *Electron. Lett.*, vol. 37, no. 8, pp. 504-506, Apr. 2001.

[37] J. S. Lee and Cam Nguyen, “New uniplanar subnanosecond monocycle pulse generator and transformer for time-domain microwave applications,” *IEEE Trans. Microwave Theory and Tech.*, vol. 49, no. 6, pp. 1126-1129, Jun. 2001.

[38] J. S. Lee and Cam Nguyen, “Novel low-cost ultra-wideband, ultra-short-pulse transmitter with MESFET impulse-shaping circuitry for reduced distortion and improved pulse repetition rate,” *IEEE Microwave and Wireless Compon. Lett.*, vol. 11, no. 5, pp. 208-210, May 2001.

[39] J. Han and Cam Nguyen, “A new ultra-wideband, ultra-short monocycle pulse generator with reduced ringing,” *IEEE Microwave and Wireless Compon. Lett.*, vol. 12, no. 6, pp. 206-208, Jun. 2002.

[40] M. J. Lesha and F. J. Paoloni, “Generation of balanced subnanosecond pulses using step-recovery diodes,” *Electron. Lett.*, vol. 31, no. 7, pp. 510-511, Mar. 1995.

[41] *Pulse and Waveform Generation with Step Recovery Diodes*, Agilent Technologies Inc., Palo Alto, CA, Application Note 918.

[42] G. D. Cormack and A. P. Sabharwal, “Picosecond pulse generator using delay lines,” *IEEE Trans. Instrum. Meas.*, vol. 42, no. 5, pp. 947-948, Oct. 1993.

[43] S. Hamilton and R. Hall, "Shunt-mode harmonic generation using step recovery diodes," *Microwave Journal*, pp. 69-78, Apr. 1967.

[44] J. L. Moll and S. Hamilton, "Physical modeling of the step recovery diode for pulse and harmonic generation circuits," *Proc. of IEEE*, vol. 57, no. 7, pp. 1250-1259, Jul. 1969.

[45] S. Goldman, "Computer aids design of impulse multipliers," *Microwaves & RF*, pp. 101-128, Oct. 1983.

[46] J. Zhang and V. Räisänen, "Computer-aided design of step recovery diode frequency multipliers," *IEEE Trans. Microwave Theory and Tech.*, vol. 44, no. 12, pp. 2612-2616, Dec. 1996.

[47] S. A. Maas, Nonlinear Microwave Circuits, New York, NY: IEEE Press, 1997.

[48] S. Abuasaker and G. Kompa, "A high sensitive receiver for baseband pulse microwave radar sensor using hybrid technology," in *Proc. IEEE Radar Conference*, 2002, pp. 121-124.

[49] K. J. Weingarten, M. J. W. Rodwell, and D. M. Bloom, "Picosecond optical sampling of GaAs integrated circuits," *IEEE J. Quantum Electron.*, vol. 24, no. 2, pp. 198-220, Feb. 1988.

[50] M. Kamegawa, K. Giboney, J. Karin, S. Allen, M. Case, R. Yu, M. J. W. Rodwell, and J. E. Bowers, "Picosecond GaAs monolithic optoelectronic sampling circuit," *IEEE Photonics Tech. Lett.*, vol. 3, no. 6, pp. 567-569, Jun. 1991.

[51] D. M. Akos and J. B. Y. Tsui, "Design and implementation of a direct digitization GPS receiver front end," *IEEE Trans. Microwave Theory Tech.*, vol. 44, no. 12, pp. 2334-2339, Dec. 1996.

[52] W. M. Grove, "Sampling for oscilloscopes and other RF systems: DC through X-band," *IEEE Trans. Microwave Theory and Tech.*, vol. MTT-14, no. 12, pp. 629-635, Dec. 1966.

[53] J. Merkelo and R. D. Hall, "Broad-band thin-film signal sampler," *IEEE J. of Solid-State Circuits*, vol. SC-7, no. 1, pp. 50-54, Feb. 1972.

[54] N. P. Akers, "RF sampling gates: A brief reviw," *IEE Proc.*, vol. 133, no. 1, pp. 45-49, Jan. 1986.

[55] A. Bologlu, "A 26.5-GHz automatic frequency counter with enhanced dynamic range," *Hewlett-Packard J.*, pp. 20-22, Apr. 1980.

[56] B. E. Gilchrist, R. D. Fildes, and J. G. Galli, "The use of sampling techniques for miniaturized microwave synthesis applications," in *1982 IEEE MTT-S International Microwave Symposium Digest*, 1982, pp. 431-433.

[57] K. Madani and C.S. Aichison, "A 20GHz Microwave Sampler," *IEEE Trans. Microwave Theory and Tech.*, vol. 40, no. 10, pp. 1960-1963, Oct. 1992.

[58] S. E. Moore, B. E. Gilchrist, and J. G. Galli, "Microwave sampling effective for ultrabroadband frequency conversion," *MSN & CT*, pp. 113-126, Feb. 1986.

[59] S. R. Gibson, "Gallium arsenide lowers cost and improves performance of microwave counters," *Hewlett-Packard J.*, pp. 4-10, Feb. 1986.

[60] M. S. Shakouri, A. Black, B. A. Auld, and D. M. Bloom, “500 GHz GaAs MMIC sampling wafer probe,” *Electron. Lett.*, vol. 29, no. 6, pp. 557-558, Mar. 1993.

[61] M. J. W. Rodwell, M. kamegawa, R. Yu, M. Case, E. Carman, and K. S. Giboney, “GaAs nonlinear transmission lines for picosecond pulse generation and millimeter-wave sampling,” *IEEE Trans. Microwave Theory Tech.*, vol. 39, no. 7, pp. 1194-1204, Jul. 1991.

[62] Y. Konishi, M. Kamegawa, M. Case, R. Yu, S. T. Allen, and M. J. W. Rodwell, “A broadband free-space millimeter-wave vector transmission measurement system,” *IEEE Trans. Microwave Theory Tech.*, vol. 42, no. 7, pp. 1131-1139, Jul. 1994.

[63] A. Miura, “Monolithic sampling head IC,” *IEEE Trans. Microwave Theory and Tech.*, vol. 38, no. 12, pp. 1980-1985, Dec. 1990.

[64] R. A. Marsland, V. Valdivia, C. J. Madden, M. J. W. Rodwell, and D. M. Bloom, “130 GHz GaAs monolithic integrated circuit sampling head,” *Appl. Phys. Lett.*, vol. 55, no. 6, pp. 592-594, Aug. 1989.

[65] P. Abele, M. Birk, D. Behammer, H. Kibbel, A. Trasser, P. Maier, K.-B. Schad, E. Sönmez, and H. Schumacher, “Sampling Circuit on Silicon Substrate for Frequencies beyond 50 GHz,” in *2002 IEEE MTT-S International Microwave Symposium Digest*, 2002, pp. 1681-1684.

[66] A. Pärssinen, R. Magoon, S. I. Long, and V. Porra, “A 2-GHz subharmonic sampler for signal downconversion,” *IEEE Trans. Microwave Theory Tech.*, vol. 45, no. 12, pp. 2344-2351, Dec. 1997.

[67] J. S. Lee and Cam Nguyen, "A low-cost uniplanar sampling down-converter with internal local oscillator, pulse generator, and IF amplifier," *IEEE Trans. Microwave Theory and Tech.*, vol. 49, no. 2, pp. 390-392, Feb. 2001.

[68] J. Han and C. Nguyen, "Integrated balanced sampling circuit for ultra-wideband communications and radar systems," *IEEE Microwave Wireless Compon. Lett.*, to be published.

[69] D. F. Williams and K. A. Remley, "Analytic sampling-circuit model," *IEEE Trans. Microwave Theory Tech.*, vol. 49, Jun. 2001, pp. 1013-1019.

[70] K. A. Remley, "Realistic sampling-circuit model for a nose-to-nose simulation," in *2000 IEEE MTT-S International Microwave Symposium Digest*, 2000, pp. 1473-1476,

[71] M. Aikawa and H. Ogawa, "A new MIC magic-T using coupled slot lines," *IEEE Trans. Microwave Theory and Tech.*, vol. MTT-28, no. 6, pp. 523-528, Jun. 1980.

[72] S. A. Maas, *Microwave Mixers*, Norwood, MA: Artech House, 1993.

[73] *Advanced Design System 2003A Release Notes*, Agilent EEsof EDA, Westlake Village, CA, 2003.

[74] G. Gonzalez, *Microwave Transistor Amplifiers: Analysis and Design*. Upper Saddle River, NJ: Prentice-Hall, 1996.

[75] H. G. Schantz, "Introduction to ultra-wideband antennas," in *2003 IEEE Conference on Ultra Wideband Systems and Technologies*, 16-19 Nov., 2003, pp. 1-9.

[76] A. G. Yarovoy, B. Sai, G. Hermans, P. V. Genderen, L. P. Ligthart, A. D. Schukin, and I. V. Kaploun, “Ground penetrating impulse radar for detection of small and shallow-buried objects,” in *IGARSS ’99 Proceedings of IEEE 1999 International Geoscience and Remote Sensing Symposium*, 1999, pp. 2468-2470.

[77] D. J. Daniels, “Short pulse radar for stratified lossy dielectric layer measurement,” IEE Proc., vol. 127, pt. F, no. 5, pp. 384-388, Oct. 1986.

[78] J. A. N. Noronha, T. Bielawa, C. R. Anderson, D. G. Sweeney, S. Licul, and W. A. Davis, “Designing antennas for UWB systems,” *Microwaves & RF*, Jun. 2003.

[79] J. D. Cermignani, R. G. Madonna, P. J. Scheno, and J. Anderson, “Measurement of the performance of a cavity backed exponentially flared TEM horn,” *Proc. of SPIE: Ultrawideband Radar*, vol. 1631, pp. 146-154, May 1992.

[80] J. Park and C. Nguyen, “An ultra-wideband microwave radar sensor for characterizing pavement subsurface,” in *2003 IEEE MTT-S International Microwave Symposium Digest*, 8-13 Jun. 2003, pp. 1143-1146.

[81] C. Nguyen, J. Lee, and J. Park, “Ultra-wideband microstrip quasi-horn antenna,” *Electron. Lett.*, vol. 37, no. 12, pp. 731-732, Jun. 2001.

[82] S. Evans and F. N. Kong, “TEM horn antenna: input reflection characteristics in transmission,” *IEE Proc.*, vol. 130, pt. H, no. 6, pp. 403-409, Oct. 1983.

[83] *CST Micorwave Studio User Manual*, CST-Computer Simulation Technology, Darmstadt, Germany, 2003.

[84] L. P. Ligthart, A. G. Yarovoy and A. Y. Kirana, “GPR antenna simulations and optimizations in time domain,” in *International Conference on Antenna Theory and Techniques*, 9-12 Sep., 2003, pp. 21-24.

[85] R. P. Hecken, “A near-optimum matching section without discontinuities,” *IEEE Trans. Microwave Theory and Tech.*, vol. MTT-20, no. 11, pp. 734-739, Nov. 1972.

[86] *MATLAB User Manual*, The MathWorks Inc., Natick, MA, 2002.

[87] *LabVIEW User Manual*, National Instruments, Austin, TX, 1998.

VITA

Jeongwoo Han was born in Pohang, Republic of Korea in May 1966. He received the B.S. degree in electronic engineering from Kyungpook National University in 1988 and the M.S. degree in electronic engineering from the same university in 1990. Upon graduating with a M.S. degree, he worked as a research engineer at the Agency for Defense Development in Republic of Korea, for 8 years. During that time, he developed the signal processing algorithms for underwater surveillance system and Towed Array Sonar System. He worked as a research assistant under Dr. Cam Nguyen in the sensing, imaging, and communication systems laboratory. His graduate research projects have been supported by grants from the National Science Foundation, the Texas Transportation Institute, the Southwest Region University Transportation Center, the Texas Advanced Research Program and Dell Computer Corporation. His current research interests are in microwave and millimeter-wave integrated circuits, antennas, subsurface radar sensors, and CMOS RF circuits.

Dr. Han can be contacted via Professor Cam Nguyen, Texas A&M University, Department of Electrical Engineering, College Station, TX 77843-3128.